Design, fabrication and characterisation of interdigitated back-contacted c-Si solar cells based on transition metal oxides

Gerard Masmitja Rusiñol

UNIVERSITAT POLITÈCNICA DE CATALUNYA
BARCELONATECH
Departament d'Enginyeria Electrònica

Design, fabrication and characterisation of interdigitated back-contacted c-Si solar cells based on transition metal oxides

Thesis submitted in partial fulfilment of the requirement for the PhD Degree issued by the Universitat Politècnica de Catalunya, in its Electronic Engineering Program.

Gerard Masmitjà Rusiñol

Director: Pablo Ortega Villasclaras

Barcelona, July 2019

To Blanca

Agraïments

Vull agrair a tots els que heu format part d'aquest camí, apassionant, d'iniciació a la recerca i la investigació. Converses i debats, que no oblidaré, sobre el funcionament, la fabricació i la caracterització de les cèl·lules solars. Ha sigut increïble compartir aquests anys al vostre costat: Pablo Ortega, Joaquim Puigdollers, Cristoval Voz, Isidro Martín i Ramón Alcubilla. En especial, un agraïment infinit al director d'aquesta tesi, en Pablo, sense tu, aquesta tesis no hagués estat possible. Encara recordo, la passió pels semiconductors que transmeties/transmets els teus alumnes, a l'assignatura de dispositius i tecnologies. Agrair també, en Joaquim, per enfocar la tesi en els contactes selectius mitjançant òxids metàl·lics de transició.

A la Gema Lopez, gràcies per ensenyar-me els processos de fabricació i a utilitzar els equips de la sala blanca, un agraïment sincer, també, a en Guillermo Gerling, a sigut un plaer investigar al vostre costat. A la resta de companys que he tingut el gust de conèixer, gràcies: Eric Calle, Jin Chen, Sergi Gorreta, Arnau Coll, Lukasz Kowalski, Didac Vega, Eloi Ros, Benjamin Pusay, Estefania Almache, i resta de col·legues del D213.

Als tècnics del laboratori, Miguel i Xavi, menció especial, per mantenir-lo en funcionament.

Gràcies a la Roser per la revisió/correcció ortogràfica de part d'aquesta tesi.

Per acabar, i no menys important, donar les gràcies a la família, en especial al meu germà Ivan i als meus pares, la Fina i en Medir per ajudar-me i ser-hi sempre. Sense vosaltres no hauria arribat fins aquí.

Agrair-te mil vegades a tu Elisabet per la paciència que has fet gala envers meu durant aquests anys de doctorat. Finalment a la petita Blanca, tu que vas néixer el 4 d'octubre del 2017, t'has convertit en motor de tot, gràcies.

Abstract

The photovoltaic industry is mainly dominated by crystalline silicon (c-Si) solar cells, in which contact selectivity is usually achieved by doping the wafer surfaces with phosphorous (n^+) and boron (p^+) by means of high temperature oven-based diffusions, called pn-Junction (pnJ). This requires complex and energy consuming processes and lengthy cleaning protocols to avoid possible degradation of bulk lifetime, increasing the number of steps involved in the manufacturing and consequently the production cost.

In order to replace those high temperature diffusions, several approaches have been studied. The well-known silicon heterojunction (SHJ) structure using doped and intrinsic hydrogenated amorphous silicon (a-Si:H) films is probably the best known. Nevertheless, this option uses toxic and flammable gases as dopant precursors, which is not desirable from the point of view of process simplicity.

In parallel, several contact structures have been developed from the past to now. Among them, two cell architectures have pushed forward the efficiency of c-Si solar cells. On the one hand, the passivated emitter and rear locally-diffused (PERL) cell structure, which was designed by the group leader by Prof. Martin A. Green at the University of New South Wales, Sydney, achieving power conversion efficiencies of up to 25%. On the other hand, the interdigitated back-contacted (IBC) cell structure, which was firstly designed for photovoltaic concentration applications, but in recent years have been applied on non-concentration purposes. In fact, the world solar cell efficiency record on c-Si substrates (26.6%) is achieved with an IBC cell structure.

This thesis deals with the research on c-Si solar cells using both an IBC structure and an alternative approach to the conventional pnJ and SHJ concepts by implementing *novel* selective contacts, which are those based on transition metal oxides (TMOs).

The first part of the Thesis is focused on the use of vanadium oxide (V_2O_x) as hole-selective contact. It is demonstrated that the V_2O_x has better selectivity behaviour when a nickel metal, which has a high work-function, is used as a capping layer. Finally, the selective contact based on Ni-capped V_2O_x film is applied to an IBC c-Si solar cell yielding an efficiency of 19.7%. In this device the electron-selective contact is performed with the laser-doped technique, where the n^+ region is formed by the laser-processing of a dielectric film, consisting of a phosphorous-doped amorphous silicon carbide layer.

The last part of the Thesis is related to the development of an electron-selective contact based on TMOs, replacing the laser-doped contacts. In this way, a titanium oxide (TiO_x) film is used in combination with a thin aluminium oxide (Al_2O_x) passivating interlayer. Once again, the metal capping has an influence to the selectivity of the final contact, being the best option the use of a magnesium film, which has a low work-function. Finally, a novel IBC c-Si solar cell is developed, which combines the previously mentioned Ni-capped V_2O_x as hole-selective contact and Mg-capped Al_2O_x/TiO_x as electron-selective contact, yielding a proof-of-concept device with a conversion efficiency of up to 19.1%. It is important to stress that both selective contacts are fabricated at temperatures lower than 100 ^oC reducing the overall thermal budget of the fabrication process, as well as circumventing the use of toxic and flammable gasses as dopant precursors.

"It is not the mountain we conquer but ourselves"

Sir Edmund Hillary

Contents

List of symbols

$\hbar$	Planck's constant	eVs
φ	Electrical potential	V
λ	Wavelength	m
hf	Photon energy	eV
E_p	Phonon energy	eV
E_G	Bandgap energy	eV
E_V	Valence band energy edge	eV
E_C	Conduction band energy edge	eV
E_F	Fermi energy	eV
E_{Fn}	Fermi energy for electrons in conduction band	eV
E_{Fp}	Fermi energy for holes in valence band	eV
χ_e	Electron affinity	eV
Φ	work-function	eV
p^+	Doped region with acceptor impurities	
n^+	Doped region with donor impurities	
$\alpha(\lambda)$	Absorption coefficient	cm^{-1}
τ_{eff}	Effective recombination lifetime	s
τ_b, τ_s	Bulk and surface recombination lifetime	s
τ_{SRH}	Shockley-Read-Hall recombination lifetime	s
τ_{in}	Intrinsic recombination lifetime	s
S	Surface recombination velocity	cm/s
I	Current; Intensity	A
J	Current density	A/cm^2
σ_n, σ_p	Electron and hole conductivity	S/cm
q	Elementary charge	C
J_0	Recombination current density	fA/cm^2
J_L	Photocurrent density	A/cm^2
V_{th}	Thermal voltage	V
AM1.5G	Solar spectrum	kW/m^2

S_{10}	Contact selectivity	
n	Diode ideality factor	
I_0	Diode saturation current	A
R_{sh}	Shunt resistance	Ω
R_s	Series resistance	Ω
r_s	Specific series resistance	Ωcm^2
V_{oc}	Open-circuit voltage	V
V_{mp}	Voltage at maximum power point	V
I_{sc}	Short-circuit current	A
I_{mp}	Current at maximum power point	A
FF	Solar cell fill factor	
η	Solar cell energy-conversion efficiency	%
T	Temperature	ºC
iV_{oc}	Implied open circuit voltage	V
N_{Bulk}	Bulk doping concentration	cm^{-3}
g_{eeh}	Richter enhanced factor	
B_{rel}	Altermatt recombination coefficient	
Δn, Δp	Excess concentration of minority-carrier electrons and holes	cm^{-3}
n_i	Intrinsic concentration	cm^{-3}
n, p	Electron and hole concentration	cm^{-3}
W	Thickness of the wafer	cm
r_c	Specific contact resistance	Ωcm^2
R_T	Total resistance	Ω
d	Dot-contact diameter	cm
d_b	Estimated back-contact dot diameter	cm
ρ	Resistivity	Ωcm
R_0	Set-up resistance	Ω
R_b	Back-contact resistance	Ω

1 Introduction

This Chapter explains the motivation and objectives of the Thesis in order to obtain a step forward in high efficiency solar cells using transition metal oxide as selective contacts in combination with an interdigitated back-contacted cell architecture. At the end of this Chapter, the structure of the Thesis is described.

1.1 Context

In the late 1940s, the invention of the transistor at Bell Telephone Laboratories, USA, by J. Bardeen, W.-H. Brattain and W.-B. Shockley, began a revolution in the world of electronics by replacing thermionic valves for low-cost semiconductor-based devices. From that crucial moment, many researchers started to study the properties of semiconductors and their applications, establishing the technology and the knowledge of silicon processing.

That new technology was the basis for developing new semiconductor devices, including those based on the photovoltaic phenomenon such as solar cells. A solar cell is a device that absorbs photons of light and generates electron-hole pairs, which can be extracted to an external circuit, generating electrical energy, i.e. electric potential and current. Although, the photovoltaic effect was observed for the first time by a French physicist Alexandre-Edmond Becquerel, in 1839, it was not until 1953 when a solar cell with a reasonable power conversion efficiency, 6%, was made as a proof-of-concept. This new paradigm was achieved by D. Chapin, C. Fuller and G. Pearson at Bell Telephone Labs, using silicon substrates, allowing the beginning of the photovoltaic age.

However, first efficiency values were very far from the theoretical thermodynamic limit, which is beyond 30% [1], indicating that there was room for improvement. As expected, the efficiency has progressively increased in recent decades, as a result of a better understanding of the properties of crystalline silicon (c-Si), as well as a great optimisation of the manufacturing technological processes. These improvements come basically from the reduction of the main loss mechanisms involved in the performance of solar cells, especially those related to the recombination of the photogenerated electrons and holes in the bulk and device surfaces. This has been achieved to a large extent by improving both the quality of the silicon raw material, i.e. low bulk recombination substrates, and surface passivation, i.e. low surface recombination velocities.

In addition, the structure of solar cells, which consists basically of an absorber and two electrodes, has also been investigated, applying different strategies to maximise energy conversion efficiency. Among them, two structures have achieved the most promising results in c-Si substrates (see Figure 1.1). On the one hand, the passivated emitter and rear locally-diffused (PERL) cell structure [2], which is used to reduce the optical losses on the rear surface by using a dielectric passivation layer covered by aluminium reflective metal, as well as minimising the recombination in the back contact by reducing the contacted area, i.e. the aluminium electrode contacts the silicon through the dielectric using an array of small holes (covering about 1% of the rear surface). Moreover, the use of diffused regions (p^+) decreases both surface recombination and contact resistance, improving the overall solar cell electrical performance.

On the other hand, the interdigitated back-contacted (IBC) structure [4] was developed to eliminate the optical losses on the front surface. There are no shadow areas, i.e. the photogenerated current can be maximised, since both contacts are placed on the rear side.

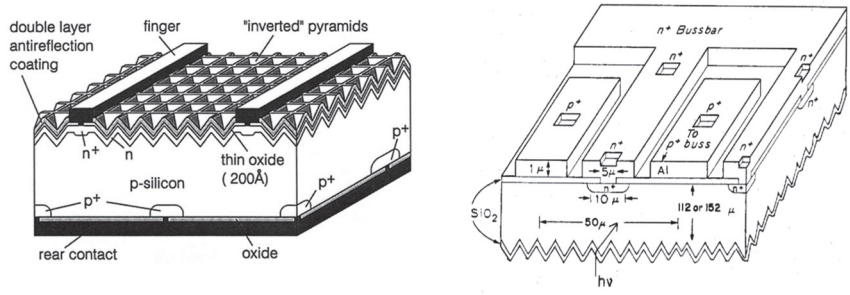

Figure 1.1 Sketch of the PERL cell structure (left) and IBC structure (right), which were published by [2] *© 1996 Elsevier Science and* [4] *© 1986 IEEE, respectively.*

Figure 1.2 shows the highest confirmed conversion efficiencies for different solar cell technologies published periodically by the National Renewable Energy Laboratory (NREL) [7]. Firstly, the silicon solar cells were fabricated from donor and acceptor impurities diffused on p-type c-Si wafers to perform, respectively, n^+ and p^+ regions acting as *basic* selective contacts. This technology has been dominant for many years in research laboratories and industries, achieving efficiencies of over 25% [5].

In the 2001 doped hydrogenated amorphous silicon (a-Si:H) films began to be used as selective contacts, named silicon heterojunction (SHJ), in solar cells. This concept was successfully applied not only in the laboratory, but also in industrial cells, in fact, the actual world record efficiency combines an IBC structure with SHJ contacts achieving a cell efficiency of 26.6% obtained by Kaneka Corporation, Japan [6]. Finally, other silicon-based absorbers are reported such as multicrystalline and thin-film crystal with cell efficiencies of 22% and 21%, respectively. These high efficiencies together with the maturity of the silicon technology industry, i.e. reasonable manufacturing cost, have allowed the dissemination of the photovoltaic devices across the globe as an alternative power source.

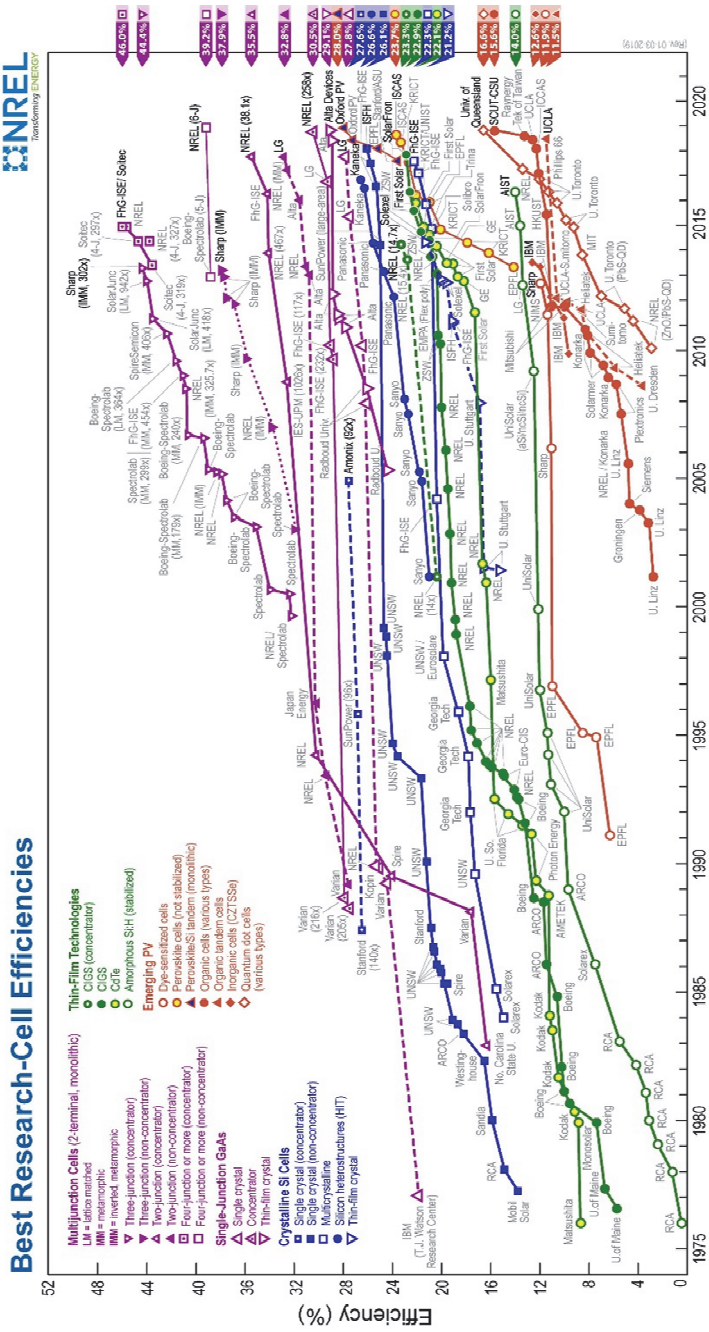

Figure 1.2 Highest confirmed conversion efficiencies for different solar cell technologies from 1976 to the present. Published by [7] *© 2019 NREL.*

1.2 Motivation

The efficiency of c-Si solar cells has improved to such an extent that further device advances are now based on innovative passivation/anti-reflection surface schemes, e.g. black silicon [8], and novel selective contact structures [9]. These new concepts are not only interesting to reduce the cost of manufacturing by simplifying the steps involved, but also from a scientific point of view, which increases the understanding of photovoltaic devices. This new paradigm broadens the technological possibilities and multiple options are actively being explored to achieve the best balance between efficiency and simplicity.

Regarding the use of selective contacts, the concept of which arises from the heritage of thin film and organic photovoltaics [10], in recent years several non-doping approaches have emerged in silicon photovoltaics. Among them, selective contacts based on transition metal oxides (TMOs) are the most promising candidates [11].

The TMOs are becoming very attractive as selective contacts applied to c-Si substrates due to their high bandgap (>3 eV), this fact allows a high optical transparency, together with the possibility of being deposited at low temperatures, for example thermal evaporation, spin or spray coating, or sputtering. TMOs with a high work-function (~7 eV) such as molybdenum oxide (MoO_x), tungsten oxide (WO_x) and vanadium oxide (V_2O_x) are preferred as substitutes for p^+ contacts, while low work-function compounds (~4 eV) such as magnesium oxide (MgO_x) and titanium oxide (TiO_x) are being investigated as candidates for n^+ contacts.

Figure 1.3 shows a review of c-Si solar cell efficiencies based on different selective contact approaches. This study has been published by the group led by Prof. Bram Hoex at the University of New South Wales (UNSW), Australia [12].

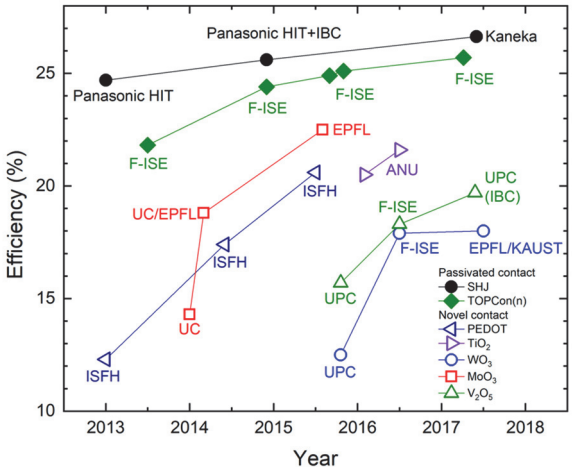

Figure 1.3 Champion efficiencies of various selective solar cell concepts. Extracted from [12] © *2019 UNSW Hoex Group.*

Notice that the use of TMOs as selective contact in c-Si solar cells started around the 2014 whit the study of the MoO_x films by the University of California, Berkeley. At the end of 2015 other TMOs were investigated by the group of Micro and NanoTechnologies (MNT) at the Universitat Politècnica de Catalunya (UPC) achieving solar cell efficiencies of up to 16% using V_2O_x and WO_x films as selective contacts. Moreover, it is important to remark that in 2017 a V_2O_x-based solar cell appears in combination with an IBC cell structure reaching a noticeable efficiency of 19.7%. This solar cell result is in fact a significant part of this Thesis.

In the past years, the MNT group has developed and optimized several c-Si solar cells using different approaches. Figure 1.4 and 1.5 summarise the evolution of MNT solar cells from the beginning of 2010 to the present, with their corresponding photovoltaic efficiency, using an IBC structure or a both sides-contacted architecture, respectively.

The MNT group has an extensive experience in the use of *conventional* pn-Junction which uses the well-known phosphorus and boron diffusion process to create the n^+ and p^+ regions, respectively, with efficiencies greater than 20% [13], [14]. Furthermore, the use of advanced surface texturizing, which is black silicon, has enabled to boost a solar cell efficiency of up to 22.1% [8].

The group has also explored the use of laser-doping approaches. On the one hand, the so-called laser fired contact (LFC), where a laser beam fires the aluminium putting it, through a dielectric passivation layer, into the c-Si substrate to form the p^+ contact. This technology allows efficiencies higher than 20% using a passivated emitter rear cell (PERC) structure [15] and efficiencies of 16% using a heterojunction structure [16].

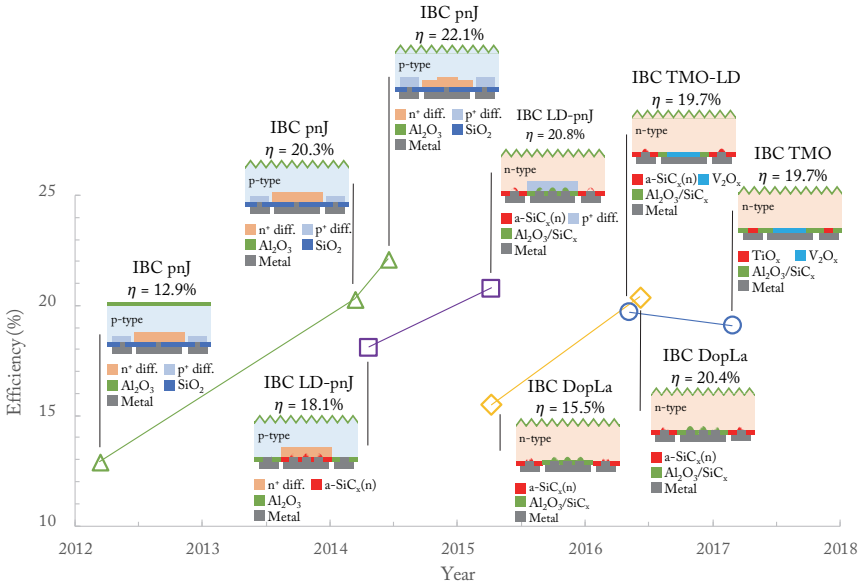

Figure 1.4 Main c-Si solar cell structures and their efficiencies reported by the MNT group of UPC, using interdigitated back-contacted devices (IBC).

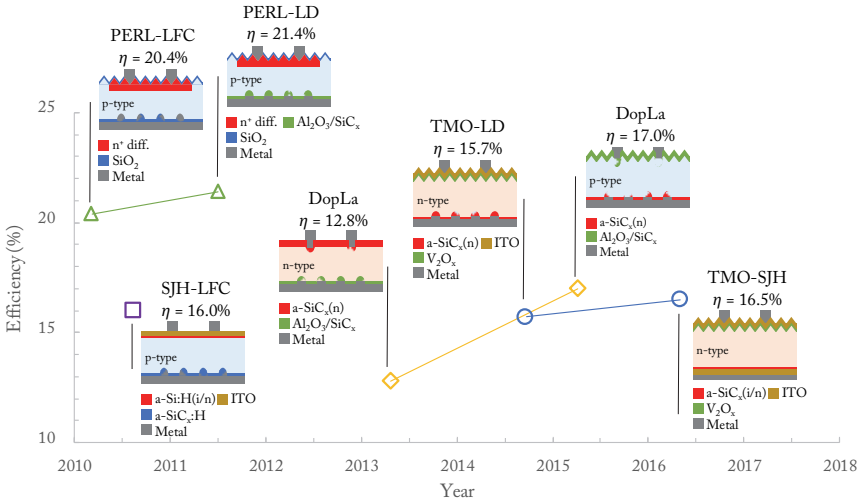

Figure 1.5 Main c-Si solar cell structures and their efficiencies reported by the MNT group of UPC, using both sides-contacted devices.

On the other hand, the laser-doped (LD) approach, where the n^+ or p^+ regions are formed by the laser-processing of dielectric films, which acts as dopant sources, as well as passivation layers and anti-reflection coating (ARC). The PERL-LD cell structure has allowed to obtain efficiencies of 21.4% [17] and the IBC LD-pnJ approach efficiencies of 18.1% [18] and 20.8% [19] using phosphorous and boron diffused *emitters*, respectively. Finally, the LD technique was used for both contacts with the so called DopLa (Doped by Lacer) cells [20]–[22], being a *cold* fabrication process, which is the use of temperatures below 400 ºC. In this way, a remarkable efficiency of 20.4% was obtained using an IBC structure [23].

Focusing on novel selective contacts, the MNT group has explored the application of TMOs as selective contacts on c-Si based solar cells, obtaining cell efficiencies of around 16% [24], [25], using a both sides-contacted solar cell structure. A further step has been explored, being the main part of this Thesis, through the use

of selective contacts based on TMOs in combination with an IBC cell structure. In this way, an IBC solar cell with an efficiency of 19.7% [26] has been fabricated using an *hybrid* structure, i.e. Ni-capped V_2O_x film and LD selective contact approaches as an alternative to the p^+ and n^+ regions, respectively. Furthermore, a remarkable IBC solar cell with an efficiency of 19.1% [27] with a fully-TMO based structure, which is using Ni-capped V_2O_x and Mg-capped Al_2O_x/TiO_x selective contacts, has been achieved in this work.

1.3 Objectives of the Thesis

The main objective of this Thesis has been the fabrication of high efficiency IBC c-Si solar cells using TMOs as dopant-free carrier-selective contacts. To achieve this, it has been necessary to develop an adequate baseline fabrication process, compatible with the low temperature TMOs deposition stages, as well as the study and optimisation of the TMO/metal and c-Si/TMO contact interfaces.

The first part of the research was dedicated to acquire the knowledge about the technological processes involved in the fabrication of the IBC solar cell developed by the MNT group. Thus, the work previously developed in the master's Thesis related to the passivation of boron diffused regions [28] was used to develop an IBC c-Si solar cell. In this initial solar cell, the hole-selective contact was formed on a boron-doped diffused region, which was partially contacted with the LD technique through an Al_2O_3 layer, forming a high doped region (p^{++}). While the electron-selective contact was created with the LD technique through a phosphorous doped amorphous silicon (a-SiC_x(n)) film. The IBC solar cell achieves an efficiency of 20.8% [19], being the basis for the TMO-based devices involved in this Thesis, as can be seen in Figure 1.6.

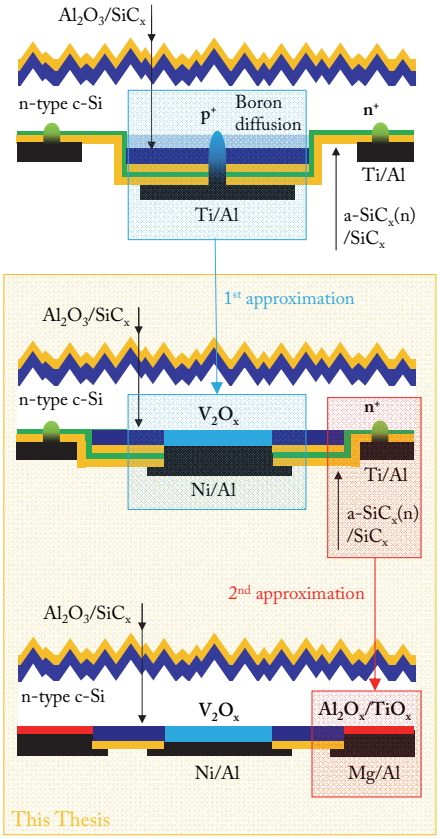

Figure 1.6 Cross-section of the reference IBC solar cell structure (top) and the TMO-based cells. Firstly, the boron diffusion was replaced by a V_2O_x-based contact (middle), and then the a-SiC_x(n) laser-doped contact was replaced by a TiO_2-based contact (bottom).

To achieve the objective of the Thesis -development of IBC c-Si solar cells based on TMOs- the work has been divided into the following parts:

The first part/approximation was the replacement of the hole-selective contact, i.e. p^+ boron diffused region and p^{++} laser-doped selective contact, for a TMO-based compound. Considering the good results obtained by the MNT group using

V_2O_x films as hole-selective contacts, this compound was selected and its properties were optimised for an IBC structure. In this way, the physical/chemical and electrical characterisation of V_2O_x films together with the capping metal material were studied. As a main result of this part, an IBC solar cell with an efficiency of 19.7% was obtained [26].

The second part/approximation, considering the previous structure of the IBC, was the study of an electron-selective contact based on TMOs to replace the laser-doped n^+ regions. In this Thesis, a new film based on TiO_x deposited by atomic layer deposition (ALD) technique is proposed as an electron-selective contact. The physical, chemical and electrical characterisation of the TiO_x films together with the capping metal material were investigated. In this way, a fully low-temperature dopant-free IBC solar cell was fabricated with a remarkable efficiency of 19.1% [27], using an Ni-capped V_2O_x film and an Mg-capped Al_2O_x/TiO_x stack as hole- and electron-selective contacts, respectively. The fabrication was simplified by avoiding the use of both thermal silicon oxide and amorphous silicon films in the structure of the carrier-selective contacts.

1.4 Structure of the Thesis

The Thesis is divided into the following Chapters:

Chapter 1: Introduction. This Chapter explains the motivation and objectives of the Thesis in order to obtain a step forward in high efficiency solar cells using transition metal oxide as selective contacts in combination with an interdigitated back-contacted cell architecture. At the end of this Chapter, the structure of the Thesis is described.

Chapter 2: Background of the Thesis. This Chapter deals with the basic fundamentals related to solar cells and transition metal oxide (TMO) materials to form selective contacts. In addition, the interdigitated back-contacted structure (IBC) is described with its pros and cons. Finally, the state-of-the-art for c-Si solar cells based on TMOs as hole-selective contacts and/or TMOs as electron-selective contacts, as well as those based on the IBC structure, are seen in detail.

Chapter 3: Experimental and characterisation methods. This Chapter explains the baseline fabrication process involved in the different interdigitated back-contacted c-Si solar cells as well as the test structures used during the Thesis. Moreover, the different techniques to measure and characterise such devices are explained in detail.

Chapter 4: Vanadium oxide as hole-selective contact. This Chapter explores the use of vanadium oxide (V_2O_x) capped with a thin nickel layer as a hole transport layer (HTL). V_2O_x/Ni test samples demonstrate saturation current density and specific contact resistance values below 200 fA/cm^2 and 120 mΩcm^2, respectively. This HTL was applied to a c-Si solar cell with an interdigitated back-contacted cell structure reaching an efficiency of up to 19.7%.

Chapter 5: Titanium oxide as electron-selective contact. This Chapter explores the use of titanium oxide together with an ultrathin alumina (Al_2O_x/TiO_x) stack capped with a thin magnesium film as an electron transport layer (ETL). Al_2O_x/TiO_x/Mg test samples demonstrate saturation current density and specific contact resistance values below 140 fA/cm^2 and 2.5 mΩcm^2, respectively. This ETL stack was applied to an interdigitated back-contacted (IBC) structure reaching a fully-TMO based IBC c-Si solar cell with an efficiency beyond 19%.

Chapter 6: Conclusions and future work. This Chapter summarises the main results and conclusions of this Thesis, as a result of the design, manufacture and

characterisation of interdigitated back-contacted c-Si solar cells based on transition metal oxides as selective contacts.

Appendix: List of publications. This Chapter describes the most important research work accomplished during the Thesis. The abstracts of the publications, as a main author, are included for the readability of the Chapter.

1.5 References

[1] W. Shockley and H. J. Queisser, "Detailed Balance Limit of Efficiency of *p-n* Junction Solar Cells," *J. Appl. Phys.*, vol. 32, no. 3, pp. 510–519, Mar. 1961.

[2] J. Zhao, A. Wang, P. P. Altermatt, S. R. Wenham, and M. A. Green, "24% efficient perl silicon solar cell: Recent improvements in high efficiency silicon cell research," *Sol. Energy Mater. Sol. Cells*, vol. 41–42, pp. 87–99, Jun. 1996.

[3] A. W. Blakers, A. Wang, A. M. Milne, J. Zhao, and M. A. Green, "22.8% efficient silicon solar cell," *Appl. Phys. Lett.*, vol. 55, no. 13, pp. 1363–1365, Sep. 1989.

[4] R. A. Sinton, Young Kwark, J. Y. Gan, and R. M. Swanson, "27.5-percent silicon concentrator solar cells," *IEEE Electron Device Lett.*, vol. 7, no. 10, pp. 567–569, Oct. 1986.

[5] M. A. Green, "The path to 25% silicon solar cell efficiency: History of silicon cell evolution," *Prog. Photovoltaics Res. Appl.*, vol. 17, no. 3, pp. 183–189, May 2009.

[6] K. Yoshikawa *et al.*, "Silicon heterojunction solar cell with interdigitated back contacts for a photoconversion efficiency over 26%," *Nat. Energy*, vol. 2, no. 5, p. 17032, Mar. 2017.

[7] National Renewable Energy Laboratory of the U.S. Department of Energy (NREL), "Best Research-Cell Efficiency Chart." [Online]. Available: https://www.nrel.gov/pv/cell-efficiency.html. [Accessed: 08-Apr-2019].

[8] H. Savin *et al.*, "Black silicon solar cells with interdigitated back-contacts achieve 22.1% efficiency," *Nat. Nanotechnol.*, vol. 10, no. 7, pp. 624–628, Jul. 2015.

[9] C. Battaglia, A. Cuevas, and S. De Wolf, "High-efficiency crystalline silicon solar cells: status and perspectives," *Energy Environ. Sci.*, vol. 9, no. 5, pp. 1552–1576, May 2016.

[10] E. L. Ratcliff, B. Zacher, and N. R. Armstrong, "Selective Interlayers and Contacts in Organic Photovoltaic Cells," *J. Phys. Chem. Lett.*, vol. 2, no. 11, pp. 1337–1350, Jun. 2011.

[11] M. T. Greiner, M. G. Helander, W.-M. Tang, Z.-B. Wang, J. Qiu, and Z.-H. Lu, "Universal energy-level alignment of molecules on metal oxides," *Nat. Mater.*, vol. 11, no. 1, pp. 76–81, Jan. 2012.

[12] UNSW Hoex Group, "Carrier selective contacts for silicon solar cells." [Online]. Available: https://unswhoexgroup.com/research/carrier-selective-contacts-for-silicon-solar-cells/. [Accessed: 19-Apr-2019].

[13] P. Ortega *et al.*, "An IBC solar cell for the UPC CubeSat-1 mission," in *2013 Spanish Conference on Electron Devices*, 2013, pp. 333–336.

[14] E. Calle *et al.*, "High efficiency interdigitated back-contact c-Si(p) solar cells," in *2015 10th Spanish Conference on Electron Devices (CDE)*, 2015, pp. 1–4.

[15] P. Ortega *et al.*, "Crystalline silicon solar cells beyond 20% efficiency," in *Proceedings of the 8th Spanish Conference on Electron Devices, CDE'2011*, 2011, pp. 1–4.

[16] I. Martin, M. Labrune, A. Salomon, P. Roca i Cabarrocas, and R. Alcubilla, "Laser fired contacts applied to the rear surface of heterojunction silicon solar cells," *Sol. Energy Mater. Sol. Cells*, vol. 95, no. 11, pp. 3119–3123, Nov. 2011.

[17] P. Ortega *et al.*, "p-type c-Si solar cells based on rear side laser processing of Al2O3/SiCx stacks," *Sol. Energy Mater. Sol. Cells*, vol. 106, pp. 80–83, Nov. 2012.

[18] G. López *et al.*, "Base contacts and selective emitters processed by laser doping technique for p-type IBC c-Si solar cells," *Energy Procedia*, vol. 77, pp. 752–758, Aug. 2015.

[19] G. Masmitja, P. Ortega, I. Martín, G. López, C. Voz, and R. Alcubilla, "IBC c-Si(n) Solar Cells Based on Laser Doping Processing for Selective Emitter and Base Contact Formation," *Energy Procedia*, vol. 92, pp. 956–961, Aug. 2016.

[20] I. Martín *et al.*, "c-Si Solar Cells based on Laser-processed Dielectric Films," *Energy Procedia*, vol. 55, pp. 255–264, Jan. 2014.

[21] I. Martín, A. Coll, G. López, P. R. Ortega, J. M. López-González, and R. Alcubilla, "DopLa Solar Cells with Texturized Front Surface," *Energy Procedia*, vol. 92, pp. 949–955, Aug. 2016.

[22] G. López, P. R. Ortega, I. Martín, C. Voz, A. Orpella, and R. Alcubilla, "'Cold' Process for IBC c-Si Solar Cells Fabrication," *Energy Procedia*, vol. 92, pp. 652–660, Aug. 2016.

[23] P. Ortega *et al.*, "Fully low temperature interdigitated back-contacted c-Si(n) solar cells based on laser-doping from dielectric stacks," *Sol. Energy Mater. Sol. Cells*, vol. 169, pp. 107–112, Sep. 2017.

[24] L. G. Gerling *et al.*, "Transition metal oxides as hole-selective contacts in silicon heterojunctions solar cells," *Sol. Energy Mater. Sol. Cells*, vol. 145, pp. 109–115, Feb. 2016.

[25] L. G. Gerling, G. Masmitja, P. Ortega, C. Voz, R. Alcubilla, and J. Puigdollers, "Passivating/hole-selective contacts based on V2O5/SiOx stacks deposited at ambient temperature," *Energy Procedia*, vol. 124, pp. 584–592, Sep. 2017.

[26] G. Masmitjà *et al.*, "V 2 O x -based hole-selective contacts for c-Si interdigitated back-contacted solar cells," *J. Mater. Chem. A*, vol. 5, no. 19, pp. 9182–9189, 2017.

[27] G. Masmitjà *et al.*, "Interdigitated back-contacted crystalline silicon solar cells with low-temperature dopant-free selective contacts," *J. Mater. Chem. A*, vol. 6, no. 9, pp. 3977–3985, 2018.

[28] G. Masmitja *et al.*, "Boron diffused emitters passivated with Al<inf>2</inf>O<inf>3</inf>films," in *Proceedings of the 2013 Spanish Conference on Electron Devices, CDE 2013*, 2013.

2 Background of the Thesis

This Chapter deals with the basic fundamentals related to solar cells and transition metal oxide (TMO) materials to form selective contacts. In addition, the interdigitated back-contacted (IBC) structure is described with its pros and cons. Finally, the state-of-the-art for c-Si solar cells based on TMOs as hole-selective contacts and/or TMOs as electron-selective contacts, as well as those based on the IBC structure, are seen in detail.

2.1 Theory of solar cells

A solar cell consists basically of an absorbent region, composed of a semiconductor material, where the light radiation is converted into electrical energy by absorption of photons causing the photogeneration of electron-hole pairs. For a net current to flow through the connected external circuit, electrons and holes must be separately extracted from the region of the absorber using two additional regions/contacts. Figure 2.1 shows a conventional solar cell structure, with a crystalline silicon (c-Si) absorber and two selective contacts formed by high-doped p^+ and n^+ regions.

The name of these regions is under discussion nowadays. Cuevas [1] has proposed a specific terminology for them, calling them *hole collector* and *electron collector*, replacing the classical names routinely applied to n-type c-Si substrates, *emitter* and *back surface field* regions, respectively (see Figure 2.1). In the same way, Würfel calls these regions *semipermeable membranes* [2], emphasising the required selectivity behaviour.

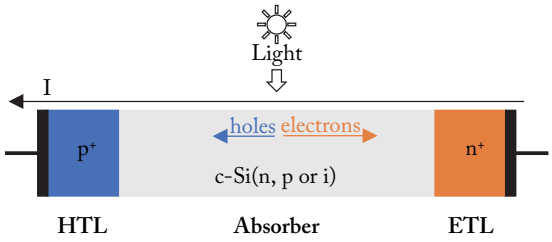

Figure 2.1 Sketch of a crystalline silicon solar cell, which is essentially formed by an absorber, n- or p-type or undoped (intrinsic), and their respective hole (p^+) and electron (n^+) collector regions.

The selectivity of the contacts can be easily explained from an energy point of view by means of energy barriers. Figure 2.2 shows the energy-band diagram of a solar cell with the structure mentioned above. The photo-generated electrons can flow towards the right, through the electron collector, or electron transport layer (ETL). Nevertheless, electrons can not flow to the left due to the large energy barrier, which results in an electron-blocking layer. In the same way, but opposed, the photo-generated holes are rejected by the ETL because of the energy barrier, but they can flow towards the left, through the hole collector, or hole transport layer (HTL).

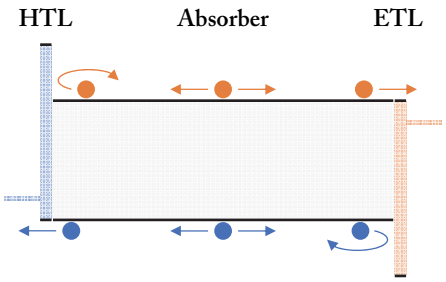

Figure 2.2 The ETL on the right allows photo-generated electrons in the absorber, to flow to the right, while blocking the holes. The HTL allows holes to flow to the left, blocking the electrons.

2.1.1 The absorber

Although all materials absorb light in some manner, not all of them are good enough candidates to be used as absorbers in solar cells.

The absorption of a photon with energy hf by an electron causes a temporal increment of its energy, being h and f the Plank's constant and light frequency, respectively. In the case of metals, since the range of energy in which electrons are allowed is continuous (see Figure 2.3), the light-excited electron quickly thermalizes to its original energetic state (relaxation) by generating phonons (E_P). In fact, the generation of phonons is an almost instantaneous phenomenon, so there is nearly no time to extract the electrons from the metals, allowing a theoretical poor power conversion efficiency [2].

Semiconductors, on the other hand, exhibit a totally different behaviour due to the existence of a bandgap energy (E_G), in which there are not energy states and the electrons are not allowed. Therefore, the relaxation of electrons by emitting phonons is interrupted (see Figure 2.3). The electrons in the valence band, with energies below the valence energy edge (E_V), can reach the conduction band, with energies higher the conduction energy edge (E_C), by the absorption of photons.

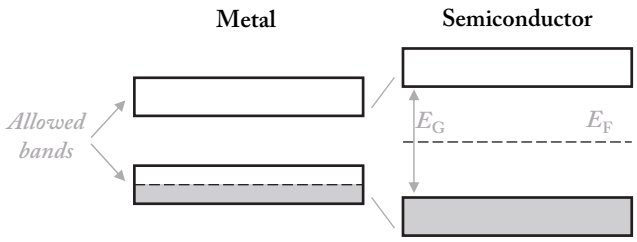

Figure 2.3 Basic energy-band diagram of a metal and a semiconductor. Adapted from [3] *© 1998 The University of New South Wales.*

The semiconductor energy-band structure, which is represented in Figure 2.4, permits the photo-generated electron-hole pairs to remain temporally in the conduction and valence band, respectively, in a non-equilibrium state. In this way, carriers can reach the contacts without hardly recombining in the absorber, producing a net photocurrent.

Another important parameter to understand the semiconductor energy-band diagram is the Fermi energy level (E_F). The Fermi distribution statistics are used to represent the probability of occupation of the energy states in the conduction or valence bands by electrons or holes, respectively. Doping the semiconductor is a common way to control the concentrations of electrons in the conduction band (electron conductor or n-type) or holes in the valence band (hole conductor or p-type), which is to modulate the conductivity of the semiconductor. Therefore, for a n-type or a p-type semiconductor the E_F is near the E_C or E_V energy levels, respectively. In addition, for illuminated semiconductor, i.e. non-equilibrium state, there are two Fermi energy levels, one for electrons (E_{Fn}) and the one for holes (E_{Fp}).

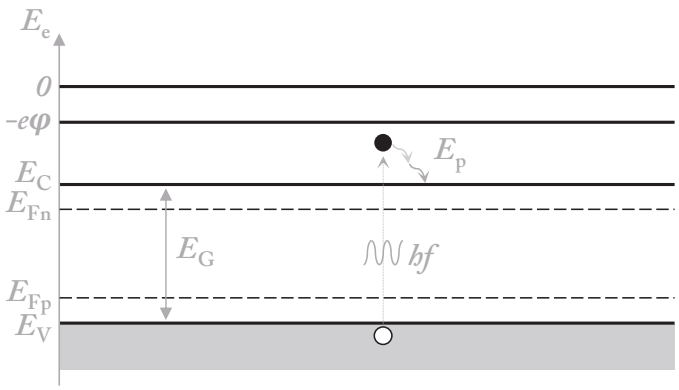

Figure 2.4 Energy-band diagram of a semiconductor.

Photogeneration of an electron-hole pair requires the photon energy to be higher than the gap energy of the semiconductor material ($hf \geq E_G$) [3]. Then, when light passes through the semiconductor the photons are absorbed inside the material following an exponential profile, i.e. the substantial photo-generated carriers are produced near the surface. The most frequent approach to calculate that profile is by using the absorption law of Lambert-Beer, in which the density of the photon flux after passing a distance x in a film with an absorption coefficient $\alpha(\lambda)$ is reduced with a factor $e^{-\alpha(\lambda)x}$. This coefficient depends on the light wavelength and the substrate material. The higher the value of α the shorter the distance to absorb the photons in the substrate.

Direct bandgap semiconductors as Cadmium Telluride (CdTe) or Chalcogenides (CIGS and CIS) solar cells have a high α coefficient in the useful part of the solar spectrum. Therefore, in this case solar cells can be manufactured very thin, with a typical 1-2 μm thick absorber. In contrast, indirect bandgap semiconductors like Si and germanium (Ge), the small value of α requires thicker substrates, as photons are absorbed deep into the substrate. Thus, solar cells typically have more than a 100 μm thick substrate to obtain a reasonable light absorption.

In all cases, it is important to increase the photon absorption probability by reducing reflectance losses on the front surface, as can be seen in Figure 2.5. In this way, a front surface texturization scheme [4], [5] complemented with an antireflective coating film [5] is typically used. Additionally, a back-reflector scheme reduces the escape of photons on the rear surface, which increases the capture of light inside the absorber.

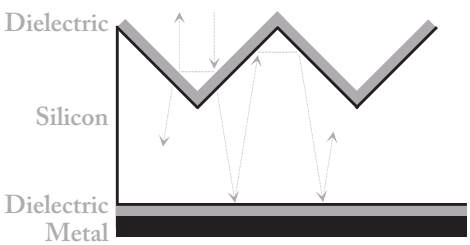

Figure 2.5 Reduction of optical losses by including a textured front surface and an antireflection coating film (ARC) together with a black reflector scheme (dielectric + metal).

Once the electron-hole pairs are generated by the absorption of light, if the light is switched off, these concentrations decay back to their equilibrium values. The process in which electrons and holes decay, after a characteristic time (lifetime), is known as recombination. The total of recombination can be characterised by an effective lifetime (τ_{eff}), which depends on the lifetime related to bulk (τ_b) and surface (τ_s) recombination, as Eq. (2.1) describes. Thus, a maximum lifetime can be obtained, i.e. higher solar cell efficiencies, by reducing bulk and surface recombination mechanisms.

$$\frac{1}{\tau_{eff}} = \frac{1}{\tau_b} + \frac{1}{\tau_s} \tag{2.1}$$

Figure 2.6 summarises the different recombination processes involved in the bulk and the surface of a semiconductor. Regarding bulk recombination, there are several mechanisms which act at the same time. On the one hand, there is a mechanism associated to a recombination via impurities or traps in the bandgap, which is known as the Shockley-Read-Hall (SRH) recombination process [6]. The associated lifetime (τ_{SRH}) and the diversity of possible dependence with temperature and the minority carrier injection-levels was reported by Rein [7]. However, this mechanism is negligible for high quality c-Si substrates.

On the other hand, it is possible that an electron in the conduction band recombines directly with a hole in the valence band by emitting a photon (radiative recombination) or giving the excess energy to a second electron (Auger recombination). Both recombination mechanisms are inherent to semiconductors and they are referred to as intrinsic recombination mechanisms, determining the upper limit efficiency of solar cells. The lifetime related to intrinsic recombination processes (τ_{in}) depends strongly on doping, carrier excess and temperature. A recent parametrisation of τ_{in} is given by Richter [8] based on the most recent improvements on c-Si passivation surfaces, which has allowed the investigation of the silicon intrinsic bulk recombination with an improved precision.

Regarding surface recombination, recombination on the semiconductor surface is typically characterised by a surface recombination velocity parameter (*S*). A high rate of recombination occurs on the surface by SRH mechanisms due to the existence of dangling bonds on the ended lattice atoms. In fact, surface passivation techniques are used in solar cells to reduce this recombination as much as possible, being one of the most important design characteristics to obtain highly efficient devices.

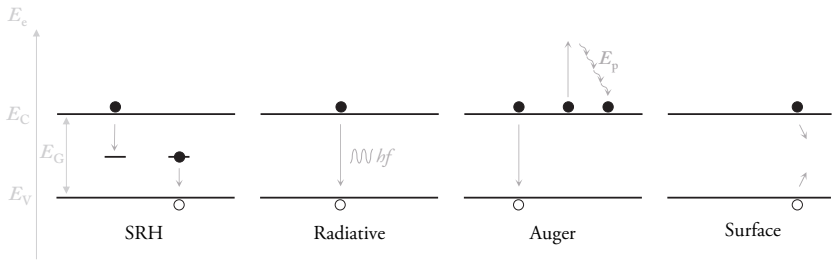

Figure 2.6 Two-step recombination process (SRH mechanisms), radiative recombination with associated photon emission, auger recombination with associated excess energy given to a second electron and surface recombination mechanism.

2.1.2 The carrier collectors

In an electron-selective contact the electrons exhibit a high conductivity, while holes are rejected back to the absorber, i.e. no recombination on the surface, or alternatively, a very-low hole conductivity. An opposite behaviour for electrons and holes occurs in hole-selective contacts, i.e. high conductivity for holes and low recombination and/or low conductivity for electrons. Therefore, the photo-generated electron-hole pairs can be separately extracted, maximising the total current density (J).

The J is due to the motion of the photo-generated carriers inside the semiconductor into the contacts by both diffusion (nonuniform carrier concentration) and drift (electric field) transport mechanisms. This can be calculated from the gradient of pseudo-Fermi energy levels of electrons and holes, respectively, E_{Fn} and E_{Fp}, as follows:

$$J = \frac{\sigma_n}{q} grad(E_{Fn}) + \frac{\sigma_p}{q} grad(E_{Fp}) \tag{2.2}$$

where q is the elementary charge and σ_n and σ_p are the electron and hole conductivity, respectively [2].

Figure 2.7 shows the energy-band diagram of an illuminated n-type semiconductor contacted with electron-selective contacts on both surfaces, under short-circuit condition. Because of the high conductivity of electrons at the ETL regions, the gradient of the E_{Fn} required to drive the electrons to the contacts is negligibly small, as followed in Eq. (2.2).

In contrast, the very small hole concentration in that region, i.e. low hole conductivity, leads an unappreciable hole current to the contact, although there is a large gradient of the E_{Fp}. Finally, the metal contact forces the Fermi energies to join on the surfaces.

As a result, the electrons in above mentioned structure (Figure 2.7) do not move in any preferred direction, resulting in a no photogeneration of current. However, if the left contact is replaced by a hole-selective contact, then the electrons and holes have a preferred direction. Therefore, they separately move to the right (electrons) and left (holes) contacts, giving a net current density flowing outside the semiconductor. Figure 2.8 shows the energy-band diagram under short-circuit conditions for this asymmetric structure.

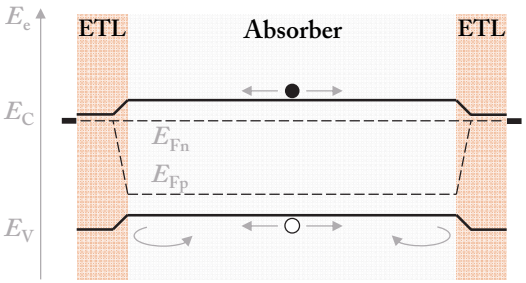

Figure 2.7 Energy-band diagram of a homogeneously illuminated n-type semiconductor, symmetrically contacted with electron-selective contacts.

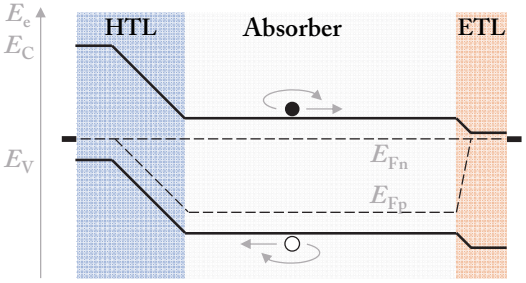

Figure 2.8 Energy-band diagram of a homogeneously illuminated n-type semiconductor, contacted with a hole-selective contact on the left and an electron-selective contact on the right. Under short-circuit condition.

In order to characterise the selective behaviour of a contact, two important parameters are typically used in the literature. One of them, the specific contact resistance (r_c) in Ωcm^2 units, which measures the conductivity in the selective contact for the non-blocked carrier. The other parameter is the contact recombination current density (J_{0c}) in fA/cm^2 units, which measures the level of selectivity for the blocked carrier. Good contacts are characterised by simultaneously low r_c and J_{0c} values.

If the electrical performance of the solar cell is limited by the contacts, then the simplified model shown in Figure 2.9 can be used. In that case, the current density-voltage (J-V) characteristic is modelled by Eq. (2.3) assuming that electrical behaviour is completely dominated by the r_c and the J_{0c} values.

$$J = J_L - J_{0c}\left(e^{\frac{V+J\cdot r_c}{V_{th}}} - 1\right) \tag{2.3}$$

where J_L and V_{th} are the photocurrent density and thermal voltage parameters, respectively.

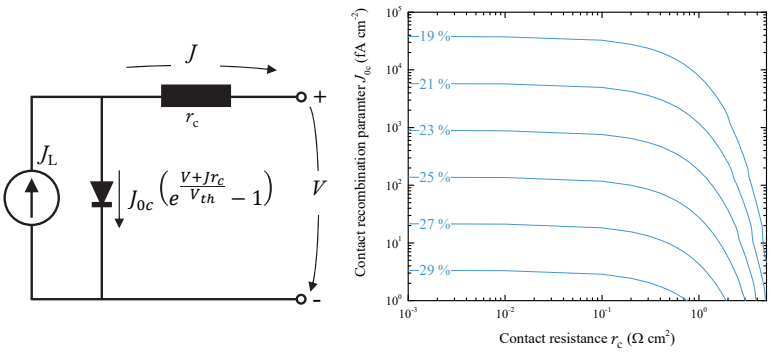

Figure 2.9 Left, the equivalent circuit of a solar cell characterised by a selective contact with a recombination (J_{0c}) and contact resistance (r_c) parameters. Right, the photovoltaic efficiency contours as a function of r_c vs. J_{0c} parameters using the foregoing electrical model.

With this simple solar cell model, an upper limit of the photovoltaic efficiency can be calculated considering both r_c and J_{0c} as free parameters in the study, as can be seen in Figure 2.9 assuming a fixed photo-generated current density, i.e. independently of contact quality, of J_L = 43.33 mA/cm^2 and assuming fully contacted devices. The chosen J_L value is a representative maximum value for c-Si solar cells under AM1.5G solar spectrum (1 kW/m^2) [9].

For low values of r_c (< 0.1 Ωcm^2), the J_{0c} parameter is the main contribution factor in efficiency. Otherwise, for large values of r_c (> 1 Ωcm^2), efficiency decays dramatically even for low J_{0c} values. Theoretical efficiencies higher than 25% are envisaged for J_{0c} values below 100 fA/cm^2 and a reasonable r_c value (< 0.1 Ωcm^2).

Some authors have incorporated both the r_c and the J_{0c} parameters in a single-figure of merit to quantify the contact quality. In this way, Brendel [10] suggests the so-called contact selectivity parameter (S_{10}) defined as:

$$S_{10} = log\left(\frac{V_{th}}{J_{0c}r_c}\right) \tag{2.4}$$

Alternatively, Bullock [11] suggests the so-called "upper-limit" maximum power voltage ($V_{C,UL}$) as:

$$V_{C,UL} = V_{th} ln\left(\frac{J_L}{J_{0c}}\right) - J_L r_c \tag{2.5}$$

In both cases, the higher S_{10} and/or $V_{C,UL}$ values means a better contact selectivity, therefore, higher solar cell efficiencies.

2.2 Photovoltaic parameters of solar cells

Figure 2.10 depicts the equivalent circuit (two-diode model) of a solar cell and its dark and light current-voltage (*I-V)* characteristics [2]. Considering this model, Eq. (2.6) determines the leaving current from the solar cell.

The D_1 and D_2 diodes consider recombination losses, being I_{01} and I_{02} their representative recombination current. The D_1 corresponds to the ideal diode (ideality factor of n = 1). The second diode, D_2 with n = 2, is included in the model in order to consider extra recombination losses, e.g. device edge recombination losses or/and recombination in a space charge region.

The lumped resistances R_{sh} and R_s consider any shunt resistances, e.g. pinholes between the metal contact and absorber, and series resistances, e.g. resistance of metal fingers, respectively.

$$I(V) = I_L - I_{01}\left(e^{\frac{V-I\cdot R_S}{V_{th}}} - 1\right) - I_{02}\left(e^{\frac{V-I\cdot R_S}{2\cdot V_{th}}} - 1\right) - \frac{V-I\cdot R_S}{R_{sh}} \tag{2.6}$$

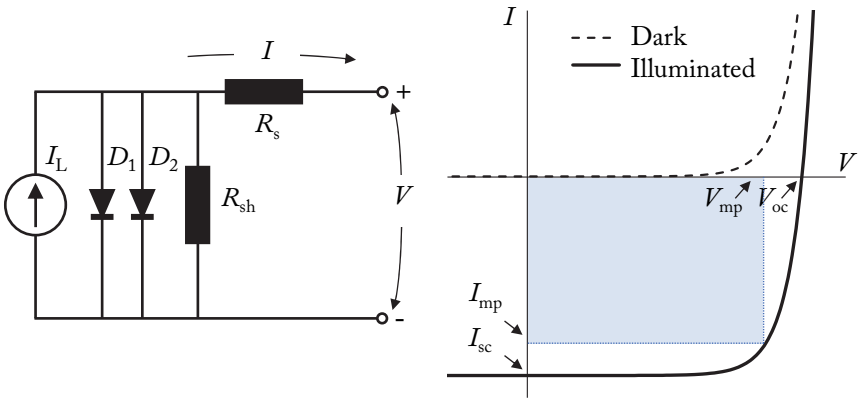

Figure 2.10 Left, the equivalent circuit of a solar cell (two-diode model). Right, the dark and light I-V curves. Ideally, the I_{sc} is equal to the photo-generated current (I_L).

Equation (2.7) is a more compacted expression where the two dark diodes are simplified to a single diode with an effective recombination current density and ideality factor, I_0 and n, the values of which are in general voltage-dependent.

$$I(V) = I_L - I_0\left(e^{\frac{V-I\cdot R_S}{n\cdot V_{th}}} - 1\right) - \frac{V-I\cdot R_S}{R_{sh}} \tag{2.7}$$

Solar cell characterisation usually involves three parameters, which determine the device's performance. The first is the short-circuit current (I_{sc}), setting V to zero in Eq. (2.7), which is ideally equal to the I_L current, i.e. low series resistance losses.

The second important parameter is the open-circuit voltage (V_{oc}) resulting from set I to zero in Eq. (2.7) and avoiding shunt ohmic losses, i.e. $R_{sh}\rightarrow\infty$.

$$V_{oc} = nV_{th}\cdot\ln\left(\frac{I_L}{I_0}+1\right) \tag{2.8}$$

The third parameter is the Fill Factor (*FF*), which is defined as the ratio between the maximum power (*mp*) delivered by the cell, $V_{mp}\cdot I_{mp}$, and the $V_{oc}\cdot I_{sc}$ product, i.e. the maximum available power. That parameter specifies the "squareness" of the light *I-V* curve (see Figure 2.10), hence its name, being its value less than one.

$$FF = \frac{V_{mp}\cdot I_{mp}}{V_{oc}\cdot I_{sc}} \tag{2.9}$$

Finally, using the foregoing photovoltaic parameters and considering the total incident light power on the solar cell (P_{in}), the energy-conversion efficiency (η) can be calculated as:

$$\eta = \frac{V_{oc}\cdot I_{sc}\cdot FF}{P_{in}} \tag{2.10}$$

2.3 Selective contact technology approaches

The dopant-diffused pn-Junction (pnJ), is the *classic* way to achieve carrier-selective contacts on n-type c-Si substrates (the energy-band diagram of a typical pnJ is represented in Figure 2.11), yielding efficiencies beyond 25% on lab solar cells [12]. The same efficiency was reported by the SunPower Corporation [13], for a large area (121 cm^2) using an industrial process. In fact, dopant-diffused contacts dominate nowadays the c-Si photovoltaic industry.

Nevertheless, interesting alternatives have emerged over the last years by lowering processing temperatures. The doping on the pnJ structure needs to be performed at high temperatures (beyond 800 ^oC), which requires complex and energy consuming processes and lengthy cleaning protocols to avoid possible degradations of the bulk c-Si lifetime.

The well-known silicon heterojunction structure (SHJ) (see Figure 2.11), which uses doped and intrinsic hydrogenated amorphous silicon (a-Si:H(i /n or p)) films as selective contacts, has proven to be an excellent alternative for the manufacturing of solar cells at low-temperature (typically 300 ^oC). The Panasonic Corporation [14] reported an efficiency of 25.6% with 143.7 cm^2 active area, using a SHJ structure. However, this structure uses toxic and flammable gases as dopant precursors. Therefore, it is necessary to use complex equipment again, increasing the number of steps involved in the production process and consequently the cost.

As an alternative to the SHJ structure as a low-temperature technology, there is a technology based on the laser-processing of dielectric thin-films, the Doped by Laser (DopLa) approach [15]. Using this concept, the Micro and Nano-Technologies group (MNT) [16] reported an efficiency of 20.4% using an Al_2O_3 layer as a source of dopant for the hole-selective contact. However, the efficiency does not achieve higher values probably due to the degradation of the surface passivation during the laser step and/or deficient contact passivation.

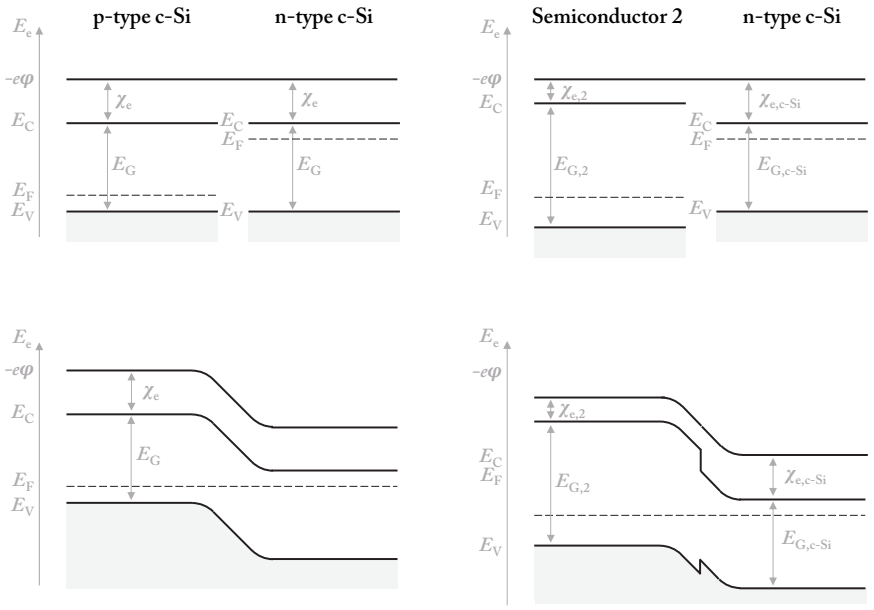

Figure 2.11 Left, Energy-band diagrams of p- and n-type c-Si prior to making contact (top) and in contact (bottom). Right, Energy-band diagrams of different semiconductors prior to making contact (top) and after contact (bottom) at equilibrium. The difference between the vacuum level ($-e\varphi$) and E_C is the so-called electron affinity (χ_e).

Research on dopant-free c-Si solar cells is an emerging research topic that uses the so-called DASH approach (Dopant Free Asymmetric Heterocontacts) [17], where the carrier selectivity is achieved by using alternative materials: organic polymers [18], metal salts [17], [19], [20] and transition metal oxides (TMOs) [21], [22]. This new paradigm extends the technological possibilities and multiple options are actively being explored to achieve the best balance between efficiency and simplicity [23].

These interesting alternatives comes mostly from organic photovoltaic technology, where the TMOs, for instance, are often used as semipermeable membranes to selectively extract carriers form a semiconductor light absorber [24].

Among others, the TMOs are becoming very attractive due to the combination of the wide range of work-functions offered (from 3 to 7 eV) and the large bandgap (E_G >3 eV) and consequently high optical transparency, which overcome the J_{sc} losses in the SHJ structure due to the light absorption in the films of a-Si:H [25]. Figure 2.12 shows a list of commonly used TMOs, together with its energy-level diagram (adapted from [24]). Energy level of crystalline silicon is also plotted, together with the work-function of several metals.

TMOs with a high work-function (Φ >7 eV), such as molybdenum oxide (MoO_x), tungsten oxide (WO_x) and vanadium oxide (V_2O_x) are preferred as hole-selective contacts [22], while low work-function compounds (<4 eV) such as magnesium oxide (MgO_x) [26], and titanium oxide (TiO_x) [27] are being investigated as electron-selective contacts.

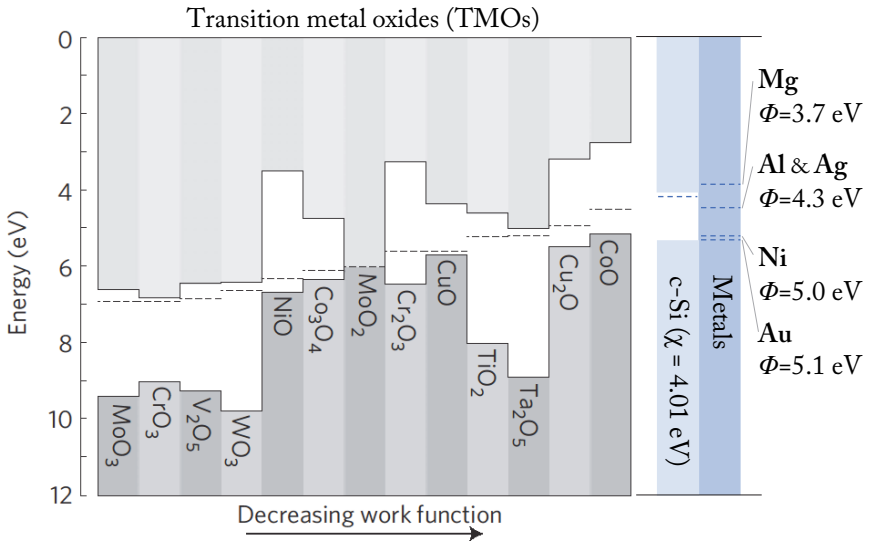

Figure 2.12 Energy level diagrams of some transition metal oxides (TMOs), metals and the crystalline silicon (c-Si) on an absolute energy scale. The lower and upper shaded regions represent the valence and conduction bands, respectively. The dashed black lines indicate the Fermi level position. Adapted from [24] *© 2012 Nature.*

The asymmetric conductivity in these materials is achieved either by band alignment or through a strong induced band-bending. In order to take advantage of the band structure of the silicon/contact interface while simultaneously decreasing surface recombination, it is important to avoid fermi-level pinning by reducing the density of states at the silicon interface [28]. In most cases, this is achieved by plasma enhanced chemical vapour deposition (PECVD) growth of a thin film of a-Si:H(i) between the TMO and the c-Si surface [17]. Two drawbacks overshadow this approach, the use of flammable gases and the intrinsic difficulty of obtaining good c-Si/a-Si:H(i) interfaces. Another possibility, although introducing a high temperature step, is to grow a thin tunnel SiO_2 layer between the TMO and the silicon surface [29]. The SiO_2 thickness is the result of a trade-off between contact resistance and passivation. Finally, another plausibility way is to take advantage of the in situ redox reaction during thermal evaporation of the TMO material which results in spontaneous growth of a SiO_x film [30].

In addition, the work-function and conductivity of TMOs are highly adjustable depending on their oxygen content [31], which offers an additional flexibility. Moreover, the TMOs can be deposited by using low-temperature and/or vacuum-free techniques, such as thermal evaporation, spin-on, spray-on, sputtering and atomic layer deposition (ALD), offering great adaptability when introducing them into the manufacturing processes.

2.4 Interdigitated back-contacted structure

The structure of an interdigitated back-contacted (IBC) solar cell is an old but attractive concept, which was primarily designed for concentrated photovoltaic applications. It was introduced by Schwartz and Lammert in the 1970s [32] and its schematic representation is illustrated in Figure 2.13.

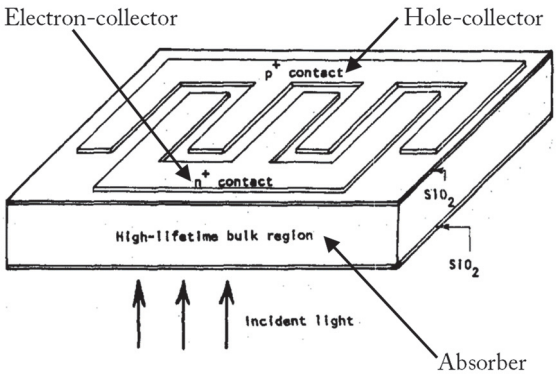

Figure 2.13 Schematic illustration of an interdigitated back contacted (IBC) solar cell. Adapted from [32] *© 1977 IEEE.*

The IBC cells have both electron- and hole-selective contacts in the back of the device. By placing the selective contacts on the rear side, not only is the passivation and antireflection scheme simplified on the front side but it also avoids shadow losses in it. In fact, high short-circuit current densities are achieved by eliminating the shading of the metal grid on the front surface.

Because of there is no need for lateral conduction across a high-resistive region, i.e. through thin-doped region or transparent conductive oxide (TCO) film, the IBC structure allows to overcome the trade-off that exist in both sides-contacted solar cells between series resistance and grid shading. Moreover, the current losses due to parasitic optical absorption in the foregoing films are also eliminated [33].

However, the IBC solar cell is a very demanding structure which requires a very high-lifetime absorber and an exceptional surface passivation to reduce both bulk and surface recombination, which is mandatory because a large part of the photons are absorbed near the front surface. Therefore, photo-generated carriers must travel more than the wafer thickness before being collected at their respective electrodes.

The IBC structure has also been commercially introduced and optimised for the applications under standard one-sun operation. In the 1980s the photovoltaic group at Stanford University, USA [34], achieved an efficiency of 22.3% for diffused junctions IBC devices (pnJ-IBC), which was later used in the industry by Sunpower, USA [35] with a remarkable cell efficiency of 25.2%.

In fact, the recent world record efficiency for crystalline silicon solar cells has been obtained by Kaneka Corporation, Japan, using an SHJ-IBC structure with a cell efficiency of 26.6% [36].

2.5 State-of-the-art

2.5.1 Interdigitated back-contacted solar cells

In recent years, several carrier-selective contact technologies applied to IBC c-Si solar cells have been introduced and optimised. Table 2.1 summarises the main photovoltaic parameters for IBC cells with remarkable power conversion efficiencies and Figure 2.14 shows their efficiencies *vs.* the reported year.

As mentioned before, high efficiency was achieved in the 1980s by a photovoltaic group from Stanford University, USA [34] with an efficiency of up to 22.3% using a pnJ-IBC scheme. More recently, other institutions have also reported efficiencies over 20% using pnJ-IBC structures: the International Solar Energy Research Center (ISC) [37], [38] and the Fraunhofer Institute for Solar Energy Systems (F-ISE) [39], both from Germany, the Australian National University (ANU), Australia [40], the Institute for Solar Energy Research Hamelin (ISFH), Germany [41] and our group (MNT) at the Universitat Politècnica de Catalunya (UPC), [4].

The SHJ concept has also been applied successfully to IBC devices, as an alternative to diffused junctions. Remarkable efficiencies of over 20% have been reported, namely: The École Polytechnique Fédérale de Lausanne (EPFL), Switzerland [42], the Helmhotz-Zentrum Berlin (HZB), Germany [43], the Institut National de l'Energie Solaire (INES), France [44] and the Interuniversitair Micro-Electronic Centrum (IMEC), Belgium [45].

The introduction of the IBC structure in the industry as a feasible high efficiency cost-effective solar cell product is a reality nowadays. As mentioned above, the world record efficiency has been obtained by Kaneka with an SHJ-IBC structure with an efficiency of 26.3% [36]. Panasonic, Japan [14] and Sharp, Japan [46] have also achieved excellent values, over 25% with SHJ-IBC schemes. Other industrial approaches based on pnJ-IBC devices have been developed by companies such as Trina Solar, China [47] and Sunpower, USA [35], with remarkable efficiencies of 23.5% and 25.2%, respectively.

The above results demonstrate that the IBC concept is a promising structure applied to c-Si solar cells, which could achieve high conversion efficiencies at a competitive cost.

At present, researchers focus their efforts to high-efficient devices using simplified manufacturing processes. In this way, the technique based on laser processed films, to carry out diffused regions into the c-Si substrate, have been explored for IBC devices (DopLa-IBC): The Stuttgart University, Germany [48], the ANU [40] and the UPC [16] have reported notable results using this technique.

In addition, a remarkable cell efficiency of 26.1% has been reported by ISFH [49] employing doped polycrystalline silicon (poly-Si) contacts. A similar structure was studied by the F-ISE [50] with an efficiency of up to 23.7%.

Finally, to simplify the IBC manufacturing process the DASH concept was introduced yielding notable results in the last years. Um [51] from Ulsan National

Institute of Science and Technology (UNIST), Korea, reported an efficiency of 15.4% for a 1 cm^2 cell with MoO_x and LiF_x films as selective contacts. Wu [52] from Sun Yat-Sen University (SYSU), China, investigated the use of WO_x, MoO_x and V_2O_x films as hole-selective contacts in combination with caesium carbonate (Cs_2CO_3) as electron-selective contacts. This study achieved the best cell using V_2O_x films, with an efficiency of up to 16.6%. More recently, the same group reported a cell efficiency of 19% employing a V_2O_x/Au/V_2O_x stack and LiF_x film as HTL and ETL, respectively [53]. However, in this case, the front surface of the solar cell was passivated with a diffused front surface field (FSF; 200 Ω/sq).

Part of this Thesis is dedicated to obtain a DASH-IBC solar cell, in fact, this objective was achieved with a solar cell efficiency of 19.1% using an Ni-capped V_2O_x film and an Mg-capped Al_2O_x/TiO_x stack as hole- and electron-selective contacts, respectively, [54].

Finally, similarly to high efficiency both sides-contacted structures [17], a thin a-Si:H(i) layer was also used as an intermediate passivated film in an IBC structure by Wu [55]. The collaboration between SYSU and EPFL universities resulted in a solar cell with an efficiency of 22%, which used MoO_x and MgF_x films as HTL and ETL, respectively.

Table 2.1 Single-junction interdigitated back-contacted (IBC) c-Si solar cells with remarkable efficiencies. Measured under the global AM1.5 spectrum (1 kW/m² at 25 °C).

Ref.	V_{oc} (mV)	J_{sc} (mAccm^{-2})	*FF* (%)	η (%)	Selective contacts	Description	Last member institution	Year
Selective contacts based on diffusion processes (pn junction)								
[39]	697	41.2	80.0	23.0	pnJ	4 cm² cell area, front: FSF+SiO_2/Si_3N_4	F-ISE	**2012**
[37]	648	41.9	78.5	21.3	pnJ	156 cm² cell area, front: FSF	ISC	2012
[41]	686	41.3	81.6	23.1	pnJ	4 cm² cell area	ISFH	2013
[40]	702	42.0	82.7	24.4	pnJ	4 cm² cell area, front: SiN_x/SiO_x	ANU	2014
[38]	654	41.1	80.2	21.5	pnJ	239 cm² cell area, front: FSF	ISC	2015
[4]	665	42.2	78.7	22.1	pnJ	9 cm² cell area, front: Al_2O_3/black silicon	UPC	2015
[56]	721	40.5	82.9	24.2	pnJ	155 cm² cell area, front and rear text. surf.	Sun Power	2010
[57]	683	41.6	80.6	22.9	pnJ	243 cm² cell area	Trina Solar	2014
[35]	737	41.3	82.7	25.2	pnJ	153 cm² cell area, front and rear text. surf.	Sun Power	2016
[47]	690	42.1	80.9	23.5	pnJ	243 cm² cell area	Trina Solar	2016
Selective contact based on doped a-Si:H films (SHJ)								
[43]	673	39.7	75.7	20.2	SHJ	1 cm² cell area, front: FSF	HZB	**2011**
[42]	726	40.9	74	22	SHJ	9 cm² cell area, front: SiO_x/SiN_x/a-Si:H(i)	EPFL	2015
[44]	711	40.1	72.1	20.5	SHJ	18 cm² cell area, laser patterning process	INES	2016
[45]	732	41.8	74.8	22.6	SHJ	4 cm² cell area, front: SiN_x/a-Si:H(i)	IMEC	2017
[46]	736	41.7	81.9	25.1	SHJ	4 cm² cell area, front: SiN_x/a-Si:H(i/n)	Sharp	2014
[14]	740	41.8	82.7	25.6	SHJ	144 cm² cell area	Panasonic	2014
[36]	744	42.3	83.8	26.3	SHJ	180 cm² cell area	Kaneka	2017

Ref.	V_{oc} (mV)	J_{sc} (mAccm^{-2})	*FF* (%)	η (%)	Selective contacts	Description	Last member institution	Year
Selective contact based on alternative strategies								
[48]	669	41.3	79.8	22.0	DopLa	4 cm^2 cell area, boron-sputtered & $POCl_3$	Stuttgart	2013
[40]	671	41.7	68.0	19.1	DopLa	4 cm^2 cell area, spin-on dopant films	ANU	2014
[16]	654	40.6	77.0	20.4	DopLa	9 cm^2 cell area, Al_2O_3 and n-doped a-SiC_x	UPC	2017
[50]	720	41.3	79.6	23.7	Poly-Si	4 cm^2 cell area, wet-chemically grown SiO_x	ISE	2017
[49]	727	42.6	84.3	26.1	Poly-Si	4 cm^2 cell area, thermally grown SiO_2	ISFH	2018
Selective contact based on Doped free Asymmetric Selective Heterocontacts (DASH)								
[51]	5610	36.8	74.6	15.4	DASH	Thermally evaporated MoO_x and LiF_x	UNIST	2016
[52]	610	38.8	70.0	16.6	DASH	Thermally evaporated V_2O_x and Cs_2CO_3	SYSU	2016
[53]	651	38.7	75.5	19.0*	DASH	Therm. evap. V_2O_x /Au/ V_2O_x and LiF_x	SYSU	2017
[54]	633	40.0	75.4	19.1	DASH	Therm. evap. V_2O_x and ALD Al_2O_x/TiO_x	UPC	2018
[55]	709	41.5	75.6	22.2	DASH	a-Si:H(i) plus therm. evap. MoO_x & MgF_x	EPFL	2018

* With a 200 Ω/sq FSF

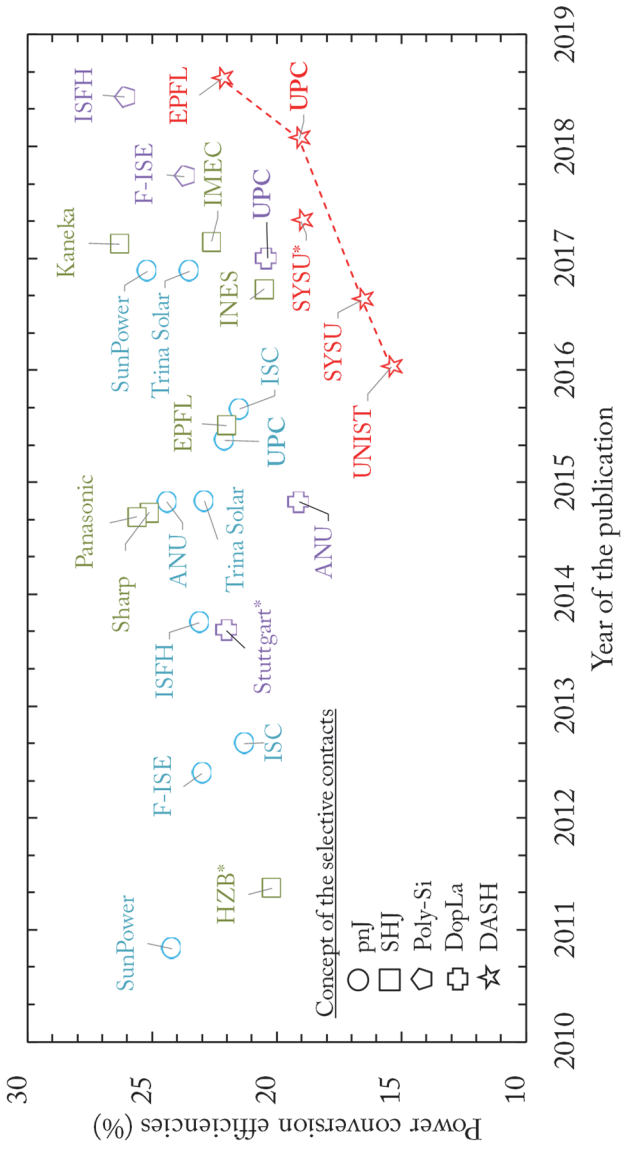

Figure 2.14 Power conversion efficiencies for IBC c-Si solar cells using different selective contact approaches. The blue circle and green square symbols mean the classical diffusion approach (pnJ) and a-Si (SHJ) based contacts, respectively. The pink hexagon and cross symbols mean alternative concepts, respectively, doped polycrystalline silicon contacts (Poly-Si) and employing the laser diffused technique (DopLa). Finally, the red stars denote the use of the dopant-free contacts by a metal compound approach for both contacts (DASH). The (*) means the use of front surface field.

2.5.2 Metal compounds as hole-selective contacts

Transition metal oxides used as hole-selective contacts have been used traditionally in organic photovoltaic technology, but nowadays, they have also become a recurring subject which is being intensively studied in c-Si solar cells. Table 2.2 summarises the main photovoltaic parameters for c-Si solar cells using TMOs with a remarkable efficiency of energy conversion and Figure 2.15 shows their efficiencies *vs.* the reported year.

The most commonly used TMOs as hole-selective contacts have been films based on MoO_x, WO_x and V_2O_x. Battaglia [58] investigated the atomic and the morphological structure of thermally evaporated MoO_x films. They suggested that the MoO_x film acts as a high work-function metal with a low density of states at the Fermi level with a measured work-function of ~6.6 eV. To demonstrate the viability, they manufactured a c-Si solar cell with a 15 nm thick MoO_x layer, achieving an efficiency of 14.3%. Then, using an a-Si:H(i) passivation layer between the oxide and the c-Si substrate, they obtained a higher cell efficiency with a value of 18.8% [59], mainly due to a higher V_{oc} value (711 mV).

Bullock [17] applied the previous MoO_x-based approach (stack of a-Si:H(i)/MoO_x) to a DASH concept solar cell with an efficiency of 19.4%, using a-Si:H(i)/LiF_x stack as an electron-selective contact. The same author, subsequently reported an efficiency improvement to 20.7% using the same approach [60]. In addition, Geissbühler [61] pushed forward the efficiency using an electrodeposited copper film as a metal front contact to avoid annealing steps above 130 ºC, as well as to substantially reduce the fingerbreadth. The result was a c-Si solar cell based on SHJ with an efficiency of 22.5%, using an a-Si:H(i)/MoO_x stack as HTL.

The MNT group at the UPC was one of the first in report (in the 29th European Photovoltaic Solar Energy Conference and Exhibition, 2014) the use of MoO_x layers as HTL on c-Si solar cells [62], obtaining a cell efficiency of 12.5%. Then in an extensive work [22] a comparative study of MoO_x, WO_x and V_2O_x films were reported, with cell efficiencies of 13.6%, 12.5% and 15.7%, respectively. Finally, in another study [30] the passivation properties of thermally evaporated TMOs were attributed to the spontaneous growth of a SiO_x film, e.g. a considerable high value of iV_{oc} (more than 630 mV) for c-Si covered with a 20 nm thick MoO_x film.

Similarly, but with the use of an a-Si:H(i) interlayer, Bivour [63] compared the selective properties of MoO_x and WO_x films, obtaining cell efficiencies of 19.0% and 17.9%, respectively. These latter efficiencies are specially notable if one considers that the devices were manufactured on polished-surface wafers, which is non-textured surface on the front, which resulted in low J_{sc} values (about 33 mA/cm^2). When the V_2O_x film was introduced in the study as HTL, the cell efficiency improves to 18.3% [64]. Surprisingly, a poor cell efficiency was obtained when the a-Si:H(i) film was introduced between the c-Si substrate and the V_2O_x film, due to a drastic drop of the *FF* value.

Complementary to the use of a-Si:H(i) passivated films, Bullock [65] explored the use of a thin chemically grown SiO_x film to passivate the interface between the c-Si substrate and the MoO_x layer, obtaining a non-textured cell with an efficiency of 16.7%. Boccard [66] also investigated the influence of the incorporation of a thin SiO_x film, which improved the current density, but led to lower *FF* values. The reported higher efficiency was without the use of this SiO_x layer with a DASH cell efficiency of 11.2%.

In this Thesis, we have fabricated IBC solar cells using HTLs based on thermally evaporated V_2O_x layers (without using an a-Si:H(i) passivation interlayer), resulting in cell efficiencies of up to 19.7% [67]. The electron-selective contact was done by laser-doped technique.

In an additional work, and as an important part of this Thesis, layers of TiO_x deposited by ALD have been optimised as ETL contact. In which, an ALD Al_2O_3 film has been used as an alternative passivation interlayer to the a-Si:H(i) films. The resultant Al_2O_x/TiO_x stack was applied to a DASH-IBC solar cell as ETL (thermally evaporated V_2O_x film was used as HTL), obtaining a cell efficiency of 19.1% [54].

The sputtering technique to deposit the TMOs, such as WO_x and NiO_x:Cu films was investigated by Mews [68] and Yang [69], with cell efficiencies of 16.6% and 9.1%, respectively. Yu [70] used an electron-beam technique to deposit the MoO_x film with a cell efficiency of 14.2%.

The use of TMOs on p-type c-Si substrates have also been reported in the literature, but not as extensively. Bullock [65] explored the use of an MoO_x film as a majority carrier contact, i.e. using p-type c-Si substrates, reporting a pnJ-based cell efficiency of 16.4%. The use of local point contacts on the rear surface improved the previous reported results, with a cell efficiency of up to 20.4% [71]. Lin [72] reported a cell efficiency of 20.3% using a $CrO_x/Ag/CrO_x$ multilayer as HTL. In the same way, Wu [73] explored the use of a thermally evaporated $MoO_x/Ag/MoO_x$ multilayer as HTL on n-type c-Si substrates, obtaining a cell efficiency of 13.0% on a planar both sides-contacted structure.

Regarding the use of TMOs as HTL in IBC structures, Wu [52] compared the properties of MoO_x, WO_x and V_2O_x films as a selective contacts reporting efficiencies of 15.1%, 12.4% and 16.6%, respectively. In a later work [53], the same group reported a solar cell efficiency of 19.0%, using a $V_2O_x/Au/V_2O_x$ multilayer. However, the device includes a high thermal stage to form a phosphorous-doped front surface field, FSF = 200 Ω/sq. Um [51] and Lin [74] achieve an IBC cell efficiency of 15.4% and 15.8%, respectively, with MoO_x and CrO_x films as HTL. And Qiu [75] used a c-Si(p) absorber with a WO_x layer as a carrier-selective contact with cell efficiency of 10.9%.

Table 2.2 Single-junction c-Si solar cells with "novel"-based hole-selective contacts. Measured under the global AM1.5 spectrum (1 kW/m² at 25 °C).

Ref.	V_{oc} (mV)	J_{sc} (mAccm^{-2})	*FF* (%)	η (%)	Selective contacts	Description	Last member institution	Year
Electron-selective contact based on diffusion process (pnJ)								
[65]	616	37.0	72.0	15.4	MoO_x	c-Si(p), fully back contacted area	ANU	2015
[71]	685	39.8	77.8	20.4	MoO_x	c-Si(p), partially back contacted area	ANU	2015
[69]	378	35.8	67.7	9.1	NiO_x:Cu	Fully front area, sputtered NiO_x:Cu	Nankai	2018
[72]	638	39.8	80.1	20.3	CrO_x/Ag/CrO_x	c-Si(p), Partially back contacted area	SYSU	2018
Electron-selective contact based on doped a-Si:H film (SHJ)								
[58]	580	37.8	65.0	14.3	MoO_x	Fully front contacted area	Berkeley	2014
[59]	711	39.4	67.2	18.8	a-Si:H(i)/MoO_x	Fully front contacted area	Berkeley	2014
[62]	610	29.0	70.6	12.5	MoO_x	Planar fully front contacted area	UPC	2014
[63]	713	33.4	80.5	19.0	a-Si:H(i)/MoO_x	Planar fully front contacted area	F-ISE	2015
[65]	637	35.0	75.0	16.7	SiO_x/MoO_x	Planar fully front contacted area	ANU	2015
[61]	725	38.6	80.4	22.5	a-Si:H(i)/MoO_x	Cu electrodeposited (front-grid)	EPFL	2015
[22]	581	34.1	68.8	13.6	MoO_x	DopLa concept back junction cell	UPC	2015
[76]	593	36.0	67.6	14.4	a-Si:H(i)/MoO_x	Fully front contacted area	Nankai	2017
[63]	687	33.8	78.1	17.9	a-Si:H(i)/WO_x	Planar fully front contacted area	F-ISE	2015
[22]	577	33.3	65.0	12.5	WO_x	Fully front contacted area	UPC	2015
[68]	695	37.0	66.0	16.6	a-Si:H(i)/WO_x	Planar fully front contacted area	HZB	2017
[22]	606	34.4	75.3	15.7	V_2O_x	Fully front contacted area	UPC	2015
[64]	684	34.0	79.0	18.3	V_2O_x	Planar front fully contacted directly	F-ISE	2016
[67]	656	40.7	74.0	19.7	V_2O_x	IBC structure	UPC	2017

Ref.	V_{oc} (mV)	J_{sc} (mAcm^{-2})	*FF* (%)	η (%)	Selective contacts	Description	Last member institution	Year
Electron-selective contact based on Doped Free Asymmetric Selective Heterocontact (DASH)								
[51]	561	36.8	74.6	15.4	MoO_x	IBC structure	UNIST	2016
[17]	716	37.1	73.1	19.4	a-Si:H(i)/MoO_x	Fully front contacted area	Berkeley	2016
[66]	565	37.5	53.0	11.2	MoO_x	Fully front contacted area	ASU	2016
[52]	594	38.4	66.1	15.1	MoO_x	IBC structure	SYSU	2016
[73]	583	29.4	75.8	13.0	MoO_x/Ag/ MoO_x	Planar fully front contacted area	SYSU	2016
[70]	595	32.6	73.4	14.2	MoO_x	Planar fully front area, e-beam tech.	CAS	2017
[60]	706	38.4	76.2	20.7	a-Si:H(i)/MoO_x	Fully front contacted area	Berkeley	2018
[52]	610	38.8	70.0	16.6	$V2O_x$	IBC structure	SYSU	2016
[53]	651	38.7	75.5	19.0	V_2O_x/Au/V_2O_x	IBC structure, FSF	SYSU	2017
[54]	633	40.0	75.4	19.1	V_2O_x	IBC structure	UPC	2018
[52]	539	37.7	61.3	12.4	WO_x	IBC structure	SYSU	2016
[75]	525	33.7	61.7	10.9	WO_x	c-Si(p), fully back contacted area	SYSU	2018
[74]	605	39.2	66.6	15.8	CrO_x/Au/CrO_x	IBC structure	SYSU	2018

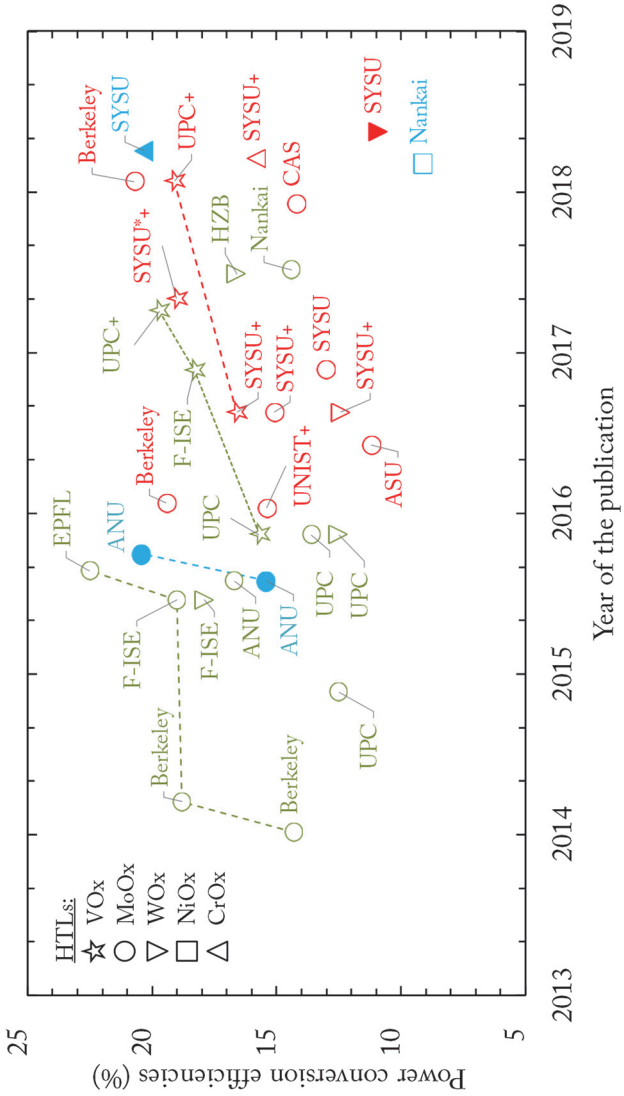

Figure 2.15 Power conversion efficiencies for c-Si solar cell using metal-based compounds as dopant-free hole-selective contacts (HTL). The blue, green and read symbols mean the use of a classical diffusion process (pnJ), a doped a-Si film (SHJ) and a dopant-free approach (DASH), respectively, for the electron-selective contacts. The (*) and (+) labelling mean the use of a front surface field (FSF) and an interdigitated back-contacted (IBC) structure, respectively. A filled symbol indicates that a p-type c-Si absorber is used.

2.5.3 Metal compounds as electron-selective contacts

In recent years, electron-selective contacts based on metal compounds (oxides or salts) have been used to manufacture c-Si solar cells. Table 2.3 summarises the main contributions reported in the literature and Figure 2.16 shows their efficiencies *vs.* the reported year.

Few studies have been conducted using TiO_x films as ETL. Yang [27] investigated the influence of TiO_x film thicknesses with the surface passivation, where effects on contact resistance were not reported. Applying the best result to a fully rear contacted c-Si(n) solar cell provided an efficiency of up to 19.8%. Nonetheless, the solar cell efficiency was mainly limited by the degradation of the TiO_x film during contact formation annealing. This phenomenon was investigated and overcome by introducing a very-thin thermally grown SiO_2 (~1.5 nm) layer between the c-Si and the TiO_x, obtaining a cell efficiency of 20.5% [77] and 21.6% [29]. Further passivation and contact resistivity research, with the same SiO_2/TiO_x bilayer, resulted in a solar cell with an efficiency of 22.1% [78]. However, the relatively large contact resistance (20 – 200 $m\Omega cm^2$) of the heterojunction discourages its use on a partial-area contacted structure.

Allen [79] explored the use of low work-function metals, such as calcium (Ca), to contact the TiO_x-based ETL to reduce the contact resistance, and applied it in a solar cell partially contacted on the rear side, achieving an efficiency of 21.8%.

Bullock [60] investigated the thermal stability of TiO_x films, achieving a solar cell efficiency of 20.9%. In which the contact properties of the previously reported LiF_x-based ETL [17] were improved by using a thin TiO_x film between the a-Si:H(i) and LiF_x layers. Boccard [66] previously reported the use of an a-Si:H(i) passivation layer together with a TiO_x layer obtaining an excellent surface passivation, with lifetimes close to 3 ms. Nevertheless, the manufactured solar cells showed S-shape current-voltage curves, and consequently a poor efficiency due to

an extremely low fill factor value. Finally, suppressing the a-Si:H(i) passivation film, they obtained an efficiency of 15.8%. Within the same studies, Boccard [66] and Bullock [60] developed the concept of DASH solar cells, reporting cell efficiencies of 11.2% and 20.7%, respectively.

In the same way, and as part of this Thesis, passivation interlayer of Al_2O_x deposited by ALD were also studied as an alternative to a-Si:H(i) and SiO_2 films. The combination of this layers with a layer of TiO_x deposited by ALD has allowed to obtain good ETL contacts, obtaining a DASH-IBC solar cell efficiency of up to 19.1% [54].

Other authors have published alternative TMOs to TiO_x as electron-selective contacts. Wan [26] investigated thermally evaporated MgO_x films with solar cell efficiencies of up to 20%, which represents ~5% more efficiency related to devices directly contacted with aluminium metal. Furthermore, the electron beam (e-beam) technique was also used to evaporate a MgO_x film, in which Yu [70] reported a DASH cell efficiency of 14.2%, with a planar device structure.

Wan [80] also studied the use of TaO_x films deposited by ALD as ETL, reporting a solar cell efficiency of 19.1% with Mg as a metal capping layer. However, the TaO_x/c-Si interface needs to be hydrogenated in order to improve the passivation, which was done by depositing a sacrificial layer of silicon nitride. In addition, they reported a relatively large contact resistance (~350 $m\Omega cm^2$) for a TaO_x film of only 6 nm of thicknesses, which is insufficient to be able to be applied on partial-area contacted devices.

Alternatively, metal carbonates (e.g. Cs_2CO_3) and metal salts (e.g. LiF_x) have been used as ETL for c-Si solar cells. Zhang [20] investigated the properties of a solution of Cs_2CO_3/polyethylenimine deposited by spin-coating on c-Si substrates. Optimum solution was applied to a DASH concept solar cell obtaining an efficiency of 13.7%. The enhanced performance, ~3% in efficiency, was

attributed to the reduced metal work-function of Al used over the Cs_2CO_3 layer. In addition, Wu also reported Cs_2CO_3-based ETL devices, but in this case the carbonate film was deposited by a thermal evaporation process, obtaining a DASH cell efficiency of 16.6% and 13.0% employing a V_2O_x film (IBC structure) [52] and MoO_x/Ag/MoO_x stacks (planar front junction cell) [73] as HTLs, respectively.

In the same way, metal salts allow the formation with metal a low work-function contact, which increases the electron selectivity [81]. Bullock [82] obtained a solar cell with an efficiency of 20.6% using a LiF_x film as an ETL with a partially contacted structure. Wan [19] reported a cell efficiency of 20.1% using a thermally evaporated MgF_x film, which was passivated with an a-Si:H(i) layer. The use of this passivated interlayer was also applied to a LiF_x-based contact, combined with an a-Si:H(i)/MoO_x stack as HTL, resulting in a DASH cell efficiency of 19.4% [17].

Other authors also used the LiF_x films as ETL on DASH-IBC structures, obtaining solar cell efficiencies of 15.4% [51], 19.0% [53] and 15.8% [74] using films of MoO_x, V_2O_x and CrO_x, respectively, as HTL.

Finally, low work-function metals have been investigated to form an Ohmic contact with n-type c-Si substrates. Wan [83] directly evaporated Mg metal (Φ ~3.7 eV) over an a-Si:H(i) passivation film obtaining solar cell efficiencies of up to 19.0%. Similarly, Allen [84] reported a remarkable efficiency of 20.3% with a partial-area back contacted cell with thermally evaporated Ca metal (Φ ~2.9 eV), in this case, without using any passivation interlayer.

Table 2.3 Single-junction c-Si solar cells with "novel"-based electron-selective contacts. Measured under the global AM1.5 spectrum (1 kW/m² at 25 °C).

Ref.	V_{oc} (mV)	J_{sc} (mAccm^{-2})	*FF* (%)	η (%)	Selective contacts	Description	Last member institution	Year
Hole-selective contact based on diffusion process (pnJ)								
[27]	639	39.2	79.1	19.8	TiO_x	Fully contacted area, ALD TiO_x	ANU	2015
[77]	650	39.5	80.0	20.5	SiO_2/TiO_x	Fully contacted area, ALD TiO_x	ANU	2016
[29]	676	39.6	80.7	21.6	SiO_2/TiO_x	Fully contacted area, ALD TiO_x	ANU	2016
[79]	681	39.6	80.9	21.8	TiO_x/Ca	Planar fully contacted area, ALD TiO_x	ANU	2017
[78]	674	39.8	82.5	22.1	SiO_2/TiO_x	Fully contacted area, ALD TiO_x	KAUST	2017
[26]	629	39.5	80.6	20.0	MgO_x	Fully contacted area	ANU	2016
[80]	638	37.8	79.3	19.1	TaO_x/Mg	Fully contacted area, ALD TaO_x	ANU	2017
[19]	687	37.8	77.3	20.1	a-Si:H(i)/MgF_x	Fully contacted area	ANU	2016
[82]	676	38.9	78.3	20.6	LiF_x	Partially contacted area	Berkeley	2016
[83]	637	38.0	78.4	19.0	a-Si:H(i)/Mg	Fully contacted area	ANU	2016
[84]	652	39.6	78.6	20.3	Ca/Al	Partially contacted area	ANU	2016
Hole-selective contact based on doped a-Si:H film (SHJ)								
[66]	616	37.2	69.0	15.8	TiO_x	Fully contacted area, ALD TiO_x	ASU	2016
[60]	713	37.5	78.1	20.9	aSi:H(i)/TiO_x/LiF_x	Fully contacted area (text.), ALD TiO_x	Berkeley	2018

Ref.	V_{oc} (mV)	J_{sc} (mAccm^{-2})	*FF* (%)	*PCE* (%)	Selective contacts	Description	Last member institution	Year
Hole-selective contact based on diffusion process (pnJ)								
[66]	565	37.5	53.0	11.2	TiO_x	Fully contacted area, ALD TiO_x	ASU	2016
[60]	706	38.4	76.2	20.7	a-Si:H(i)/TiO_x/LiF_x	Fully contacted area (text.), ALD TiO_x	Berkeley	2018
[54]	633	40.0	75.4	19.1	Al_2O_x/TiO_x	IBC structure, ALD Al_2O_x/TiO_x stack	UPC	2018
[70]	595	32.6	73.4	14.2	MgO_x	Fully contacted area, e-beam MgO_x	CAS	2018
[20]	621	32.2	68.4	13.7	Cs_2CO_3	Fully contacted area, spin-coat. Cs_2CO_3	SUDA	2014
[52]	610	38.8	70.0	16.6	Cs_2CO_3	IBC structure	SYSU	2016
[73]	583	29.4	75.8	13.0	Cs_2CO_3	Fully contacted area	SYSU	2017
[51]	561	36.8	74.6	15.4	LiF_x	IBC structure	UNIST	2016
[17]	716	37.1	73.2	19.4	a-Si:H(i)/LiF_x	Fully contacted are (text.)	Berkeley	2016
[53]	651	38.7	75.5	19.0	LiF_x	IBC structure	SYSU	2017
[74]	605	39.2	66.6	15.8	LiF_x	IBC structure	SYSU	2018

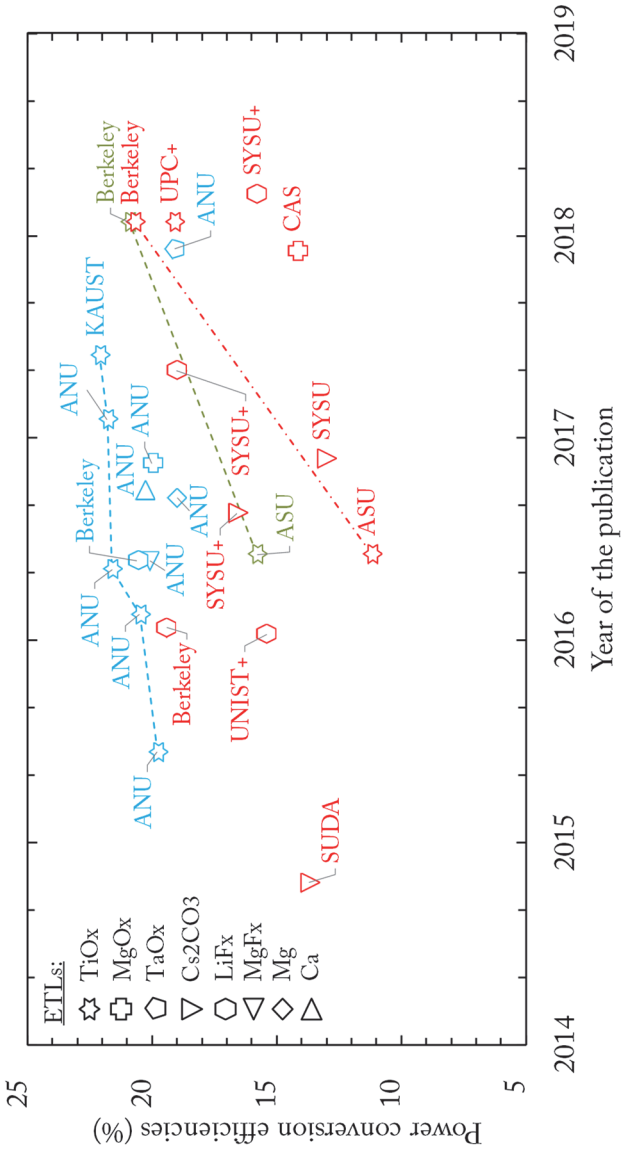

Figure 2.16 Power conversion efficiencies for c-Si solar cells using metal compounds as dopant-free electron-selective contacts (ETL). The blue, green and red symbols mean the use of a classical diffusion process (pnJ), a doped a-Si film (SHJ) and a dopant-free approach (DASH), respectively, for the hole-selective contact. The (+) labelling means the use of an interdigitated back-contacted (IBC) structure.

2.6 References

[1] A. Cuevas and D. Yan, "Misconceptions and Misnomers in Solar Cells," *IEEE J. Photovoltaics*, vol. 3, no. 2, pp. 916–923, Apr. 2013.

[2] P. Würfel and U. Würfel, *Physics of Solar Cells: From Principles to New Concepts*, Second, Up. Weinheim, Germany: Wiley-VCH Verlag GmbH & Co., 2009.

[3] M. A. Green, *Solar cells: operating principles, technology, and system applications*. Kensington, NSW: University of New South Wales, 1998.

[4] H. Savin *et al.*, "Black silicon solar cells with interdigitated back-contacts achieve 22.1% efficiency," *Nat. Nanotechnol.*, vol. 10, no. 7, pp. 624–628, Jul. 2015.

[5] G. López *et al.*, "Surface passivation and optical characterization of Al 2 O 3 /a-SiC x stacks on c-Si substrates," *Beilstein J. Nanotechnol*, vol. 4, pp. 726–731, 2013.

[6] W. Shockley and W. T. Read, "Statistics of the Recombinations of Holes and Electrons," *Phys. Rev.*, vol. 87, no. 5, pp. 835–842, Sep. 1952.

[7] S. Rein, T. Rehrl, W. Warta, and S. W. Glunz, "Lifetime spectroscopy for defect characterization: Systematic analysis of the possibilities and restrictions," *Cit. J. Appl. Phys.*, vol. 91, p. 2059, 2002.

[8] A. Richter, F. Werner, J. Schmidt, and S. W. Glunz, "Improved Parameterization of Auger Recombination in Silicon," *Energy Procedia*, vol. 27, pp. 88–94, Jan. 2012.

[9] A. Richter, M. Hermle, and S. W. Glunz, "Reassessment of the Limiting Efficiency for Crystalline Silicon Solar Cells," *IEEE J. Photovoltaics*, vol. 3, no. 4, pp. 1184–1191, Oct. 2013.

[10] R. Brendel and R. Peibst, "Contact Selectivity and Efficiency in Crystalline Silicon Photovoltaics," *IEEE J. Photovoltaics*, vol. 6, no. 6, pp. 1413–1420, Nov. 2016.

[11] J. Bullock, "Advanced Contacts For Crystalline Silicon Solar Cells," 2016.

[12] M. A. Green, "The path to 25% silicon solar cell efficiency: History of silicon cell evolution," *Prog. Photovoltaics Res. Appl.*, vol. 17, no. 3, pp. 183–189, May 2009.

[13] D. D. Smith, P. Cousins, S. Westerberg, R. De Jesus-Tabajonda, G. Aniero, and Y.-C. Shen, "Toward the Practical Limits of Silicon Solar Cells," *IEEE J.*

Photovoltaics, vol. 4, no. 6, pp. 1465–1469, Nov. 2014.

[14] K. Masuko *et al.*, "Achievement of More Than 25% Conversion Efficiency With Crystalline Silicon Heterojunction Solar Cell," *IEEE J. Photovoltaics*, vol. 4, no. 6, pp. 1433–1435, Nov. 2014.

[15] I. Martín García, J. M. López González, M. A. Colina Brito, A. Orpella García, and R. Alcubilla González, "DopLaCell: a new c-Si solar cell based on laser processing of dielectric films," *28th European Photovoltaic Solar Energy Conference and Exhibition*. WIP, pp. 1311–1316, 22-Nov-2013.

[16] P. Ortega *et al.*, "Fully low temperature interdigitated back-contacted c-Si(n) solar cells based on laser-doping from dielectric stacks," *Sol. Energy Mater. Sol. Cells*, vol. 169, pp. 107–112, Sep. 2017.

[17] J. Bullock *et al.*, "Efficient silicon solar cells with dopant-free asymmetric heterocontacts," *Nat. Energy*, vol. 1, no. 3, p. 15031, Jan. 2016.

[18] J. He, W. Zhang, J. Ye, and P. Gao, "16% efficient silicon/organic heterojunction solar cells using narrow band-gap conjugated polyelectrolytes based low resistance electron-selective contacts," *Nano Energy*, vol. 43, pp. 117–123, Jan. 2018.

[19] Y. Wan *et al.*, "Magnesium Fluoride Electron-Selective Contacts for Crystalline Silicon Solar Cells," *ACS Appl. Mater. Interfaces*, vol. 8, no. 23, pp. 14671–14677, Jun. 2016.

[20] Y. Zhang *et al.*, "High efficiency hybrid PEDOT:PSS/nanostructured silicon Schottky junction solar cells by doping-free rear contact," *Energy Environ. Sci.*, vol. 8, no. 1, pp. 297–302, Dec. 2015.

[21] C. Battaglia *et al.*, "Hole selective MoOx contact for silicon solar cells," *Nano Lett.*, vol. 14, no. 2, pp. 967–971, 2014.

[22] L. G. Gerling *et al.*, "Transition metal oxides as hole-selective contacts in silicon heterojunctions solar cells," *Sol. Energy Mater. Sol. Cells*, vol. 145, pp. 109–115, Feb. 2016.

[23] C. Battaglia, A. Cuevas, and S. De Wolf, "High-efficiency crystalline silicon solar cells: status and perspectives," *Energy Environ. Sci.*, vol. 9, no. 5, pp. 1552–1576, May 2016.

[24] M. T. Greiner, M. G. Helander, W.-M. Tang, Z.-B. Wang, J. Qiu, and Z.-H. Lu, "Universal energy-level alignment of molecules on metal oxides," *Nat. Mater.*, vol. 11, no. 1, pp. 76–81, Jan. 2012.

[25] H. Fujiwara and M. Kondo, "Effects of a-Si:H layer thicknesses on the performance of a-Si:H/c-Si heterojunction solar cells," *J. Appl. Phys.*, vol. 101, no. 5, p. 054516, Mar. 2007.

[26] Y. Wan *et al.*, "Conductive and Stable Magnesium Oxide Electron-Selective Contacts for Efficient Silicon Solar Cells," *Adv. Energy Mater.*, vol. 7, no. 5, p. 1601863, Mar. 2017.

[27] Xinbo Yang and K. Weber, "N-type silicon solar cells featuring an electron-selective TiO2 contact," in *2015 IEEE 42nd Photovoltaic Specialist Conference (PVSC)*, 2015, pp. 1–4.

[28] R. T. Tung, "The physics and chemistry of the Schottky barrier height," *Appl. Phys. Rev.*, vol. 1, no. 1, p. 011304, Mar. 2014.

[29] X. Yang, Q. Bi, H. Ali, K. Davis, W. V. Schoenfeld, and K. Weber, "High-Performance TiO2-Based Electron-Selective Contacts for Crystalline Silicon Solar Cells," *Adv. Mater.*, vol. 28, no. 28, pp. 5891–5897, Jul. 2016.

[30] L. G. Gerling, C. Voz, R. Alcubilla, and J. Puigdollers, "Origin of passivation in hole-selective transition metal oxides for crystalline silicon heterojunction solar cells," *J. Mater. Res.*, vol. 32, no. 2, pp. 260–268, 2017.

[31] M. T. Greiner and Z.-H. Lu, "Thin-film metal oxides in organic semiconductor devices: their electronic structures, work functions and interfaces," *NPG Asia Mater.*, vol. 5, no. 7, pp. e55–e55, Jul. 2013.

[32] M. D. Lammert and R. J. Schwartz, "The interdigitated back contact solar cell: A silicon solar cell for use in concentrated sunlight," *IEEE Trans. Electron Devices*, vol. 24, no. 4, pp. 337–342, Apr. 1977.

[33] Z. C. Holman *et al.*, "Current Losses at the Front of Silicon Heterojunction Solar Cells," *IEEE J. Photovoltaics*, vol. 2, no. 1, pp. 7–15, Jan. 2012.

[34] R. R. King, R. A. Sinton, and R. M. Swanson, "Front and back surface fields for point-contact solar cells," in *Conference Record of the Twentieth IEEE Photovoltaic Specialists Conference*, 1988, pp. 538–544 vol.1.

[35] D. D. Smith, G. Reich, M. Baldrias, M. Reich, N. Boitnott, and G. Bunea, "Silicon solar cells with total area efficiency above 25 %," in *2016 IEEE 43rd Photovoltaic Specialists Conference (PVSC)*, 2016, pp. 3351–3355.

[36] K. Yoshikawa *et al.*, "Silicon heterojunction solar cell with interdigitated back contacts for a photoconversion efficiency over 26%," *Nat. Energy*, vol. 2, no. 5, p. 17032, Mar. 2017.

[37] J. Libal *et al.*, "The Zebra Cell Concept - Large Area n-Type Interdigitated Back Contact Solar Cells and One-Cell Modules Fabricated Using Standard Industrial Processing Equipment," *27th Eur. Photovolt. Sol. Energy Conf. Exhib.*, pp. 567–570, Oct. 2012.

[38] V. D. Mihailetchi, H. Chu, G. Galbiati, C. Comparroto, A. Halm, and R. Kopecek, "A Comparison Study of n-type PERT and IBC Cell Concepts with Screen Printed Contacts," *Energy Procedia*, vol. 77, pp. 534–539, Aug. 2015.

[39] C. Reichel, F. Granek, M. Hermle, and S. W. Glunz, "Back-contacted back-junction *n* -type silicon solar cells featuring an insulating thin film for decoupling charge carrier collection and metallization geometry," *Prog. Photovoltaics Res. Appl.*, vol. 21, no. 5, p. n/a-n/a, Mar. 2012.

[40] E. Franklin *et al.*, "Design, fabrication and characterisation of a 24.4% efficient interdigitated back contact solar cell," *Prog. Photovoltaics Res. Appl.*, vol. 24, no. 4, pp. 411–427, Apr. 2016.

[41] R. Brendel *et al.*, "High-Efficiency RISE-IBC Solar Cells: Influence of Rear Side-Passivation on pn-Junction Meander Recombination," *28th Eur. Photovolt. Sol. Energy Conf. Exhib.*, pp. 971–975, Nov. 2013.

[42] B. Paviet-Salomon *et al.*, "Back-Contacted Silicon Heterojunction Solar Cells: Optical-Loss Analysis and Mitigation," *IEEE J. Photovoltaics*, vol. 5, no. 5, pp. 1293–1303, Sep. 2015.

[43] N. Mingirulli *et al.*, "Efficient interdigitated back-contacted silicon heterojunction solar cells," *Phys. status solidi - Rapid Res. Lett.*, vol. 5, no. 4, pp. 159–161, Apr. 2011.

[44] S. Harrison, O. Nos, G. D'Alonzo, C. Denis, A. Coll, and D. Munoz, "Back Contact Heterojunction Solar Cells Patterned by Laser Ablation," *Energy Procedia*,

vol. 92, pp. 730–737, Aug. 2016.

[45] M. Xu *et al.*, "Silicon heterojunction interdigitated back-contact solar cells bonded to glass with efficiency >21%," *Sol. Energy Mater. Sol. Cells*, vol. 165, pp. 82–87, Jun. 2017.

[46] J. Nakamura, N. Asano, T. Hieda, C. Okamoto, H. Katayama, and K. Nakamura, "Development of Heterojunction Back Contact Si Solar Cells," *IEEE J. Photovoltaics*, vol. 4, no. 6, pp. 1491–1495, Nov. 2014.

[47] G. Xu *et al.*, "6 inch IBC cells with efficiency of 23.5% fabricated with low-cost industrial technologies," in *2016 IEEE 43rd Photovoltaic Specialists Conference (PVSC)*, 2016, pp. 3356–3359.

[48] M. Dahlinger, B. Bazer-Bachi, T. C. Röder, J. R. Köhler, R. Zapf-Gottwick, and J. H. Werner, "22.0% Efficient Laser Doped back Contact Solar Cells," *Energy Procedia*, vol. 38, pp. 250–253, Jan. 2013.

[49] F. Haase *et al.*, "Laser contact openings for local poly-Si-metal contacts enabling 26.1%-efficient POLO-IBC solar cells," *Sol. Energy Mater. Sol. Cells*, vol. 186, pp. 184–193, Nov. 2018.

[50] C. Reichel, R. Müller, F. Feldmann, A. Richter, M. Hermle, and S. W. Glunz, "Interdigitated Back Contact Silicon Solar Cells Featuring Ion-Implanted Poly-Si/SiOx Passivating Contacts," in *33rd European Photovoltaic Solar Energy Conference and Exhibition*, 2017, pp. 455–459.

[51] H.-D. Um, N. Kim, K. Lee, I. Hwang, J. H. Seo, and K. Seo, "Dopant-Free All-Back-Contact Si Nanohole Solar Cells Using MoOx and LiF Films," *Nano Lett.*, vol. 16, no. 2, pp. 981–987, Feb. 2016.

[52] W. Wu *et al.*, "Dopant-free back contact silicon heterojunction solar cells employing transition metal oxide emitters," *Phys. status solidi - Rapid Res. Lett.*, vol. 10, no. 9, pp. 662–667, Sep. 2016.

[53] W. Wu *et al.*, "Dopant-free multilayer back contact silicon solar cells employing V2Ox/metal/V2Ox as an emitter," *RSC Adv.*, vol. 7, no. 38, pp. 23851–23858, Apr. 2017.

[54] G. Masmitjà *et al.*, "Interdigitated back-contacted crystalline silicon solar cells with low-temperature dopant-free selective contacts," *J. Mater. Chem. A*, vol. 6,

no. 9, pp. 3977–3985, 2018.

[55] W. Wu *et al.*, "22% efficient dopant-free interdigitated back contact silicon solar cells," in *AIP Conference Proceedings*, 2018, vol. 1999, no. 1, p. 040025.

[56] P. J. Cousins *et al.*, "Generation 3: Improved performance at lower cost," in *2010 35th IEEE Photovoltaic Specialists Conference*, 2010, pp. 000275–000278.

[57] X. Zhang *et al.*, "Development of High Efficiency Interdigitated Back Contact Silicon Solar Cells and Modules with Industrial Processing Technologies," in *The 6th World Conference on Photovoltaic Energy Conversion (WCPEC-6)*, 2014.

[58] C. Battaglia *et al.*, "Hole Selective MoO x Contact for Silicon Solar Cells," *Nano Lett.*, vol. 14, no. 2, pp. 967–971, 2014.

[59] C. Battaglia *et al.*, "Silicon heterojunction solar cell with passivated hole selective MoOx contact TL - 104," *Appl. Phys. Lett.*, vol. 104 VN-, no. 11, p. 113902, Mar. 2014.

[60] J. Bullock *et al.*, "Stable Dopant-Free Asymmetric Heterocontact Silicon Solar Cells with Efficiencies above 20%," *ACS Energy Lett.*, vol. 3, no. 3, pp. 508–513, Mar. 2018.

[61] J. Geissbühler *et al.*, "22.5% efficient silicon heterojunction solar cell with molybdenum oxide hole collector," *Appl. Phys. Lett.*, vol. 107, no. 8, p. 081601, Aug. 2015.

[62] L. G. Gerling-Sarabia, A. B. Morales-Vilches, M. Colina, C. Voz, J. Puigdollers, and R. Alcubilla, "Novel Crystalline Silicon Heterojunction Structure Based on Hole Selective MoO3 Emitter," in *29th European Photovoltaic Solar Energy Conference and Exhibition*, 2014.

[63] M. Bivour, J. Temmler, H. Steinkemper, and M. Hermle, "Molybdenum and tungsten oxide: High work function wide band gap contact materials for hole selective contacts of silicon solar cells," *Sol. Energy Mater. Sol. Cells*, vol. 142, pp. 34–41, Nov. 2015.

[64] M. Bivour, J. Temmler, F. Zahringer, S. Glunz, and M. Hermle, "High work function metal oxides for the hole contact of silicon solar Cells," in *2016 IEEE 43rd Photovoltaic Specialists Conference (PVSC)*, 2016, pp. 0215–0220.

[65] J. Bullock, D. Yan, A. Cuevas, Y. Wan, and C. Samundsett, "n- and p-typesilicon Solar Cells with Molybdenum Oxide Hole Contacts," *Energy Procedia*, vol. 77, pp. 446–450, Aug. 2015.

[66] M. Boccard, X. Yang, K. Weber, and Z. C. Holman, "Passivation and carrier selectivity of TiO2 contacts combined with different passivation layers and electrodes for silicon solar cells," in *2016 IEEE 43rd Photovoltaic Specialists Conference (PVSC)*, 2016, pp. 2403–2407.

[67] G. Masmitjà *et al.*, "V 2 O x -based hole-selective contacts for c-Si interdigitated back-contacted solar cells," *J. Mater. Chem. A*, vol. 5, no. 19, pp. 9182–9189, 2017.

[68] M. Mews, A. Lemaire, and L. Korte, "Sputtered Tungsten Oxide as Hole Contact for Silicon Heterojunction Solar Cells," *IEEE J. Photovoltaics*, vol. 7, no. 5, pp. 1209–1215, Sep. 2017.

[69] X. Yang, J. Guo, Y. Zhang, W. Liu, and Y. Sun, "Hole-selective NiO:Cu contact for NiO/Si heterojunction solar cells," *J. Alloys Compd.*, vol. 747, pp. 563–570, May 2018.

[70] J. Yu *et al.*, "Heterojunction solar cells with asymmetrically carrier-selective contact structure of molybdenum-oxide/silicon/magnesium-oxide," *Sol. Energy*, vol. 159, pp. 704–709, Jan. 2018.

[71] J. Bullock, C. Samundsett, A. Cuevas, D. Yan, Y. Wan, and T. Allen, "Proof-of-Concept p-Type Silicon Solar Cells With Molybdenum Oxide Local Rear Contacts," *IEEE J. Photovoltaics*, vol. 5, no. 6, pp. 1591–1594, Nov. 2015.

[72] W. Lin *et al.*, "Chromium Trioxide Hole-Selective Heterocontacts for Silicon Solar Cells," *ACS Appl. Mater. Interfaces*, vol. 10, no. 16, pp. 13645–13651, Apr. 2018.

[73] W. Wu *et al.*, "Multilayer MoOx/Ag/MoOx emitters in dopant-free silicon solar cells," *Mater. Lett.*, vol. 189, pp. 86–88, Feb. 2017.

[74] W. Lin *et al.*, "Novel hole selective CrOx contact for dopant-free back contact silicon solar cells," *Mater. Res. Bull.*, vol. 103, pp. 77–82, Jul. 2018.

[75] K. Qiu *et al.*, "Power-loss analysis of a dopant-free ZnS/p-Si heterojunction solar cell with WO3 as hole-selective contact," *Sol. Energy*, vol. 165, pp. 35–42, May 2018.

[76] F. Wang *et al.*, "Silicon solar cells with bifacial metal oxides carrier selective layers," *Nano Energy*, vol. 39, pp. 437–443, Sep. 2017.

[77] X. Yang, P. Zheng, Q. Bi, and K. Weber, "Silicon heterojunction solar cells with electron selective TiOx contact," *Sol. Energy Mater. Sol. Cells*, vol. 150, pp. 32–38, Jun. 2016.

[78] X. Yang, K. Weber, Z. Hameiri, and S. De Wolf, "Industrially feasible, dopant-free, carrier-selective contacts for high-efficiency silicon solar cells," 2017.

[79] T. G. Allen *et al.*, "A Low Resistance Calcium/Reduced Titania Passivated Contact for High Efficiency Crystalline Silicon Solar Cells," *Adv. Energy Mater.*, vol. 7, no. 12, p. 1602606, Jun. 2017.

[80] Y. Wan *et al.*, "Tantalum Oxide Electron-Selective Heterocontacts for Silicon Photovoltaics and Photoelectrochemical Water Reduction," *ACS Energy Lett.*, vol. 3, no. 1, pp. 125–131, Jan. 2018.

[81] F.-H. Hsu *et al.*, "Enhanced carrier collection in p-Ni1 – xO:Li/n-Si heterojunction solar cells using LiF/Al electrodes," *Thin Solid Films*, vol. 573, pp. 159–163, Dec. 2014.

[82] J. Bullock *et al.*, "Lithium Fluoride Based Electron Contacts for High Efficiency n-Type Crystalline Silicon Solar Cells," *Adv. Energy Mater.*, vol. 6, no. 14, p. 1600241, Jul. 2016.

[83] Y. Wan *et al.*, "A magnesium/amorphous silicon passivating contact for n -type crystalline silicon solar cells," *Appl. Phys. Lett.*, vol. 109, no. 11, p. 113901, Sep. 2016.

[84] T. G. Allen *et al.*, "Calcium contacts to n-type crystalline silicon solar cells," *Prog. Photovoltaics Res. Appl.*, vol. 25, no. 7, pp. 636–644, Jul. 2017.

3 Experimental and characterisation methods

This Chapter explains the baseline fabrication process involved in the different interdigitated back-contacted c-Si solar cells as well as the test structures used during the Thesis. Finally, the different techniques to measure and characterise such devices are explained in detail.

3.1 Fabrication processes

The interdigitated back-contacted (IBC) solar cells and the test samples were fabricated using high quality <100> single side polished float zone (FZ) n-type c-Si wafers with a thickness of 280 ±10 μm and a resistivity of 2 ±1 Ωcm.

3.1.1 Baseline fabrication process of IBC solar cells

The main steps involved for the two IBC solar cell approaches, which are "LD-TMO" and "Fully-TMO" devices, are shown in Figure 3.1. The main difference between them is how to obtain the electron transport layer (ETL). Depending on the ETL used, some fabrication stages are different but the others are the same.

The IBC structure "LD-TMO" uses the DopLa (Doped by laser) concept [1] to form the ETL, which consists on the laser-firing of an amorphous silicon film doped with phosphorous to form highly doped n^+ regions on the c-Si substrate. On the other hand, the IBC "Fully-TMO" solar cell uses a bilayer stack of aluminium and titanium oxides (Al_2O_x/TiO_x) deposited by atomic layer deposition (ALD) technique as an electron-selective contact. In both cases, the HTL regions are based on evaporated films of vanadium oxide (V_2O_x).

The manufacturing process, which is detailed in Figure 3.1, is organised in three parts: the first, the processing of the front side and the definition of the gap region between the electron- and hole-selective contact in the back. Next, the second part, in which the stages involved in the formation of the ETL are shown. Finally, the third part, in which the stages for the definition of the HTL are indicated.

Front and gap regions

The fabrication of IBC solar cells begins with the texturing of the front side with random pyramids using an alkaline etch bath. This bath consists of a solution of diluted tetramethylammonium hydroxide (TMAH) in deionized water (DI-H_2O) and isopropanol (IPA), 3200 ml of DI-H_2O/ 320 ml of IPA/ 360 ml of TMAH, at 85 ºC during 75 min. After a standard procedure of cleaning $RCA_{1/2}$ [2], the two sides of the wafer were covered with a 50 nm thick Al_2O_3 layer deposited by ALD technique (Savannah S200) at 200 ºC. The aluminium precursor and the oxidant specie used in the process were trimethylaluminium (TMA) and water, respectively. Then an annealing step was done at 400 ºC during 10 min in forming gas (hydrogen/nitrogen H_2/N_2) atmosphere, to activate the passivation of the surface provided by the Al_2O_3 films [3].

In order to avoid undesirable etching of the Al_2O_3 film during the subsequent chemical baths, a layer of silicon carbide (rich in carbon content) (a-SiC_x) of 35 nm of thickness was deposited, covering the alumina film on both sides of the wafer. The resultant Al_2O_3/a-SiC_x stack provides good anti-reflective coating (ARC) properties and maintains the surface passivation properties of the alumina film [4], in addition to protecting the alumina layer against chemical etchings. The a-SiC_x film was deposited by plasma-enhanced chemical vapour deposition (PECVD) process (13.56 MHz, Elettrorava S.p.A) at a temperature of 300 ºC, using silane (SiH_4) and methane (CH_4) as precursor gases.

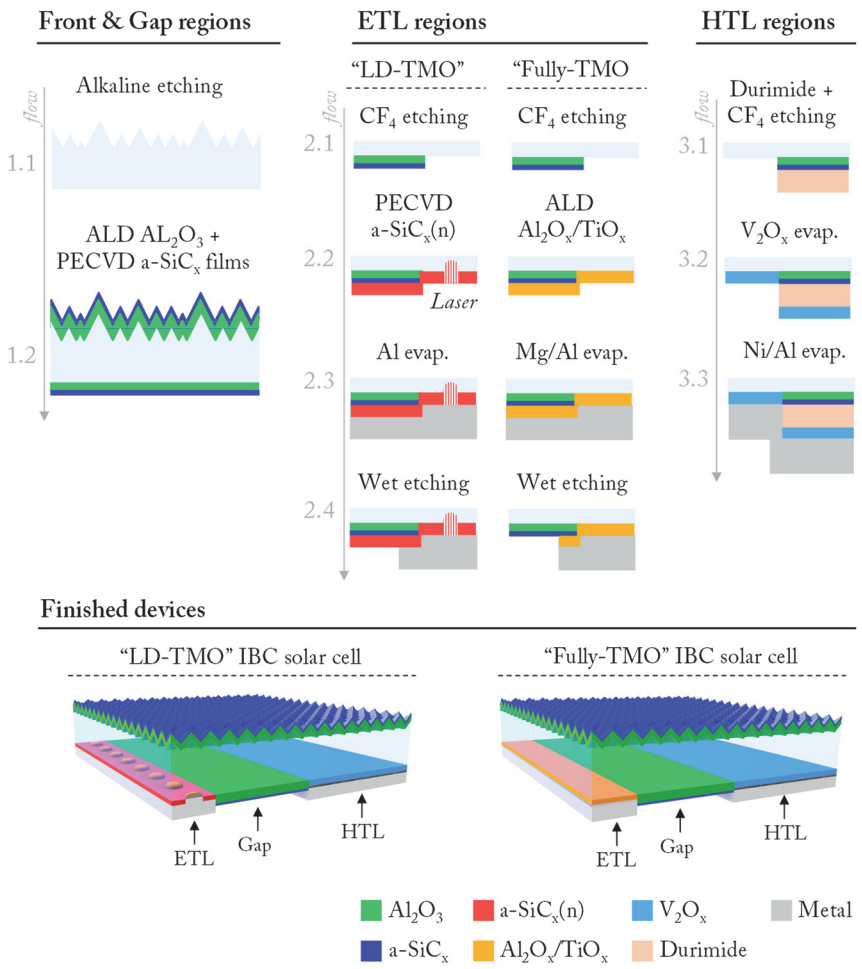

Figure 3.1 Process flow showing the main technological steps involved in the fabrication of the both "LD-TMO" and "Fully-TMO" IBC solar cell approaches.

"LD-TMO" approach to define ETL regions

A photoresist layer was deposited by spin-coated on the back of the wafer to define the strip-shaped ETL regions. Then, the a-SiC_x layer was locally removed by dry-etching using a plasma process with tetrafluoromethane (CF_4) gas (13.56 MHz,

Elettrorava S.p.A). After removing the photoresist layer, a diluted RCA_1-based cleaning [5] and a hydrofluoric acid (HF) diluted at 1% was performed, eliminating the Al_2O_3 film in the ETL areas. Then, the phosphorous-doped amorphous silicon carbide (a-SiC_x(n)) and a-SiC_x layers were deposited by PECVD with a thickness of 20 nm and 35 nm, respectively. This dielectric stack is used for two purposes, on the one hand as a passivation film and on the other hand as a source of phosphorous during the laser doping (LD) stage. The laser system to create the point-like ETL regions (n^+) operated at 1064 nm in the ns regime with a pulse repetition frequency of 4 kHz and a laser power of ~1 W [6]. The point-like contacts with a pitch of 200 µm were arranged at the centre of each strip-shaped ETL regions. At the end, just after an immersion in HF (1%) for 20 seconds a 4 µm thick aluminium layer was thermally evaporated. Afterwards, the interdigitated electrodes were patterned by a photolithography step using a standard Al wet-etching, i.e. 250 ml of orthophosphoric acid (H_3PO_4)/ 100 ml of IPA at a temperature of 70 °C for about 8 minutes.

"Fully-TMO" approach to define ETL regions

In this case, the photoresist layer was spin-coated on the back-side to define the ETL regions (again with strip shape) and the a-SiC_x layer was locally removed by dry etching using a CF_4 plasma process. After removing the remaining photoresist, a diluted RCA_1-based cleaning and an HF (1%) dip eliminated the Al_2O_3 film in the ETL areas. Then, the Al_2O_x/TiO_x stack consisting of 6 and 20 ALD cycles was deposited by ALD at a temperature of 100 °C. This stack was deposited without breaking the vacuum and with an estimated deposition rate of 1 Å/cycle for alumina and 0.6 Å/cycle for titania. The titanium and aluminium precursors used in the process were tetrakis(dimethylamido)titanium(IV) (TDMAT) and TMA respectively, while DI-H_2O was the oxidant specie. At the end, a 25 nm thick magnesium film plus a 4 µm thick aluminium layer were thermally

evaporated. The final technological step to define the ETL interdigitated contacts consisted of a standard photolithography plus a wet-etching of the aluminium layer.

HTL regions

Finally, to define the HTL contacts, the back surface was completely covered with a structural layer of photosensitive polyimide of 5 μm thickness (Durimide® 7505 type, Fujifilm). The HTL regions were patterned by a photolithography process. In this way, the finished ETL contact and the gap region, which is the separation region between the ETL and the HTL regions, were permanently protected against the CF_4 (dry) and HF (1%) (wet) etching processes, which were used to remove the silicon carbide stack and the Al_2O_3 layer of the HTL regions, respectively. Immediately afterwards, the device was placed in an oxygen-free Glovebox (O_2 <0.1 ppm), preventing any reaction of the sample with the air. The Glovebox is equipped with a vacuum deposition chamber and a thin-film deposition controller (SQC-310, Inficon), which allows deposition rates as low as 0.05 Å/s.

The HTL contact was thermally evaporated over the entire surface using a shadow mask, which simplified the fabrication process by avoiding an additional photolithography step. Firs, a 40 nm thick V_2O_x film was deposited by thermal evaporation of the V_2O_5 powder (Sigma Aldrich) at a deposition rate of 0.2 Å/s and a vacuum pressure of $9x10^{-6}$ mbar, followed with the deposition of a 25 nm thick nickel film (capping layer). The nickel layer was also deposited by thermal evaporation process and without breaking the vacuum. At the end, the HTL contact was finished with a highly conductive 1.5 μm thick aluminium layer.

It is important to indicate that the strategy of using two-metallisation scheme/level allows the possibility of using two different contact metals. Specifically, a low-

work function metal (Mg) to contact the ETL and another high-work function metal (Ni) to contact the HTL. In addition, the thick polyimide layer required to perform the two-level metallization scheme avoids any shunting between metal levels.

3.1.2 Baseline fabrication process of test structures

In parallel to the fabrication of solar cells, test structures were also fabricated using the same c-Si wafers described in the previous section. Three test sample devices were fabricated to characterise the passivation and electrical properties of the TMOs used in the IBC solar cells, which were the Ni-capped V_2O_x film and the Mg-capped Al_2O_x/TiO_x stack. The "Passivation Test" structure was used to optimise the quality of the passivation provided by these films. Alternatively, the "Diode Test" and the "Dot Test" structures were used to optimise the electrical conduction properties of the V_2O_x film and Al_2O_x/TiO_x stack, respectively.

The main steps involved in the fabrication process for the three test sample structures is depicted in Figure 3.2.

Passivation Test structures

The first step was the cleaning of the c-Si wafer using a $RCA_{1/2}$ cleaning procedure before the deposition on both sides of a 50 nm thick Al_2O_3 layer by ALD at 200 ^oC. TMA and water were used as the aluminium precursors and oxidant specie, respectively. The Al_2O_3 film was activated by an annealing at 400 ^oC under H_2/N_2 atmosphere for 10 min. Then, the alumina layer on one side was protected with a 35 nm thick a-SiC_x film, which was deposited by a PECVD process using precursor gases of SiH_4 and CH_4 at a chamber temperature of 300 ^oC.

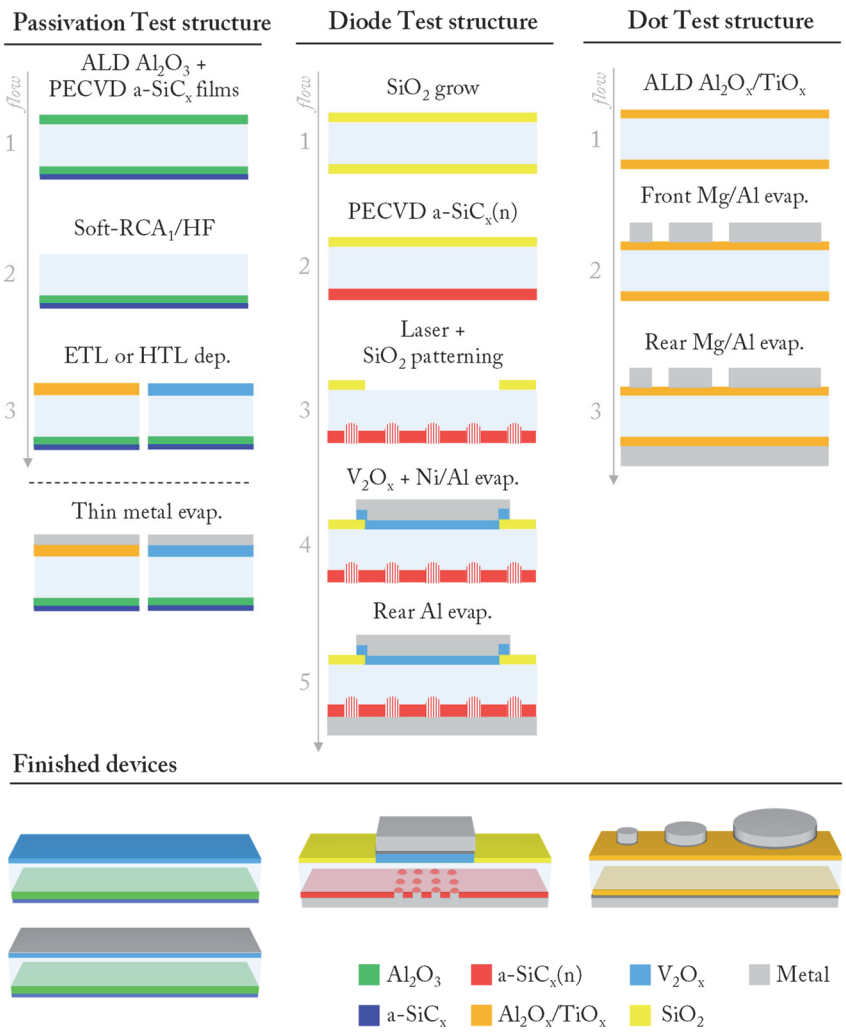

Figure 3.2 Process flow showing the main technological steps involved in the fabrication of the three test devices. They are labelled as "Passivation Test", "Diode Test" and "Dot Test" structures.

Finally, after a diluted RCA_1-based cleaning and an HF (1%) dip to clean the sample, as well as to etch the non-protected alumina film, the passivation film under study was deposited. The Al_2O_3/TiO_x stack or alternatively the V_2O_x film

were deposited using the same procedure described before for the IBC solar cells. Finally, a thin metal (<10 nm) over-layer was evaporated, respectively onto the TMO films to mimic a device contact. This semi-transparent metal allows sufficient light transmission to be able to measure the lifetime of the samples. The measurements were done before and after metal capping to discern the influence of it in the passivation properties.

Diode Test Structures

Firstly, a standard $RCA_{1/2}$ cleaning was performed for the samples, then a silicon oxide (SiO_2) of 60 nm of thicknesses was grown in a thermal oxidation step at 1000 ºC in quartz furnace tube. To prevent any contamination of the sample, before the oxidation and during the SiO_2 growing a chlorine-based gas (DCE, dichloroethylene) was introduced in the tube [7], [8]. After etching the SiO_2 film on the rear side, the sample was cleaned with a diluted RCA_1-based solution and an HF (1%) dip. Next, the a-SiC_x(n)/a-SiC_x stack with thicknesses of 20 nm and 35 nm, respectively, were deposited on the rear side of the sample by PECVD technique. After that, laser-doped regions (n^+) were created by irradiating with a laser beam the stack obtaining a square matrix arrangement of point-like contacts with a pitch of 600 μm. Laser conditions were the same as described for the IBC solar cell process.

Then, the SiO_2 film on the front side was patterned with a 4x4 mm^2 squares using a standard photolithography stage, followed by another diluted RCA_1-based solution and an HF (1%) dip cleaning steps. Finally, both the V_2O_x film and contact metals (Al or Ni/Al) were thermally evaporated on the front of the device by means of a 5x5 mm^2 square-patterned metallic shadow mask avoiding any extra photolithography step. At the end, a thick thermally evaporated Al film was deposited on the rear side.

Dot Test Structures

The first fabrication step in these samples was a standard $RCA_{1/2}$ cleaning with a subsequent diluted HF (1%) dip. Immediately after, the ALD Al_2O_x/TiO_x stack was deposited on both sides following the same process/steps described in the ETL regions of the IBC solar cells. Next, the Mg/Al metal stack was evaporated on the front side without breading vacuum by means of metallic shadow mask. In this way several dot-like contacts of different diameters (0.5, 1, 2, and 4 mm) were defined on the front surface. Then, the backside was fully covered with the same metal stack.

The metallic contact layers (Ni, Al and Mg) and V_2O_x used in the test samples, as well as in the IBC solar cells, were thermally evaporated from pure materials (>99.95%) using a vacuum chamber located inside a Glovebox device (O_2 <0.1 ppm) and with a vacuum pressure of less than $9x10^{-6}$ mbar.

3.2 Characterisation methods

Different methods were used to characterise the test samples and the IBC solar cells, which are described in detail in the following sections.

3.2.1 Lifetime measurements

The passivation of the surface provided by either, the ETL or the HTL or the dielectric passivation layer used on the front and back-gap surfaces, was evaluated by extracting both the surface recombination velocity (S) or, alternatively, the recombination current density (J_0), and the so-called implied open circuit voltage (iV_{oc}) parameter [9]. All these parameters were obtained by means of the measurement of the effective lifetime (τ_{eff}) [10] using the quasi-steady-state photoconductance decay technique (QSS-PC) [11] with the WCT-120

instrument (Sinton Consulting Inc.). As explained in Chapter 2, the total lifetime, which is the effective lifetime, can be written with the following expression:

$$\frac{1}{\tau_{eff}} = \frac{1}{\tau_{in}} + \frac{1}{\tau_{SRH}} + \frac{1}{\tau_s} \cong \frac{1}{\tau_{in}} + \frac{1}{\tau_s} \tag{3.1}$$

The simplification can be done since the Shockley-Read-Hall (SRH) recombination mechanisms for high quality FZ c-Si substrates is much smaller than other recombination mechanisms ($\tau_{SRH} \rightarrow \infty$). Therefore, the Auger and the radiative bulk recombination mechanisms are the predominant if the surfaces of the device are ideally passivated. In this case, the above bulk recombination mechanisms determine the maximum lifetime, which is the intrinsic bulk lifetime (τ_{in}). The intrinsic lifetime has been recently parameterized by Richter [12] with the following updated model on n-type c-Si substrates:

$$\frac{1}{\tau_{in}} \approx (N_{Bulk} + \Delta p) \cdot \begin{pmatrix} 2.5 \times 10^{-31} g_{eeh} N_{Bulk} + \\ 3 \times 10^{-29} \Delta p^{0.92} + 4.73 \times 10^{-15} B_{rel} \end{pmatrix} \tag{3.2}$$

where the N_{Bulk} and Δp parameters are the bulk doping concentration and excess concentration of minority-carrier holes, respectively. The g_{eeh} is an enhancement factor which depends on the bulk doping, e.g. 13.36 for $N_{bulk} \approx 3.5\text{x}10^{15}$ cm^{-3}, and the B_{rel} is a relative radiative recombination coefficient, according to Altermatt [13].

Additionally, the surface recombination and its related lifetime (τ_s) is commonly attributed to SRH mechanism, which can be expressed using an effective surface recombination velocity [14].

$$\frac{1}{\tau_s} = \frac{2S}{W} \tag{3.3}$$

where W is the thickness of the wafer and the factor 2 applied in Eq. (3.3) assumes symmetrical devices with same front and rear surface passivation, combining Eq. (3.1) and Eq. (3.3), the surface recombination velocity can be extracted as:

$$S(\Delta p) = \frac{W}{2}\left(\frac{1}{\tau_{eff}} - \frac{1}{\tau_{in}}\right) \tag{3.4}$$

Surface passivation can be achieved by means of reducing surface states, i.e. dangling bonds, in the so-called chemical passivation, and/or inducing an inversion/accumulation region near the surface, which reduces drastically minority carrier concentration on it, i.e. physical passivation [15]. The physical passivation can be obtained by either the presence of a fixed positive or negative charge density in the dielectric layer, e.g. SiO_2 or Al_2O_3 films, or due to a work function difference between semiconductor substrate and the cover film [16].

A good example in the literature is reported by Kerr [17], who characterised the passivation of stoichiometric silicon nitride (SiN) films, where passivation arises by a strong induced band-bending on the surface provided by the high fixed positive charge of these films. In his work, the injection level dependence of the S parameter was modelled in the same way as a "classical diffused emitter" [18], [19], using the J_0 as a representative parameter.

$$S(\Delta p) = \frac{J_0}{q\Delta p}\left(\frac{np}{n_i^2} - 1\right) \cong \frac{J_0(N_{Bulk}+\Delta p)}{qn_i^2} \tag{3.5}$$

where q is the elementary charge, and n, p, and n_i parameters are the electron, the hole and the intrinsic concentrations (n_i = 8.56x10^9 cm^{-3} at T = 25 ºC in c-Si), respectively. Combining the Eq. (3.5) in Eq. (3.1) and using Eq. (3.3) the well-known relationship between τ_{eff} and J_0 is given:

$$\frac{1}{\tau_{eff}} - \frac{1}{\tau_{in}} \cong \frac{2S}{W} \cong \frac{2J_0}{Wqn_i^2}(N_{Bulk} + \Delta p) \tag{3.6}$$

The main utility of Eq. (3.6) is that it allows to define the passivation quality of the surface by means of the parameter S or the J_0 indistinctly. Therefore, the lower J_0 or S value the better surface passivation. However, the J_0 parameter is generally more used to measure the contact selectivity, whereas, the S parameter is more used to quantify the level of passivation achieved using a specific dielectric layer.

Figure 3.3 shows, as an example, the lifetime measurement of a symmetrical sample passivated with a 50 nm thick ALD Al_2O_3 film annealed at 400 ºC during 10 min in FG. This layer is typically used as passivation film in the devices developed in this Thesis. From Eq. (3.1) the τ_s *vs.* Δp curve can be extracted and the S dependence with the excess carrier density using Eq. (3.3). Exceptional S values, as low as 0.5 cm/s at low injection levels are reached using the alumina-based passivation scheme optimised in this Thesis.

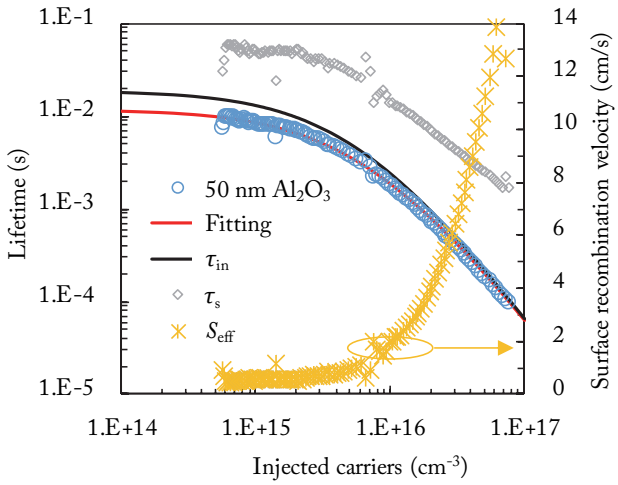

Figure 3.3 Effective lifetime vs. Δp of a c-Si(n) sample passivated symmetrically with a 50 nm thick ALD Al_2O_3 film (circle symbols) and their fitting curve (red line) using Eq. (3.6). The τ_{in} and the τ_s used in the fitting are also shown in the graph using black line and grey diamond symbols, respectively. Finally, the extracted S values are also shown (star-yellow symbols) with values as low as 0.5 cm/s at low injection level.

As can be seen in Figure 3.3, the effective lifetime behaviour exhibits a nearly constant value for low injection conditions. However, when the injection level increases, the τ_s decreases accordingly with the Eq. (3.6), and the Auger recombination becomes more dominant. Thus, the passivation of the Al_2O_3 layers could also be modelled, as Kerr [17] suggested. The high negative charge density of the Al_2O_3 films deposited by ALD [20] induces an inverted surface region on the silicon interface, exhibiting an equivalent diffused-like pn-Junction behaviour.

Finally, the J_0 parameter can be extracted from the slope of the curve $(1/\tau_{eff}-1/\tau_{in})$ *vs.* Δp, which is from the linear dependence suggested by Eq. (3.6), reaching a very low value of 1.6 fA/cm^2.

In addition, the outstanding surface passivation provided by the Al_2O_3 layers deposited by ALD indicates that it is feasible to use asymmetric test structures for the passivation studies. One side passivated with the alumina film, the contribution of which to the total recombination is almost null (~ideal passivation), and the other side passivated with the film under study, for example selective contacts based on V_2O_x or TiO_2 layers.

3.2.2 Electrical measurements

To evaluate the conductivity of the test structures based on both V_2O_x film and Al_2O_x/TiO_x stack, electrical measurements were done with a four-contact probe configuration, using a current-voltage tracer (Keithley 3601B) at room temperature.

On the one hand, the dark current density curves as a function of voltage (*J-V*) for the "Diode Test" structures (see Figure 3.2) provide information on the selectivity quality of the V_2O_x-based contact.

The following expression, for a single diode and excluding the series resistance (r_s), describes the *J-V* curves for a standard pn-Junction and it have been used to characterise the contact properties (see Figure 3.4).

$$J(V) = J_0\left(e^{(V-J(V)\cdot r_S)/n\cdot V_{th}} - 1\right) \cong J_0\left(e^{V/n\cdot V_{th}} - 1\right) \tag{3.7}$$

where n is the diode ideality factor, which in general varies with current level. However, the n value is equal to one in the low-middle voltage range for an ideal behaviour, whereas, n can take a value between 1 and 2 due to the recombination either the space charge region or in the perimeter of the device [21]. Therefore, the value of n can be used to evaluate the quality of the diode behaviour, i.e. n = 1.

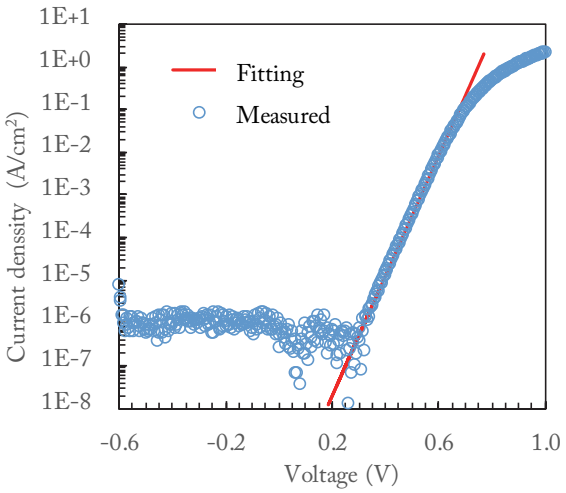

Figure 3.4 Measured dark current density vs. voltage of a Ni-capped 40 nm thick V_2O_x-based c-Si(n) diode test structure (circle symbols) and its fitting (red line) using Eq. (3.7) with a resultant ideality factor value of 1.2.

Figure 3.4 shows, by way of, the *J-V* curve of Ni-capped 40 nm thick V_2O_x diode and the equivalent fitting, in the middle-voltage range, using the Eq. (3.7), in which an *n* value around 1.2 is obtained. Additionally, the r_s and the expected open circuit voltage ($V_{oc,ex}$) values, respectively, can be estimated at forward voltages (~1 V) and at a current density of 40 mA/cm^2 by the relationship between the measured *J-V* curve and the ideal one (without ohmic losses).

On the other hand, the Al_2O_x/TiO_x-based selective contact on substrates of n-type c-Si acts as an ohmic contact. Thus, to determine the specific contact resistance (r_c), the "Dot Test" structures were used (see Figure 3.2 and 3.5). The r_c values were extracted by fitting the dependence of the total resistance (R_T) as a function of the diameter of the dot contact (d), using the spreading resistance model [22].

$$R_T = \frac{\rho}{d\pi}\tan^{-1}\left(\frac{4}{d/W}\right) + \frac{4r_c}{\pi d^2} + R_0 \tag{3.8}$$

where the parameters ρ and W are the resistivity and thickness of the substrate, respectively. A residual resistance (R_0) due to test measurements, for example, from the probe resistance, is also added. The R_0 value, which is independent of the contact diameter, can be found for the large dot diameter test sample, since the contribution of the contact resistance becomes negligible ($R_T \approx R_0$ for $d\uparrow\uparrow$).

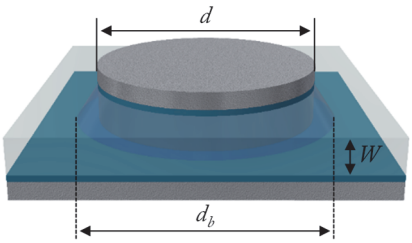

Figure 3.5 Geometric parameters of a single dot for the measurement of the total resistance (R_T) to obtain the specific contact resistance (r_c).

Eq. (3.8) is valid if the contribution of the backside contact resistance is negligible or if it is independent of the contact diameter. However, in the "Dot Test" structures, both sides have been fabricated with the same selective contact structure, so it is reasonable to think that both sides contribute to R_T. Therefore, a back-contact resistance (R_b) was added in Eq. (3.8) with the following expression:

$$R_b = \frac{4r_c}{\pi d_b^2} \tag{3.9}$$

The diameter of the back-contact dot (d_b) was estimated using a simple model (validated using 3D simulations), which considers an increase of the back-contact diameter in a factor whose value corresponds to the ratio between the spreading resistance and the cylindrical resistance. The cylindrical resistance is defined by the top dot diameter. Thus, the d_b parameter can be calculated as:

$$d_b = 2\sqrt{\frac{Wd}{\tan^{-1}\left(\frac{4}{d/W}\right)}} \tag{3.10}$$

Figure 3.6 shows, as an example, the measured resistance for Mg-capped Al_2O_x/TiO_x (with 3/20 ALD cycles) stack *vs.* reciprocal contact diameter. The fitting curve using Eq. (3.8) plus Eq. (3.9) is also shown. As a result, a r_c value as low as 2.5 mΩcm^2 has been achieved.

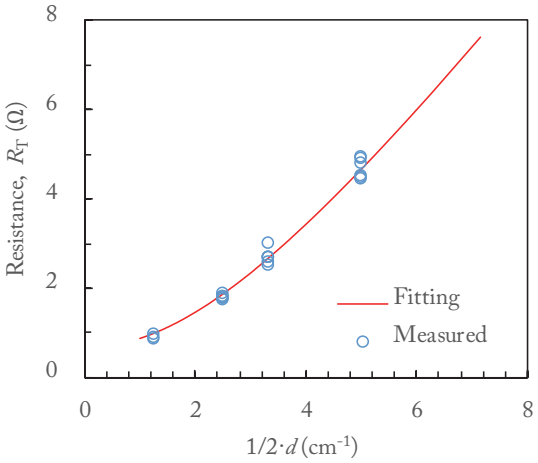

Figure 3.6 Contact resistance of Mg-capped Al_2O_x/TiO_x stack with 3/20 ALD cycles on c-Si(n) substrate vs. reciprocal contact diameter (circle symbols) and its fitting (red line) using Eq. (3.8) and Eq. (3.9).

3.2.3 Solar cell measurements

Spectral response of the solar cells by external quantum efficiency (*EQE*) curves were measured using commercial QEX10 instrument (PV Measurements, Inc.) with beam spot of 2x2 cm^2 centred within the active device area (3x3 cm^2).

The *EQE* measurements were done with a white bias light of 0.2 suns from an halogen lamp to overcome a possible non-linear response of the cell, as reported by Hartman [23] and Burdick [24] for thin-film and multijunction devices, respectively. In addition, to obtain a more accurate *EQE* measurement and accurate photocurrent (I_L) extraction, the solar cells were biased in reverse (-3 V) to discard any current drop due to ohmic losses in the cables and contacts of the measurement set-up.

The *EQE* measurement provides information on optical and recombination losses, and is defined as the ratio of the number of electrons that flow in the external circuit connected to the solar cell per each incident photon of a given wavelength (λ). Therefore, the I_L value can be determined, considering the 1 kW/m^2 AM1.5G solar spectrum, by convolving the *EQE* with the incident photon flux ($\Phi(\lambda)$) in the following manner (the wavelengths and integration limits are in nm units):

$$I_L = q \int_{300}^{1200} \Phi(\lambda) EQE(\lambda) d\lambda \tag{3.11}$$

Photovoltaic parameters were obtained from the illuminated current-voltage (*I-V*) characteristic using a four-contact probe configuration and a current-voltage tracer (Keithley 3601B). The devices were measured under standard AM1.5G spectrum (1 kW/m^2) at 25 ºC using an ORIEL 94021A solar simulator (Newport Corp.) The light irradiance was properly calibrated by means of a pyranometer.

3.2.4 Compositional and structural analysis

The compositional of the samples were studied by energy dispersive X-ray spectroscopy (EDX) and electron energy loss spectroscopy (EELS) analysis. In addition, details of the contact structure were mapped by high-angle annular dark field (HAADF) scanning transmission electron microscope (STEM) images.

The samples for these studies were acquired from cross-section lamellas prepared by the focused ion beam (FIB) lift-out technique using a Zeiss 1560XB system and the measurements were obtained using the equipment of two research laboratories. On the one hand, the Laboratorio de Microscopias Avanzadas, Instituto de Nanociencias de Aragón (LMA-INA) with a Cs-corrected FEI Titan (60-300 kV) transmission electron microscope system. Before the FEI Titan

analysis, the samples were subjected to an O_2 plasma cleaning. On the other hand, the Centres Científics i Tecnològics, Universitat de Barcelona (CCiT-UB), with a Gatan PEELS (GIF) system.

The composition of the samples was also analysed by an X-ray photoelectron spectroscopy (XPS) using a non-monochromatic Al-Kα source (1486.6 eV), (SPECS-Phoibos 150 detector). The XPS measurements were done at the Centre de Recerca en Ciència i Enginyeria Multiescala de Barcelona (CRCEMB).

3.3 References

[1] I. Martín García, J. M. López González, M. A. Colina Brito, A. Orpella García, and R. Alcubilla González, "DopLaCell: a new c-Si solar cell based on laser processing of dielectric films," *28th European Photovoltaic Solar Energy Conference and Exhibition*. WIP, pp. 1311–1316, 22-Nov-2013.

[2] W. Kern, "The Evolution of Silicon Wafer Cleaning Technology," *J. Electrochem. Soc.*, vol. 137, no. 6, p. 1887, Jun. 1990.

[3] J. J. H. Gielis, B. Hoex, M. C. M. Van De Sanden, and W. M. M. Kessels, "Negative charge and charging dynamics in films on Si characterized by second-harmonic generation," *J. Appl. Phys.*, vol. 104, p. 44903, 2008.

[4] G. López *et al.*, "Surface passivation and optical characterization of Al 2 O 3 /a-SiC x stacks on c-Si substrates," *Beilstein J. Nanotechnol*, vol. 4, pp. 726–731, 2013.

[5] G. Masmitja *et al.*, "Cost-effective cleaning solutions based on H2O/NH3/H2O2 mixtures for ALD Al2O3 passivated IBC c-Si solar cells," in *2017 Spanish Conference on Electron Devices (CDE)*, 2017, pp. 1–3.

[6] G. López *et al.*, "Emitter formation using laser doping technique on n- and p-type c-Si substrates," *Appl. Surf. Sci.*, vol. 336, pp. 182–187, 2015.

[7] P. H. Robinson and F. P. Heiman, "Use of HCl Gettering in Silicon Device Processing," *J. Electrochem. Soc.*, vol. 118, no. 1, p. 141, Jan. 1971.

[8] A. K. Hochberg *et al.*, "A New Liquid Chlorine Source for Silicon Oxidation," *J. Electrochem. Soc.*, vol. 139, no. 12, p. L117, Dec. 1992.

[9] R. A. Sinton, A. Cuevas, and M. Stuckings, "Quasi-steady-state photoconductance, a new method for solar cell material and device characterization," in *Conference Record of the Twenty Fifth IEEE Photovoltaic Specialists Conference - 1996*, 1996, pp. 457–460.

[10] A. Cuevas and D. Macdonald, "Measuring and interpreting the lifetime of silicon wafers," *Sol. Energy*, vol. 76, no. 1–3, pp. 255–262, Jan. 2004.

[11] R. A. Sinton and A. Cuevas, "Contactless determination of current–voltage characteristics and minority-carrier lifetimes in semiconductors from quasi-steady-state photoconductance data," *Appl. Phys. Lett.*, vol. 69, no. 17, pp. 2510–2512, Oct. 1996.

[12] A. Richter, F. Werner, J. Schmidt, and S. W. Glunz, "Improved Parameterization of Auger Recombination in Silicon," *Energy Procedia*, vol. 27, pp. 88–94, Jan. 2012.

[13] P. P. Altermatt, F. Geelhaar, T. Trupke, X. Dai, A. Neisser, and E. Daub, "Injection dependence of spontaneous radiative recombination in c-Si: experiment, theoretical analysis, and simulation," in *NUSOD '05. Proceedings of the 5th International Conference on Numerical Simulation of Optoelectronic Devices, 2005.*, pp. 47–48.

[14] A. B. Sproul, "Dimensionless solution of the equation describing the effect of surface recombination on carrier decay in semiconductors," *J. Appl. Phys.*, vol. 76, no. 5, pp. 2851–2854, Sep. 1994.

[15] A. G. Aberle, "Surface passivation of crystalline silicon solar cells: a review," *Prog. Photovoltaics Res. Appl.*, vol. 8, no. 5, pp. 473–487, Sep. 2000.

[16] A. G. Aberle, S. Glunz, and W. Warta, "Impact of illumination level and oxide parameters on Shockley-Read-Hall recombination at the Si-SiO2interface," *J. Appl. Phys.*, vol. 71, no. 9, pp. 4422–4431, May 1992.

[17] M. J. Kerr and A. Cuevas, "Comprehensive study of the doping and injection-level dependence of stoichiometric silicon nitride passivation for silicon solar cells," in *Conference Record of the Twenty-Ninth IEEE Photovoltaic Specialists Conference,*

2002., pp. 102–105.

[18] A. Cuevas, "The effect of emitter recombination on the effective lifetime of silicon wafers," *Sol. Energy Mater. Sol. Cells*, vol. 57, no. 3, pp. 277–290, Mar. 1999.

[19] P. Ortega, M. Vetter, S. Bermejo, and R. Alcubilla, "Very low recombination phosphorus emitters for high efficiency crystalline silicon solar cells," *Semicond. Sci. Technol.*, vol. 23, no. 12, p. 125032, Dec. 2008.

[20] B. Hoex, J. J. H. Gielis, M. C. M. van de Sanden, and W. M. M. Kessels, "On the c-Si surface passivation mechanism by the negative-charge-dielectric Al2O3," *J. Appl. Phys.*, vol. 104, no. 11, p. 113703, Dec. 2008.

[21] J. G. Fossum, R. D. Nasby, and Shing Chong Pao, "Physics underlying the performance of back-surface-field solar cells," *IEEE Trans. Electron Devices*, vol. 27, no. 4, pp. 785–791, Apr. 1980.

[22] R. H. Cox and H. Strack, "Ohmic contacts for GaAs devices," *Solid. State. Electron.*, vol. 10, no. 12, pp. 1213–1218, Dec. 1967.

[23] J. S. Hartman and M. A. Lind, "Spectral response measurements for solar cells," *Sol. Cells*, vol. 7, no. 1–2, pp. 147–157, Nov. 1982.

[24] J. Burdick and T. Glatfelter, "Spectral response and I–V measurements of tandem amorphous-silicon alloy solar cells," *Sol. Cells*, vol. 18, no. 3–4, pp. 301–314, Sep. 1986.

4 Vanadium oxide as hole-selective contact

This Chapter explores the use of vanadium oxide (V_2O_x) capped with a thin nickel layer as a hole transport layer (HTL). V_2O_x/Ni test samples demonstrate saturation current density and specific contact resistance values below 200 fA/cm^2 and 120 mΩcm^2, respectively. This HTL was applied to a c-Si solar cell with an interdigitated back-contacted cell structure reaching an efficiency of up to 19.7%.

4.1 Introduction

The interesting properties of TMOs to create selective contacts, as have been explained in Chapter 2, make them not only suitable for organic electronic devices [1], but also for c-Si based solar cells. Concretely, high work-function (>5 eV) TMOs such as molybdenum oxide (MoO_x), tungsten oxide (WO_x) and vanadium oxide (V_2O_x) can perform as efficient HTL films by promoting either an inversion layer on n-type crystalline silicon, c-Si(n), or an accumulation layer on p-type crystalline silicon, c-Si(p), [2], [3].

Table 4.1 lists the most interesting results using high work-function TMOs as HTL on c-Si solar cells. The preferred method for TMO-based film deposition is thermal evaporation, with MoO_x being the most reported material. Power conversion efficiencies (η) of 18.8% (ref. [4]), 19.4% (ref. [5]) and up to 22.5% (ref. [6]) have been achieved on c-Si(n) devices, while an efficiency of 20.4% was reported for c-Si(p) [7]. Additionally, V_2O_x and WO_x films are emerging alternatives yielding promising cell efficiencies of 18.3% and 17.9%, respectively, on n-type substrates [8]. These results were achieved using a both sides-contacted solar cell structure (*conventional* solar cells). Regarding IBC structures, several

groups have recently reported conversion efficiencies of 15.4% (MoO_x) [9], 16.6% (V_2O_x) [10] and 12.4% (WO_x) [10] for c-Si(n) substrates.

Within the reported examples, the best results are achieved using a very thin intrinsic hydrogenated amorphous silicon, a-Si:H(i), passivation interlayer, which increases the complexity of the final devices [11], [12], while only moderate open-circuit voltages (V_{oc} ~600 mV) have been reported to date with bare TMO/c-Si heterojunctions.

Table 4.1 Best solar cell efficiencies fabricated on crystalline silicon using transition metal oxides acting as hole transport layer (HTL). All the solar cells are fabricated on n-type c-Si except for ref. [7]*, which is based on p-type c-Si. The V_2O_x, MoO_x, WO_x, LiF_x, and Cs_2CO_3 films have been thermally evaporated.*

Ref.	HTL	ETL	V_{oc} (mV)	J_{sc} (mA/cm^2)	*FF* (%)	η (%)
Both sides-contacted structure						
[4]	a-Si:H(i)/MoO_x	a-Si:H(i)/a-Si:H(n)	711	39.4	67.2	18.8
[5]	a-Si:H(i)/MoO_x	a-Si:H(i)/LiF_x	716	37.1	73.1	19.4
[6]	a-Si:H(i)/MoO_x	a-Si:H(i)/a-Si:H(n)	725	38.6	80.4	22.5
[3]	V_2O_x	a-SiC_x(n) DopLa[a]	606	34.4	75.3	15.7
[3]	MoO_x	a-SiC_x(n) DopLa[a]	581	34.1	68.6	13.6
[3]	WO_x	a-SiC_x(n) DopLa[a]	577	33.3	65.0	12.5
[8]	a-Si:H(i)/MoO_x	a-Si:H(i)/a-Si:H(n)	710	33.4	80.0	19.0
[8]	a-Si:H(i)/WO_x	a-Si:H(i)/a-Si:H(n)	685	33.8	78.0	17.9
[8]	V_2O_x	a-Si:H(i)/a-Si:H(n)	684	34.0	79.0	18.3
[7]	MoO_x	*p* diffusion	658	39.8	77.8	20.4
Interdigitated back-contacted structure						
[9]	MoO_x	LiF_x	561	36.8	74.6	15.4
[10]	V_2O_x	Cs_2CO_3	610	38.8	70.0	16.6
[10]	MoO_x	Cs_2CO_3	594	38.4	66.1	15.1
[10]	WO_x	Cs_2CO_3	539	37.7	61.3	12.4
[13][b]	**V_2O_x**	**a-SiC_x(n) DopLa[a]**	**656**	**40.7**	**74.0**	**19.7**

[a] DopLa: doped by laser. [b] this work.

In the next section, the results and discussions of thermally evaporated V_2O_x films on surface passivation and carrier selectivity are reported, as well as the impact of the metal capping layer on the electrical contact performance. In this way, it is demonstrated that the c-Si/V_2O_x/Ni heterojunction provide a high level of carrier selectivity, i.e. low contact resistance and surface passivation, on c-Si(n) substrates. Moreover, the long-term stability and temperature stability of the initial electrical properties are also analysed. Finally, this selective contact scheme is applied to an IBC c-Si(n) solar cell architecture, achieving an efficiency of 19.7% on a 9 cm^2 device, which is the state-of-the-art as can be seen in Table 4.1. It is also remarkable that a highly stable open circuit voltage of 656 mV could be achieved in the final devices without an additional passivation layer, i.e. a-Si:H(i).

4.2 V_2O_x-based selective contact properties

Surface passivation can be characterised in terms of interface recombination velocity (S) or alternatively by means of recombination current density (J_0). The former parameter is more suitable for passivation dielectric layers, whereas the latter is applied to selective contacts such as homo and heterojunctions. Independent of the type of surface, recombination can be evaluated by the so-called implied open circuit voltage parameter (iV_{oc}) [14]. The higher the iV_{oc} value, the lower the recombination inside the device considering both bulk and surface recombination. All foregoing parameters can be obtained by effective lifetime (τ_{eff}) measurements using the quasi-steady-state photoconductance (QSS-PC) technique.

The recombination current density of V_2O_x films ($J_{0,HTL}$) was measured for different layer thicknesses from 15, 30 to 60 nm using asymmetrical samples (see the inset of Figure 4.1). In these samples, the front and rear sides were covered,

respectively, with a V_2O_x layer and a dielectric passivation stack. In order to discriminate the recombination contribution of the hole-selective contact in lifetime measurements, a well-passivated rear surface is necessary, i.e. a low rear surface recombination velocity (S_R). Layers like aluminium oxide (Al_2O_3) deposited by atomic layer deposition (ALD) technique [15], [16] or amorphous silicon carbide films (a-SiC_x(n)) [17] deposited by plasma-enhanced chemical vapour deposition (PECVD) process satisfies this passivation requirement.

The alumina film used through the experiments has a surface recombination velocity as low as ~0.5 cm/s, which corresponds to τ_{eff} values >15 ms (at Δp = 10^{15} cm^{-3}), Consequently, the $J_{0,HTL}$ parameter can be calculated as follows (see Chapter 3 for more details):

$$\frac{1}{\tau_{eff}} - \frac{1}{\tau_{in}} = \frac{S_R}{W} + \frac{J_{0,HTL}}{Wqn_i^2}(N_{Bulk} + \Delta p) \cong \frac{J_{0,HTL}}{Wqn_i^2}(N_{Bulk} + \Delta p) \quad (4.1)$$

where W is the thickness of the wafer (280 μm), q is the elementary charge, n_i is the silicon intrinsic carrier concentration (n_i = 8.56x10^9 cm^{-3} at 25 ºC), Δp is the carrier excess density, τ_{in} is the intrinsic bulk lifetime (Auger and radiative mechanisms) [18] and N_{Bulk} parameter is the bulk doping concentration.

From Eq. (4.1), the $J_{0,HTL}$ values can be directly extracted for different V_2O_x thicknesses considering the slopes of $1/\tau_{eff} - 1/\tau_{in}$ *vs.* Δp curves, which is shown in Figure 4.1. Similar results were obtained independently of V_2O_x thickness yielding $J_{0,HTL}$ and iV_{oc} values of 175 ±10 fA/cm^2 and 675 ±5 mV respectively, in accordance with the state-of-the-art related to this material [8].

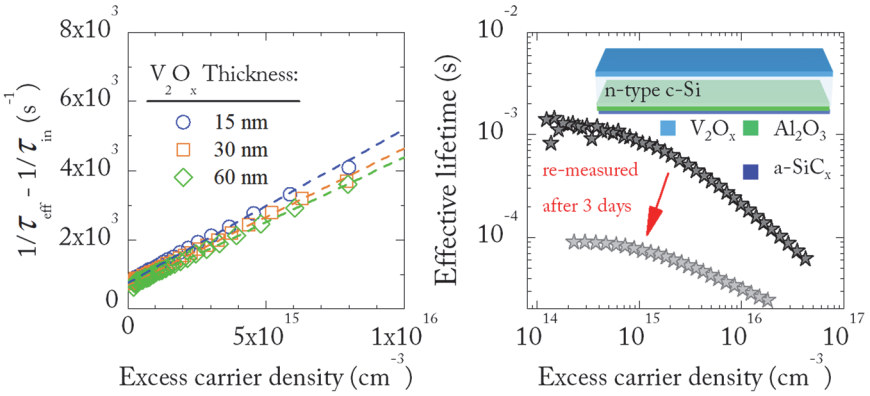

Figure 4.1 Measured intrinsic-corrected inverse effective lifetime (symbols) and their fitting (dashed line) as a function of the injection level for different V_2O_x thicknesses (left). Measured τ_{eff} of the 40 nm thick V_2O_x layer after its deposition and after three days under air exposure (right). A sketch of passivated samples used in the study is shown in the inset.

In spite of the initial good $J_{0,HTL}$ and iV_{oc} results, surface passivation degrades with time as can be deduced from the strong drop in τ_{eff} shown in Figure 4.1. This might be due to a reduction of the material work-function by chemical reaction of the samples with air (water and oxygen species) [19], [20], weakening the induced p-type inversion region beneath the contacts and increasing local recombination, i.e. lower τ_{eff} values.

In order to mimic a final contacted solar cell, the use of a nickel metal layer was explorer, which has a metal work-function (Φ_M) of ~5.4 eV, as the capping material in a similar way to that reported in ref. [2] where palladium (Φ_M ~5.6 eV) was used over MoO_x films. For the purpose of allowing reliable QSS-PC measurements, the Ni thickness was kept under 10 nm (in this case ~5 nm thick). This is mandatory to guarantee that the metal conductivity does not saturate the lifetime measurement system and sufficient light is transmitted into the silicon substrate. The results are shown in Figure 4.2.

Firstly, the normalised iV_{oc} to the initial value (iV_{oc}^{n}) as a function of time was explored after deposition of thin nickel layer over 40 nm thick V_2O_x films. Samples with the metal capping exhibit much better long-term surface passivation stability, indicating that the Ni layer is thick enough to block the reaction of chemical species in air with the V_2O_x films.

In addition, Figure 4.2 also shows the evolution of the iV_{oc}^{n} parameter for accumulative 10 min annealing in forming gas at different temperatures. The Ni/V_2O_x films seem to be stable at temperatures, from a surface passivation point of view, up to 300 ºC without apparent degradation. These results demonstrate a great passivation stability and enough thermal budget for the last stages of solar cell fabrication.

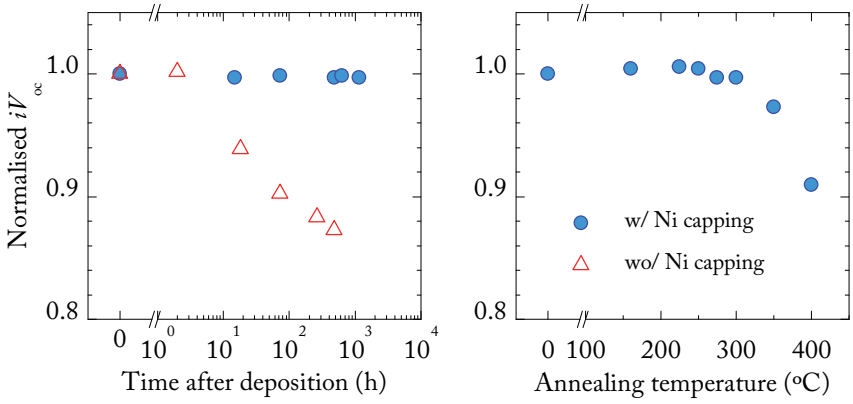

Figure 4.2 Comparative behaviour (time-dependence of iV_{oc} under air exposure) of samples with and without nickel capping film (left). Effect of the accumulative annealing temperature on the iV_{oc} parameter (right). Notice that the iV_{oc} values are normalised to their initial values.

To evaluate the electron-blocking or hole-extraction properties, as well as the contact resistance of the V_2O_x layers on c-Si(n) substrates, vertical test diodes were used (the test device sketch is depicted in the inset of Figure 4.3). The measured dark current density *vs.* voltage (*J-V*) curves greatly depend on the metal capping material, nickel or alternatively aluminium, being the former material the best choice to contact the devices. We suppose that the high Φ_M value of the Ni plays a significant role in preserving the high work-function provided by the V_2O_x films, which increases the hole-selective contact behaviour.

On the other hand, the influence of V_2O_x thickness on the electrical device performance was studied. As it can be seen in Figure 4.4, the diode ideality factor $n = J/(V_{th} \cdot \Delta J/\Delta V)$, which it has been calculated in the middle voltage range and considering a thermal voltage (V_{th}) of 25.69 mV at 25 ºC, improves towards the ideal value, i.e. $n = 1$, as film thickness increases, exhibiting a minimum value of ~1.2 for the 40 nm thick V_2O_x sample.

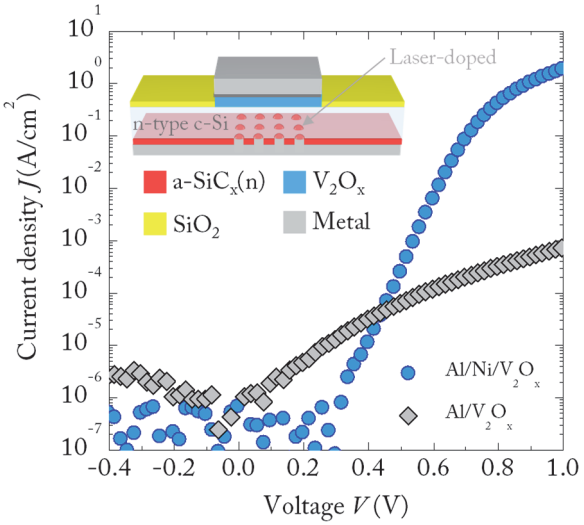

Figure 4.3 Measured dark J-V characteristics for 40 nm thick V_2O_x on c-Si(n) diode test devices using nickel or aluminium as a capping material. The Diode Test structure is depicted in the inset.

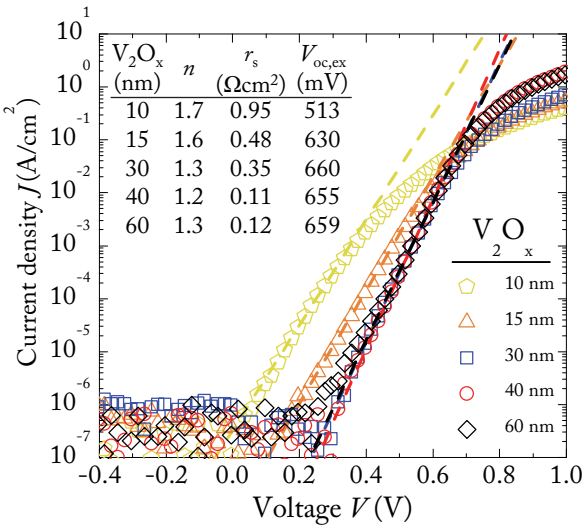

Figure 4.4 Measured dark J-V characteristics for different V_2O_x thicknesses (symbols) and their fitting (dashed line) on n-type c-Si Diode Test devices (left). The inside table shows the extracted parameters.

Additionally, the specific series resistance (r_s) decreases to 115 mΩcm^2 as the V_2O_x film thickness increases, producing similar results for 40 and 60 nm. Notice that r_s is estimated at forward voltage ~1 V by fitting the real *J-V* characteristics and the ideal one without series resistance. If the contribution of the rear contacts to the total series resistance is neglected, r_s values are representative of the specific contact resistance between silicon and the Ni/V_2O_x stack as a worst case.

Moreover, the expected open circuit voltage ($V_{oc,ex}$), extracted from ideal *J-V* curves without series resistance at a current density of 40 mA/cm^2, seems to be limited to 655 ±5 mV for relatively thick layers (>30 nm). These values are 20 mV lower than iV_{oc} values obtained from lifetime measurements. This drop might be due to recombination at the rear laser-doped contacts.

Finally, an accumulative temperature annealing was done for a representative 40 nm thick V_2O_x film to find the temperature limits of annealing steps after diode test metallization. Figure 4.5 shows a rapid degradation with temperatures higher than 150 ºC, affecting the current transport at high injection voltage levels, i.e. increasing contact resistance.

In order to determine the origin of the good selective contact behaviour, i.e. passivation and carrier collection, a physical characterization of the V_2O_x/c-Si heterojunction was carried out. Firstly, an X-ray photoelectron spectroscopy (XPS) scan was performed on a 10 nm thick V_2O_x film deposited on a c-Si(n) substrate. Figure 4.6 shows the spectra of the vanadium (V 2p) and the oxygen (O 1s) core levels, with both V^{5+} and V^{4+} oxidation states present at their characteristic binding energies [3], [21], confirming that the V_2O_x film is oxygen deficient and semi-conductive in nature.

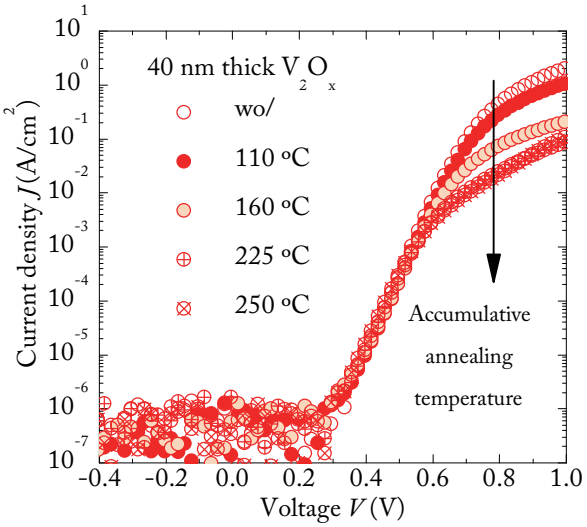

Figure 4.5. Effect of an accumulative annealing temperature process on the J-V characteristic for a representative Diode Test device of 40 nm thick V_2O_x film contacted with Ni/Al. The annealing were performed using forming gas atmosphere during 10 minutes.

The XPS spectra of the silicon (Si 2p) core level reveals the presence of Si^{3+} oxidation states [22] related to silicon suboxide SiO_x with an oxygen content x~1.5. This would explain why this interfacial layer, amorphous in nature and rich in defect states, is able to conduct even for thicknesses greater than the tunnelling limit (<2 nm) of fully stoichiometric SiO_2 layers [23], [24]. A similar conduction process is assumed for oxygen deficient metal oxides [1], [25], using defect states located within the bandgap as conduction paths for carriers.

Additionally, figure 4.7 shows the valence band spectra measured by XPS in the vicinity of the Fermi level (0 eV), with a characteristic peak at ~2 eV (after subtraction of the H-terminated c-Si component), which is ascribed to the characteristic defect states reported in the literature [25]. Consequently, the conduction across the V_2O_x layer can be guaranteed.

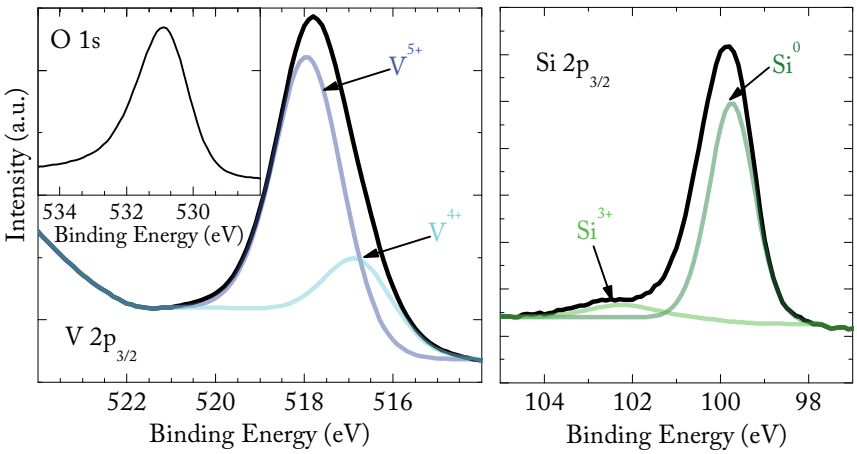

Figure 4.6 XPS spectra of the V 2p core level, showing V^{5+} and V^{4+} oxidation states (left), the O 1s core level (inset) and the Si 2p core level, showing Si^0 and Si^{3+} oxidation states (right).

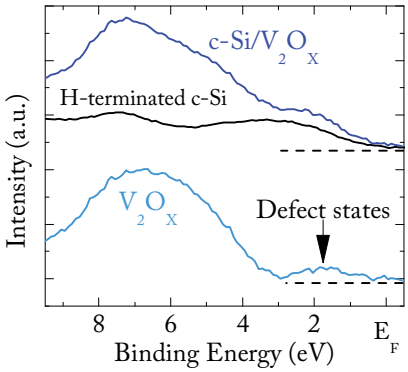

Figure 4.7 Valence band spectra measured by XPS in the vicinity of the Fermi level (0 eV) where defect states are observed at ~2 eV.

To complement the foregoing characterisation, the SiO_x interlayer is confirmed by cross-sectional images of the V_2O_x/c-Si interface via high resolution transmission electron microscopy (HR-TEM), observing the presence of a ~3.5 nm thick amorphous SiO_x interlayer between the c-Si and the V_2O_x film, see Figure 4.8. The formation of such layers has been previously reported for dielectric oxides deposited on c-Si and it has been attributed to the spontaneous growth of a SiO_x interlayer by chemical reaction [26], [27]. We presume that this SiO_x interlayer passivates the c-Si surface dangling-bonds, giving rise to the passivation properties of V_2O_x/c-Si heterojunctions.

The HR-TEM images also show the presence of a ~5 nm thick Ni film, which is confirmed by electron energy loss spectroscopy (EELS), which enables obtaining compositional information from the Al/Ni/V_2O_x selective contact stack, see Figure 4.9. Thus, the presence of the thin Ni capping layer in between aluminium and V_2O_x film is confirmed.

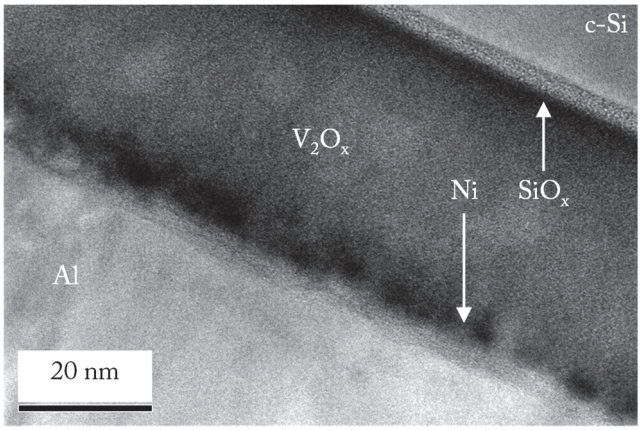

Figure 4.8 HR-TEM image showing a SiO_x interlayer grown on c-Si by a chemical reaction with the V_2O_x, and a Ni capping layer between the aluminium and V_2O_x films.

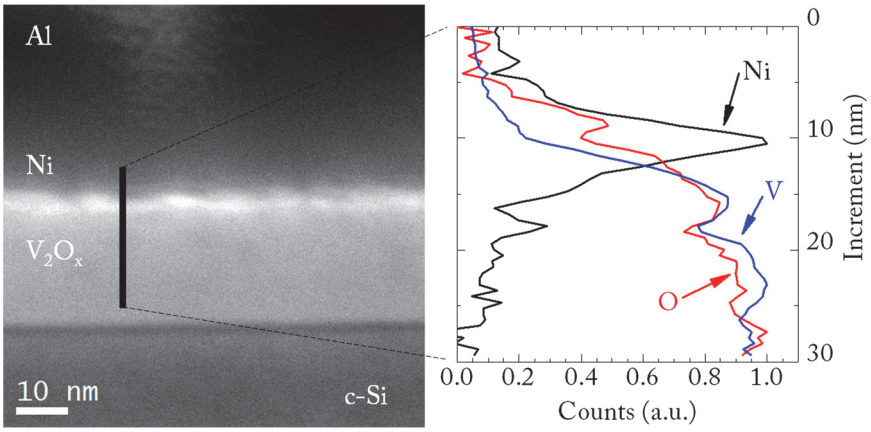

Figure 4.9 High resolution transmission electron microscopy (HR-TEM) image and an electron energy loss spectroscopy (EELS) line scan across the Al/Ni/V_2O_x selective contact stack confirms the thin uniform nickel capping layer.

4.3 IBC solar cells based on V_2O_x films

To demonstrate the applicability of Ni/V_2O_x stack as a hole contact in IBC solar cells, proof-of-concept solar cells (3x3 cm^2 area) were fabricated, with different HTL coverage values (f_{HTL}), defined as the ration between all HTL regions and the whole device area. A range of f_{HTL} from 40, 52 to 64% was studied in order to know the influence of cell geometry on series resistance and rear surface passivation and its impact on photovoltaic efficiency. Figure 4.10 depicts the schematic structure of the cell, see Chapter 3 for more details about the steps involved in the fabrication process.

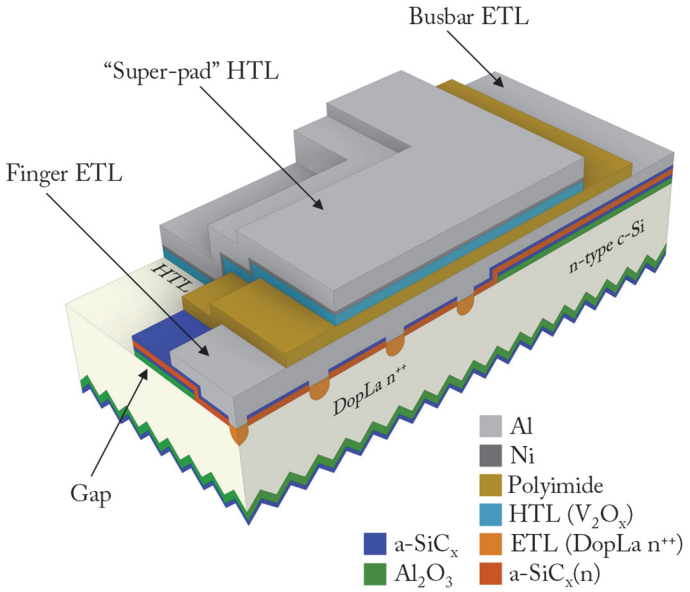

Figure 4.10 A 3D bottom view sketch of the V_2O_x-based IBC solar cell showing the main layers involved in the structure.

The fabricated IBC cells, (see image in the inset of Figure 4.11), combine evaporated V_2O_x films as HTL and DopLa [28] ETL regions. Both HTL and ETL strip-like electrodes are defined following an interdigitated pattern isolated from each other with passivated gap regions. Additionally, the metal electrodes contacting each transport layer are different and are optimised for each selective contact thanks to a two-level metallisation strategy developed in our devices.

Notice that ALD Al_2O_3 films are used on the gap region between HTL and ETL contacts, as well as over random pyramids on the front side, achieving excellent surface passivation. In addition, a very low reflectance and light absorption is achieved on the front surface [16]. It is worth noting that these devices do not use a-Si:H(i) layers and are free of transparent conductive oxide (TCO) films, which are normally made with scarce materials like indium oxide. Another important advantage is that they avoid high temperature processes, i.e. thermal diffusions and/or thermal oxidations, which results in a very low thermal budget process.

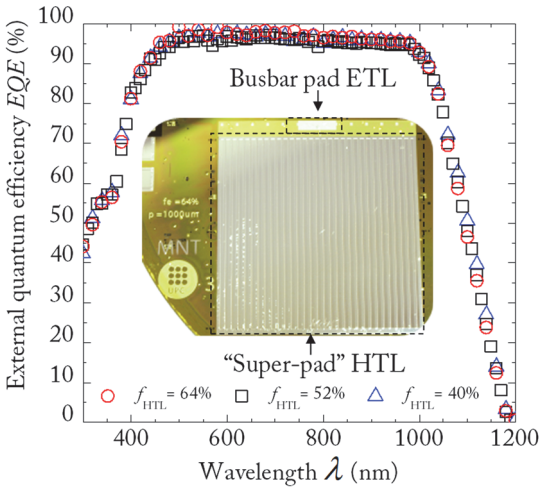

Figure 4.11 EQE curves for IBC solar cells with different HTL area coverage values f_{HTL}. In the inset, an image of the cell showing the pad through the polyamide layer needed to access the ETL's busbar and the top "super-pad" of the HTL electrode.

The external quantum efficiency (*EQE*) curves corresponding to the 40, 52 and 64% HTL coverage cells are shown in Figure 4.11. *EQE* values of up to 98% in the visible wavelength range confirm the outstanding front surface passivation obtained. The slight influence of f_{HTL} on the *EQE* curves also indicates that rear surface passivation provided by both the ETL contacts and the Al_2O_3 layer in the gap between collector regions is enough to avoid significant electrical shadowing [29].

Illuminated current density-voltage (*J-V*) curves were measured under standard AM1.5G spectrum (1 kW/m^2 and T = 25 ºC). Figure 4.12 shows the *J-V* curve of the best IBC cell efficiency. Finally, the photovoltaic parameters of the solar cells are listed in Table 4.2.

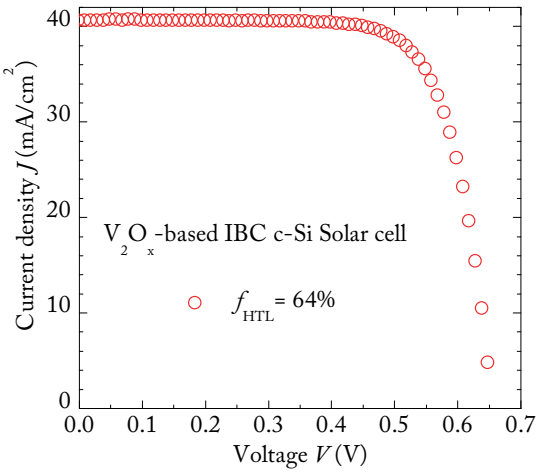

Figure 4.12 Illuminated current density-voltage (J-V) curve for the best IBC solar cell based on V_2O_x films as hole-selective contact on n-type c-Si substrates.

Table 4.2 Summary of the IBC solar cell parameters measured under standard test conditions (AM1.5G 1 kW/m² solar spectrum, 25 °C) for the three device topologies with 9 cm² active area.

Cell topology (%), f_{HTL}/f_{ETL}	V_{oc} (mV)	J_{sc} (mA/cm²)	*FF* (%)	η (%)
40 / 2.4	639	40.8	71.3	18.5
52 / 1.9	656	40.4	74.0	19.5
64 / 1.4	656	40.7	74.0	19.7

Conversion efficiencies of up to 19.7% were achieved with a short-circuit current density (J_{sc}), an open-circuit voltage (V_{oc}) and a fill factor (*FF*) of 40.7 mA/cm², 656 mV and 74.0%, respectively. These results demonstrate that n-type c-Si solar cells with an IBC structure and using a Ni/V_2O_x stack as the hole-selective contact can reach high efficiencies in a simple low-temperature fabrication process, which is without the use of a-Si:H(i) films, TCOs or thermal oxidation/diffusions steps.

4.4 References

[1] M. T. Greiner, M. G. Helander, W.-M. Tang, Z.-B. Wang, J. Qiu, and Z.-H. Lu, "Universal energy-level alignment of molecules on metal oxides," *Nat. Mater.*, vol. 11, no. 1, pp. 76–81, Jan. 2012.

[2] J. Bullock, A. Cuevas, T. Allen, and C. Battaglia, "Molybdenum oxide MoO_x: A versatile hole contact for silicon solar cells," *Appl. Phys. Lett.*, vol. 105, no. 23, p. 232109, Dec. 2014.

[3] L. G. Gerling *et al.*, "Transition metal oxides as hole-selective contacts in silicon heterojunctions solar cells," *Sol. Energy Mater. Sol. Cells*, vol. 145, pp. 109–115, Feb. 2016.

[4] C. Battaglia *et al.*, "Silicon heterojunction solar cell with passivated hole selective MoOx contact TL - 104," *Appl. Phys. Lett.*, vol. 104 VN-, no. 11, p. 113902, Mar. 2014.

[5] J. Bullock *et al.*, "Efficient silicon solar cells with dopant-free asymmetric heterocontacts," *Nat. Energy*, vol. 1, no. 3, p. 15031, Jan. 2016.

[6] J. Geissbühler *et al.*, "22.5% efficient silicon heterojunction solar cell with molybdenum oxide hole collector," *Appl. Phys. Lett.*, vol. 107, no. 8, p. 081601, Aug. 2015.

[7] J. Bullock, C. Samundsett, A. Cuevas, D. Yan, Y. Wan, and T. Allen, "Proof-of-Concept p-Type Silicon Solar Cells With Molybdenum Oxide Local Rear Contacts," *IEEE J. Photovoltaics*, vol. 5, no. 6, pp. 1591–1594, Nov. 2015.

[8] M. Bivour, J. Temmler, F. Zahringer, S. Glunz, and M. Hermle, "High work function metal oxides for the hole contact of silicon solar Cells," in *2016 IEEE 43rd Photovoltaic Specialists Conference (PVSC)*, 2016, pp. 0215–0220.

[9] H.-D. Um, N. Kim, K. Lee, I. Hwang, J. H. Seo, and K. Seo, "Dopant-Free All-Back-Contact Si Nanohole Solar Cells Using MoOx and LiF Films," *Nano Lett.*, vol. 16, no. 2, pp. 981–987, Feb. 2016.

[10] W. Wu *et al.*, "Dopant-free back contact silicon heterojunction solar cells employing transition metal oxide emitters," *Phys. status solidi - Rapid Res. Lett.*, vol. 10, no. 9, pp. 662–667, Sep. 2016.

[11] Z. C. Holman *et al.*, "Current Losses at the Front of Silicon Heterojunction Solar Cells," *IEEE J. Photovoltaics*, vol. 2, no. 1, pp. 7–15, Jan. 2012.

[12] B. Demaurex, S. De Wolf, A. Descoeudres, Z. Charles Holman, and C. Ballif, "Damage at hydrogenated amorphous/crystalline silicon interfaces by indium tin oxide overlayer sputtering," *Appl. Phys. Lett.*, vol. 101, no. 17, p. 171604, Oct. 2012.

[13] G. Masmitjà *et al.*, "V 2 O x -based hole-selective contacts for c-Si interdigitated back-contacted solar cells," *J. Mater. Chem. A*, vol. 5, no. 19, pp. 9182–9189, 2017.

[14] R. A. Sinton, A. Cuevas, and M. Stuckings, "Quasi-steady-state photoconductance, a new method for solar cell material and device characterization," in *Conference Record of the Twenty Fifth IEEE Photovoltaic Specialists Conference - 1996*, 1996, pp. 457–460.

[15] B. Hoex, J. Schmidt, P. Pohl, M. C. M. van de Sanden, and W. M. M. Kessels, "Silicon surface passivation by atomic layer deposited Al2O3," *J. Appl. Phys.*, vol.

104, no. 4, p. 044903, Aug. 2008.

[16] G. López *et al.*, "Surface passivation and optical characterization of Al 2 O 3 /a-SiC x stacks on c-Si substrates," *Beilstein J. Nanotechnol*, vol. 4, pp. 726–731, 2013.

[17] I. Martín *et al.*, "c-Si Solar Cells based on Laser-processed Dielectric Films," *Energy Procedia*, vol. 55, pp. 255–264, Jan. 2014.

[18] A. Richter, S. W. Glunz, F. Werner, J. Schmidt, and A. Cuevas, "Improved quantitative description of Auger recombination in crystalline silicon," *Phys. Rev. B*, vol. 86, no. 16, p. 165202, Oct. 2012.

[19] M. C. Gwinner *et al.*, "Doping of Organic Semiconductors Using Molybdenum Trioxide: a Quantitative Time-Dependent Electrical and Spectroscopic Study," *Adv. Funct. Mater.*, vol. 21, no. 8, pp. 1432–1441, Apr. 2011.

[20] J. Meyer, K. Zilberberg, T. Riedl, and A. Kahn, "Electronic structure of Vanadium pentoxide: An efficient hole injector for organic electronic materials," *J. Appl. Phys.*, vol. 110, no. 3, p. 033710, Aug. 2011.

[21] K. Zilberberg *et al.*, "Inverted Organic Solar Cells with Sol-Gel Processed High Work-Function Vanadium Oxide Hole-Extraction Layers," *Adv. Funct. Mater.*, vol. 21, no. 24, pp. 4776–4783, Dec. 2011.

[22] F. J. Himpsel, F. R. McFeely, A. Taleb-Ibrahimi, J. A. Yarmoff, and G. Hollinger, "Microscopic structure of the SiO 2 /Si interface," *Phys. Rev. B*, vol. 38, no. 9, pp. 6084–6096, Sep. 1988.

[23] J. Shewchun, R. Singh, and M. A. Green, "Theory of metal-insulator-semiconductor solar cells," *J. Appl. Phys.*, vol. 48, no. 2, pp. 765–770, Feb. 1977.

[24] M. A. Green, "Effects of pinholes, oxide traps, and surface states on MIS solar cells," *Appl. Phys. Lett.*, vol. 33, no. 2, pp. 178–180, Jul. 1978.

[25] M. T. Greiner and Z.-H. Lu, "Thin-film metal oxides in organic semiconductor devices: their electronic structures, work functions and interfaces," *NPG Asia Mater.*, vol. 5, no. 7, pp. e55–e55, Jul. 2013.

[26] L. G. Gerling, C. Voz, R. Alcubilla, and J. Puigdollers, "Origin of passivation in hole-selective transition metal oxides for crystalline silicon heterojunction solar cells," *J. Mater. Res.*, vol. 32, no. 2, pp. 260–268, 2017.

[27] G. D. Wilk, R. M. Wallace, and J. M. Anthony, "High-κ gate dielectrics: Current status and materials properties considerations," *J. Appl. Phys.*, vol. 89, no. 10, pp. 5243–5275, May 2001.

[28] I. Martín García, J. M. López González, M. A. Colina Brito, A. Orpella García, and R. Alcubilla González, "DopLaCell: a new c-Si solar cell based on laser processing of dielectric films," *28th European Photovoltaic Solar Energy Conference and Exhibition*. WIP, pp. 1311–1316, 22-Nov-2013.

[29] C. Reichel, F. Granek, M. Hermle, and S. W. Glunz, "Back-contacted back-junction *n* -type silicon solar cells featuring an insulating thin film for decoupling charge carrier collection and metallization geometry," *Prog. Photovoltaics Res. Appl.*, vol. 21, no. 5, p. n/a-n/a, Mar. 2012.

5 Titanium oxide as electron-selective contact

This Chapter explores the use of titanium oxide together with an ultrathin alumina (Al_2O_x/TiO_x) stack capped with a thin magnesium film as an electron transport layer (ETL). Al_2O_x/TiO_x/Mg test samples demonstrate saturation current density and specific contact resistance values below 140 fA/cm^2 and 2.5 mΩcm^2, respectively. This ETL stack was applied to an interdigitated back-contacted (IBC) structure reaching a fully-TMO based IBC c-Si solar cell with an efficiency beyond 19%.

5.1 Introduction

TMOs with low work-function values (<4 eV) such as magnesium oxide (MgO_x) [1] and titanium oxide (TiO_x) [2] are good candidates to obtain electron-selective contacts on c-Si substrates as is explained in Chapter 2.

With respect to TiO_x-based contacts, the Titania films were firstly applied in c-Si photovoltaics as an antireflection coating [7], being an alternative to silicon-nitride or silicon oxide films. Recently, TiO_x films have begun to be used as ETL directly in contact with c-Si solar cells. However, a poor contact passivation showing effective surface recombination velocities (S_{eff}) of around 300 cm/s has limited the obtained power conversion efficiency to ~11% [8]. Another approach uses a very thin-film layer of thermally grown SiO_2 between the TiO_x and silicon [5]. However, the high value of the contact resistance (<20 mΩcm^2) prevents the use of this approach in interdigitated back-contacted (IBC) structures, where the electron contact area is only a fraction of the total rear surface.

The replacement of this passivation interlayer, e.g. thermal SiO_2 or intrinsic hydrogenated amorphous silicon (a-Si:H(i)), by other films, which could be conformably deposited at low temperature with good thickness control, is an important research topic, as it would drastically simplify the fabrication process and reduce its cost.

In this part of the Thesis, we focus on the electron-selective contacts made of TiO_x films deposited by atomic layer deposited (ALD) technique. These TiO_x films were combined with an ultrathin aluminium oxide (Al_2O_x) interlayer also deposited by ALD. This Al_2O_x interlayer between the TiO_x and the silicon surface aims to reduce the defect density at the interface. The results and discussions of ALD Al_2O_x/TiO_x stack related to surface passivation and carrier selectivity are reported as a function of the Al_2O_x and TiO_x thicknesses. In Addition, the influence of different metal capping materials such as nickel (Ni), aluminium (Al) and magnesium (Mg) has been studied to optimise the selectivity. The best contact configuration consisting of a Mg-coated Al_2O_x/TiO_x stack is applied as an electron-selective contact on IBC c-Si solar cells, together with a previously explored Ni-coated V_2O_x as hole-selective contact (see the previous Chapter) with conversion efficiencies of up to 19.1% in 9 cm^2 devices. It is important to note that both selective contacts are fabricated at temperatures lower than 100 ^oC reducing the overall thermal budget of the fabrication process, as well as circumventing the use of toxic and flammable gasses as dopant precursors.

5.2 TiO_x-based selective contact properties

Surface contact passivation has been evaluated by extracting both the effective surface recombination velocity and the implicit open-circuit voltage (iV_{oc}) from effective lifetime (τ_{eff}) measurements using the quasi-steady-state

photoconductance decay (QSS-PC) technique [12]. Passivation test samples were fabricated on n-type c-Si substrates, the structure of which is depicted in the inset of Figure 5.1. One side was almost ideally passivated by means of a 50 nm thick Al_2O_3 film deposited by ALD [13]. The alumina film used in all experiments has a surface recombination velocity as low as ~0.5 cm/s, which corresponds to τ_{eff} values >15 ms (at Δp = 10^{15} cm^{-3}), as is shown in Chapter 3, which allows us to neglect the corresponding recombination contribution of this surface in the effective lifetime measurements. The other side was covered with the Al_2O_x/TiO_x stack, using different film thicknesses.

Figure 5.1 shows the τ_{eff} values as a function of the number of TiO_x ALD cycles, which are directly related with the film thickness. Firstly, considering 3 ALD cycles of alumina, the τ_{eff} value increases, i.e. better passivation properties, as the number of ALD cycles of TiO_x increases, achieving a τ_{eff} values of up to 660 µs with 20 ALD cycles.

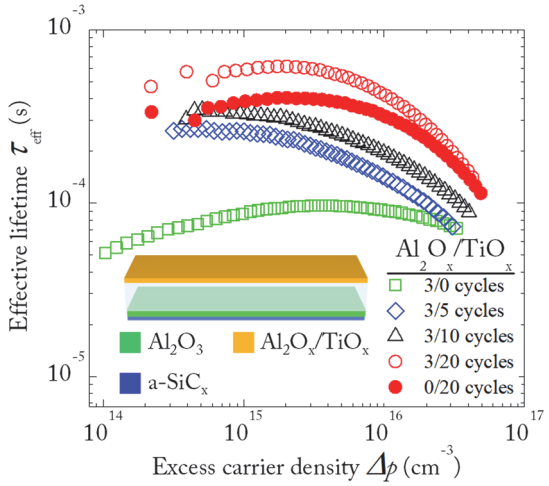

Figure 5.1 Measured effective lifetimes vs. excess carrier density of the passivation test samples on n-type c-Si substrates, considering different Al_2O_x and TiO_x ALD cycles. A sketch of the test structure is depicted in the inset.

However, if we continue increasing the thickness of the TiO_x film (>20 ALD cycles) leads a poorer surface passivation quality, as can be seen in Figure 5.2. In this Figure, the iV_{oc} values are shown as a function of the number of Al_2O_x and TiO_x ALD cycles. The higher the value of iV_{oc}, the higher the passivation quality of the surface. This trend has also been reported by X. Yang *et al.* [14]. Therefore, from the point of view of passivation, the best option is to use 3/20 ALD cycles of Al_2O_x/TiO_x, which results in an iV_{oc} value of 683 mV.

Secondly, by setting the number of TiO_x ALD cycles to 20, the iV_{oc} value increases monotonically with the number of ALD cycles of Al_2O_x, achieving an iV_{oc} value of 685 mV (S_{eff} of 33 cm/s) for 12 ALD cycles. Thus, we conclude that the inclusion of an Al_2O_x interlayer between TiO_x and c-Si improves the passivation, increasing the iV_{oc} from 667 to 687 mV, see Figure 5.1 from an effective lifetime point of view (from 400 to 660 µs). Note that annealing is not required to activate the passivation of the Al_2O_x/TiO_x stacks.

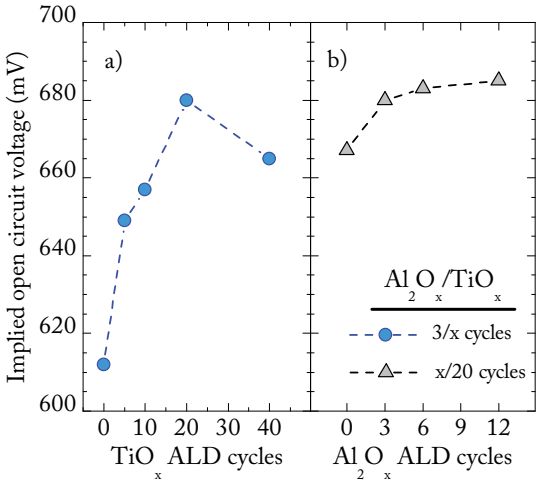

Figure 5.2 Extracted iV_{oc} values vs. (a) the number of TiO_x ALD cycles, with a fixed 3 ALD cycles of Al_2O_x. And (b) Study varying the number of Al_2O_x ALD cycles, with a fixed 20 ALD cycles of TiO_x.

The excellent surface passivation provided by the ALD Al_2O_3 films is due to both chemical and physical passivation mechanisms [17]. In other words, this silicon surface passivation arises from a low density of surface states together with an electric field effect, which is caused by the inherent charge that exists in these films.

In thick annealed Al_2O_3 films this charge is negative, thus, it causes an inversion region on the surface of n-type c-Si wafers. This fact is a counter-productive behaviour for the extraction of electrons. However, it has been reported that relatively thin dielectric Al_2O_3/TiO_2 stacks (~20 nm) exhibit a net positive charge even after an annealing step at 400 ºC [18]. The origin of the surface passivation in ultra-thin conductive Al_2O_x/TiO_x structures and the passivation behaviour with the annealing temperature are not yet clear and further research in this field is required.

Although Al_2O_x/TiO_x stacks provide excellent surface passivation on n-type silicon substrates, good electron conduction properties are mandatory for electron-selective contacts. To verify the contact quality and the influence of the metal capping on its electrical behaviour, test samples were fabricated on n-type c-Si substrates. The same Al_2O_x/TiO_x stacks were deposited on both sides of bare c-Si substrates. Then, one side was completely covered with the capping metal (Mg, Al or Ni) with a thickness of around 15 nm and was finished with an Al layer of 150 nm, while the other side was selectively metalized, with the same electrode stack, defining dot features with different diameters, see the sketch in the inset of Figure 5.4.

Figure 5.3 shows the semi-log *I-V* curves for a reference Al_2O_x/TiO_x stack (6/20 ALD cycles) with the different metal layers. For a direct comparison, the *I-V* measurements were made on dot contacts with the same pad diameter (4 mm) for all the coating metals. The best behaviour corresponds to the sample with Mg/Al metals, achieving a low resistance ohmic curve with currents two orders of magnitude higher than that of the sample in contact with Al alone. In contrast,

the worst result is obtained for the sample in contact with Ni/Al, which results in a non-ohmic curve (see the asymmetry in the current level).

Therefore, the metallic capping plays an important role in the electrical behaviour of the ETL structure. It must be taken into account that, depending on the metal used, the work-function (Φ) changes from a low value to a high value (Φ_{Mg} ~3.6 eV, Φ_{Al} ~4.3 eV and Φ_{Ni} ~5.1 eV). The electrical contact quality improves with the decrease of the metal work-function as expected in metal-semiconductor contacts on c-Si(n) substrates, i.e. the lower the work-function value, the lower the contact barrier height, and higher will be the conduction of the majority carrier conduction through the silicon/contact interface. A similar behaviour has also been reported with a-Si:H passivated contacts using either Mg/Al or Al metal capping [19].

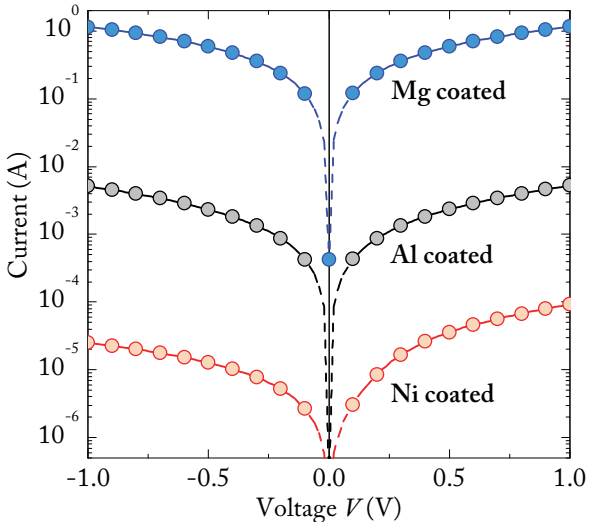

Figure 5.3 Impact of metal capping material on the measured dark current-voltage (I-V) characteristics using Al_2O_x/TiO_x stacks (6/20 ALD cycles) for 4 mm diameter spots.

The impact of the Al_2O_x interlayer thickness ranging from 0 to 24 ALD cycles on the electrical contact quality is shown in Figure 5.4. In all cases, the thickness of the TiO_2 layer was set at 20 ALD cycles and Mg/Al was used as a capping electrode. As it can bee see in this figure, for voltages ranging from -1 to 1 V the characteristics are clearly ohmic for 0, 3 and even 6 ALD cycles. Nevertheless, this electrical behaviour changes to a poor ohmic contact for 12 ALD cycles, and exhibits a pseudo-rectifying *I-V* curve for the case of 24 ALD cycles. This fact is in accordance with the dielectric nature of the alumina films, which must finally block the extraction of electrons, i.e. the tunnel conduction mechanism disappears.

In consequence, the Al_2O_x films prepared with 6 ALD cycles (~0.5 nm) yield the optimum trade-off between good passivation (thick films) and good electrical contact performance (thin films).

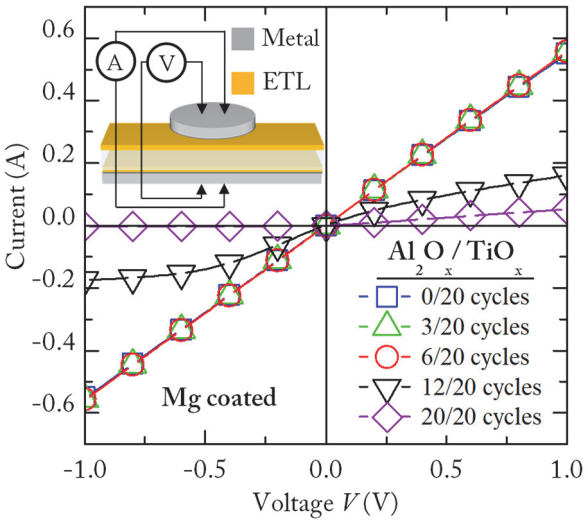

Figure 5.4 Influence of the number of Al_2O_x ALD cycles on I-V curves using Mg-coated samples with a fixed 20 ALD cycles of TiO_x. For a direct comparation, the measurements were performed on 2 mm dot diameter. The test structure is depicted in the inset.

Figure 5.5 shows the *I-V* curves for different dot-like contact diameters with the best stack configuration, i.e. Al_2O_x (6 cycles)/TiO_x (20 cycles)/Mg/Al. The specific contact resistance (r_c) of the stack was extracted by fitting the measured total resistance (R_T) for different dot diameters. The fitting, see Chapter 3 for more details, was done using Eq. (5.1), where ρ and W parameters are the resistivity and thickness of the substrate, respectively. The parameters d and d_b are the diameter of the front dot contact and the estimated back-contact dot diameter, respectively. Finally, the parameter R_0 represents the residual resistance due to test measurements.

$$R_T = \frac{\rho}{d\pi}\tan^{-1}\left(\frac{4}{d/W}\right) + \frac{4r_c}{\pi d^2} + \frac{4r_c}{\pi d_b^2} + R_0 \tag{5.1}$$

The fitting shows that excellent r_c values of 2.5 ±0.5 mΩcm^2 were obtained for our electron-selective contacts, see Figure 5.5. This result improves r_c by more than one order of magnitude compared to SiO_2/TiO_x stacks on n-type substrates [5].

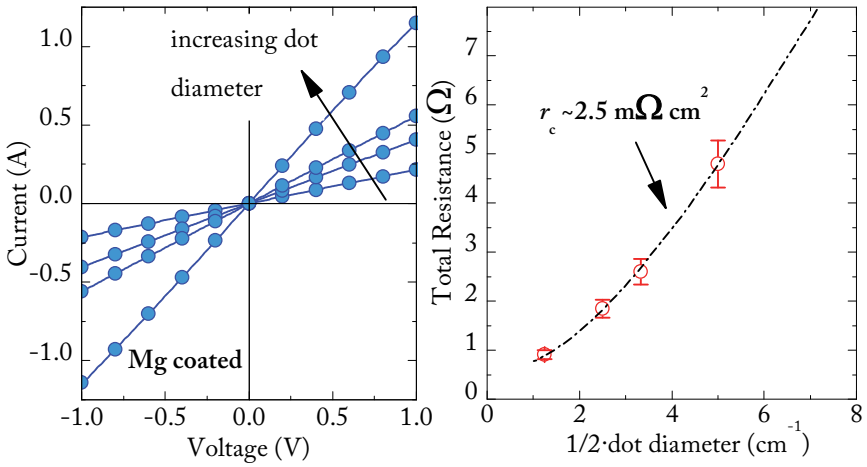

Figure 5.5 I-V measurements of Mg-coated Al_2O_x/TiO_x stack (6/20 ALD cycles) as a function of contact dot diameter (left). And its fitting (dashed line) using Eq. (5.3), (right).

It is important to keep in mind that small r_c values are crucial for the manufacture of high efficiency solar cells with non-fully contact, in which the ETL coverage area fraction (f_{ETL}), defined as the relationship between ETL and the total cell area, is typically in the 1–10% range. Furthermore, taking into account that the specific series resistance (r_s) is limited only by the ETL contact quality, the total series resistance could be roughly calculated as $r_s \approx r_c \cdot 100/f_{ETL}$ (%), resulting in the worst case (f_{ETL} = 1%) values below 0.3 Ωcm^2 in final devices.

In addition, it is also important to note that the surface passivation and the contact resistance are stable up to a temperature of 200 ºC, as shown in Figure 5.6, where the results of cumulative 5 min annealing are presented. The results show that the stability is sufficient to perform the following technological steps and a hypothetical encapsulation-lamination at 150 ºC.

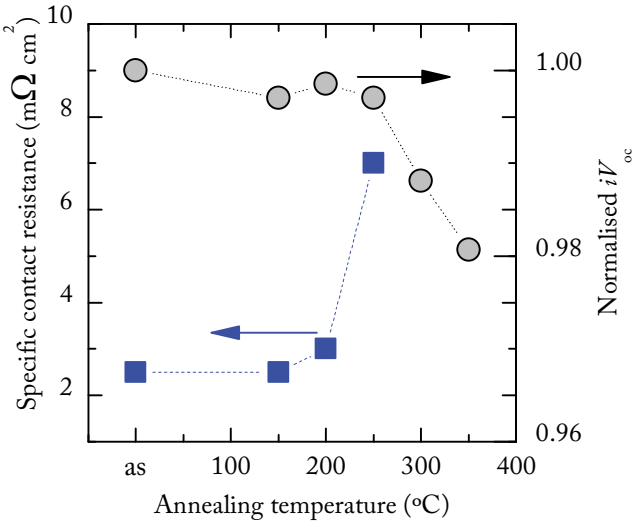

Figure 5.6 Annealing temperature study of Al_2O_x/TiO_x stack (6/20 ALD cycles) for both passivated and contacted (Mg-coated) test samples on n-type c-Si substrates. Notice that only one sample underwent the annealing study, i.e. cumulative annealing. Implied open circuit voltage values are normalized to their initial values (iV_{oc}^n).

Finally, a single figure of merit quantifying the contact quality is the so-called contact selectivity (S_{10}), defined as $S_{10}=\log(V_{th}/(r_c \cdot J_0))$ [20], where V_{th} is the thermal voltage and J_0 is the contact recombination current density. Good selective contacts are characterised by low values of r_c and J_0 simultaneously. Therefore, the higher the S_{10} value, the better the contact behaviour.

Table 5.1 compares the main figures of merit reported in the literature for different ETLs. As can be observe, although the use of a thin a-Si:H(i) or alternatively a thermal SiO_2 film as a passivating interlayer provides excellent surface passivation, these approaches usually exhibit high contact resistance values. The ETL stack reported in this Thesis reaches a remarkable S_{10} value of 13.9, which is the best result without using any PECVD or thermally grown passivation interlayer.

Table 5.1 Summary of ETL strategies applied on n-type c-Si substrates and their relevant contact quality parameters. In the lower part of the table are the TiO_x-based approaches.

Ref.	ETL approach	iV_{oc} (mV)	J_0 (fA/cm²)	S_{eff} (cm/s)	r_c (mΩcm²)	S_{10}
[4]	a-Si:H(i)(6 nm)/LiF_x(1 nm)/Al	732[a]	3[a]	-	7	15.1
[1]	MgO_x(1 nm)/Al	-	-	-	17.5	-
[21]	CS_2CO_3/Al	-	-	-	61.8	-
[21]	MgF_x(1 nm)/Al	534	1500	-	35	8.7
[21]	a-Si:H(i)(6 nm)/MgF_x(1 nm)/Al	710	10	-	76	13.5
[5]	TiO_x(2.5 nm)/Al	-	132[b]	56	20	10.0
[5]	SiO_2(1.2 nm)/TiO_x(2.5 nm)/Al	-	38[b]	16	20	13.5
[8]	TiO_x (3 nm)/Al/Ag	-	3518[b]	300	-	-
T.W.	Al_2O_x(0.5 nm)/TiO_x(1.5 nm)/Mg	683[c]	140[b]	40	2.5	13.9

[a] Reported value related to contact passivation have been measured before LiF_x deposition. [b] Extrapolated using the relationship $J_0=S_{eff} \cdot qn_i^2/N_{Bulk}$ from current S_{eff} values, where N_{Bulk}, q and n_i are the substrate doping, elementary charge and intrinsic concentration, respectively. [c] Measured in asymmetric test samples (one side ideally passivated). *T.W.* means this work.

In order to investigate the surface chemical composition of the reference Al_2O_x/TiO_2 stack (6/20 ALD cycles), uncoated and Mg-coated samples were analysed by the X-ray photoelectron spectroscopy (XPS) technique. Figure 5.7 compares the results of the XPS analysis of Si 2p, Ti 2p and O 1s core levels for both samples.

On the one hand, in both cases, two peaks appear in the Si 2p spectrum. These peaks, which correspond to Si and silicon oxide (Si-O) states, can be deconvoluted and fitted using Gaussian-Lorentzian curves centred at ~99.0 and ~102.0 eV binding energies, respectively. Since an HF dip was performed just before the ALD stack growth, oxidation of the Si surface might occur during the firsts water pulses in the Al_2O_3 deposition stage, where the Si dangling bonds react with oxygen.

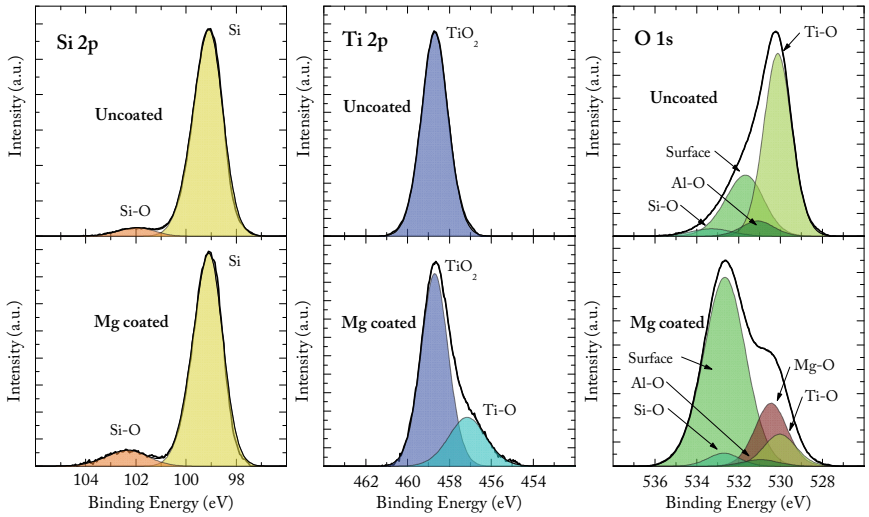

Figure 5.7 High-resolution XPS spectra of both uncoated and Mg-coated Al_2O_x/TiO_x stacks (6/20 ALD cycles) on n-type c-Si substrates. Si 2p (left), Ti 2p (middle) and O 1s (right) core levels spectra showing the multi-peak deconvolution of the fitted curves for different cation oxidation states.

Additionally, Figure 5.8 shows the Al 2p core level spectrum where the Al $2p_{3/2}$ peak centred at a binding energy of ~74.2 eV confirms the existence of the alumina.

On the other hand, the Ti $2p_{3/2}$ core level spectrum for the uncoated sample shows that a single peak centred at a binding energy of ~458.7 eV is enough to fit the curve, for the uncoated sample. However, an extra peak centred at ~457.1 eV appears for the Mg-coated sample. The peak at highest binding energy corresponds to a fully oxidised TiO_2, while the lowest binding energy peak is assigned to a TiO_x layer rich in titanium [10]. From the relative area of the Ti-O peak with respect to the Ti 2p spectrum, an approximate TiO_x content of 26% was calculated, indicating that only a fraction of the TiO_2 layer is under-stoichiometric.

The TMO work function changes strongly with the film stoichiometry [22], i.e. oxygen-deficient layers exhibit lower work-function values and a semi-metallic behaviour. In our devices, these effects could improve the electron selectivity because of a suitable energy band alignment (for n-type c-Si substrates) and an improvement in the conductivity of the layer.

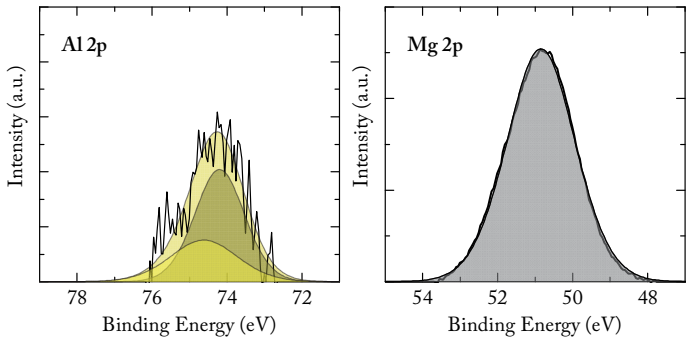

Figure 5.8 High-resolution XPS spectra of Mg-coated Al_2O_x/TiO_x stack (6/20 ALD cycles) on n-type c-Si substrates. The Mg 2p (left) and Al 2p (right) core levels spectra.

In addition, this oxygen deficiency could be attributed to a reaction of the thermally evaporated Mg with the TiO_2 film, forming a magnesium oxide layer (MgO_x). This hypothesis is corroborated by the Mg 2p spectrum, which exhibits a peak centred at a binding energy of ~50.8 eV corresponding to an Mg-O compound, see Figure 5.8.

Finally, an analysis of the O 1s core level spectrum (Figure 5.7) corroborates the presence of the many chemical species mentioned above. First, the Al-O and Ti-O species (with a characteristic binding energy of ~531.5 eV and ~530.0 eV, respectively) are identified in both samples, which correspond to the TiO_x and Al_2O_x layers. However, the sample coated with Mg shows a lower Ti-O intensity, attenuated by the presence of Mg on the upper part, as well as a Mg-O peak at ~530.4 eV, confirming the presence of MgO_x at the TiO_x/Mg interface. An interesting feature is the detection of carbon contaminants adsorbed to the surface after exposure to air, the contribution of which is particularly high for the Mg-coated sample (~532.8 eV) and can be attributed to metal carbonate species, i.e. $MgCO_3$ [23]. In addition, the Si-O component (~533.0 eV) is discernible for both samples.

To better understand the influence of Mg on both the chemistry of Al_2O_x/TiO_x stacks and the electrical contact performance, we analysed their chemical composition using both energy dispersive X-ray spectroscopy (EDX) and electron energy loss spectroscopy (EELS). In Figure 5.9 the high-angle annular dark field (HAADF) scanning transmission electron microscope (STEM) image reveals details of the contact structure. Firstly, a ~15 nm thick Mg layer is observed as well as a ~2 nm thick Al_2O_x/TiO_x stack. With a closer view, an Al_2O_x interlayer (~0.5 nm) is observed at the TiO_x/c-Si interface covered with a ~1.5 nm thick TiO_x layer.

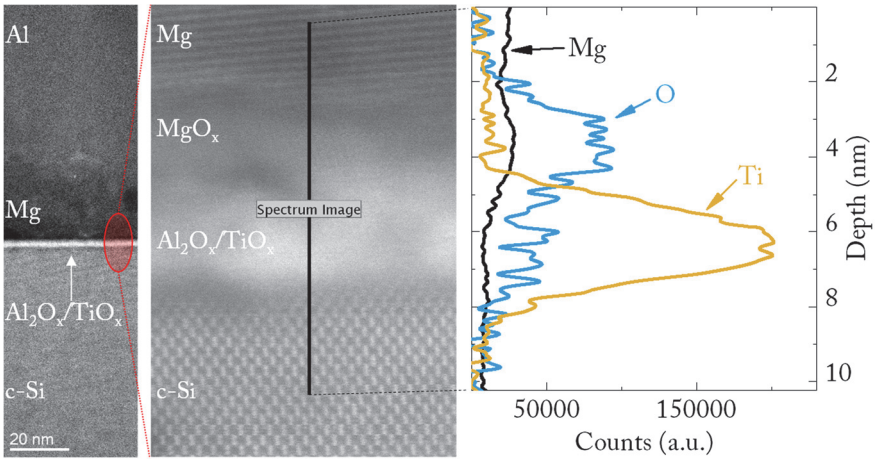

Figure 5.9 High-resolution STEM image of Mg-coated Al_2O_x/TiO_x stack, 6/20 ALD cycles (left). EELS line scan confirming an MgO_x interlayer grown in between TiO_x and Mg films (right).

Due to the strong electron affinity of the Mg metal, the magnesium atoms easily attract the oxygen atoms of the TiO_2 interlayer forming an MgO_x film with a thickness of ~2 nm. The existence of this additional layer is in accordance with the previous XPS measurements and is confirmed by the chemical composition obtained by EELS, see Figure 5.9.

A similar behaviour was also observed when the aluminium was evaporated directly on the TiO_2 layers forming an AlO_x layer (see Figure 5.10), in agreement with other reported studies [5]. However, if Mg is used as a capping metal electrode, the spontaneous growth of a MgO_x film can increase the electron-selectivity of the contacts due to the already reported ETL nature of magnesium oxide [1].

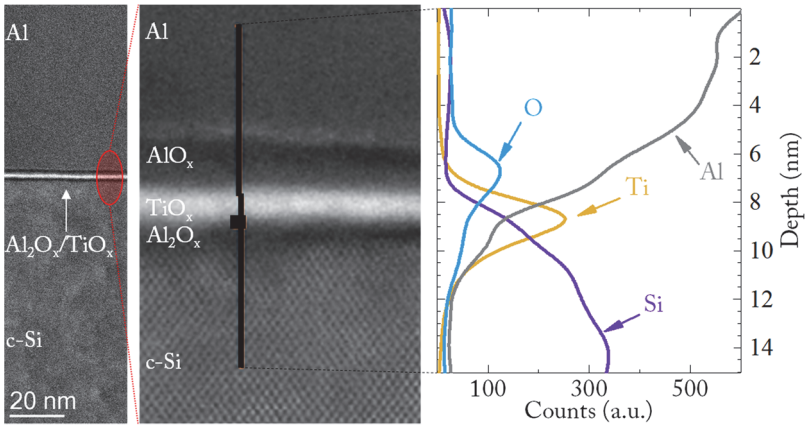

Figure 5.10 High-resolution STEM image of Al-coated Al_2O_x/TiO_x stack, 6/20 ALD cycles (left). EDX line scan confirming an AlO_x interlayer grown in between TiO_x and Al films (right).

5.3 IBC solar cells based on TiO_x and V_2O_x films

To demonstrate the feasibility of Al_2O_x/TiO_x/Mg stack as electron-selective contacts for c-Si solar cells, we fabricated a 3x3 cm^2 IBC structure on n-type c-Si substrates as a proof-of-concept (see Figure 5.11). We apply the foregoing ETL structure together with the previously explored Ni-coated V_2O_x stack as hole-selective contact. The final device was an IBC solar cell fully based on TMOs. The frontal surface was textured and covered with a 50 nm thick alumina layer plus an hydrogenated amorphous silicon carbide layer (a-SiC_x) of 25 nm. The alumina and a-SiC_x offers excellent properties of passivation and antireflection [24]. It is important to indicate that the gap space between the interdigitated back-contacts is also passivated with the same stack of layers. Therefore, all non-contacted surfaces of the solar cell are covered with the same Al_2O_3/a-SiC_x stack, which acts as a passivation and light confining structure.

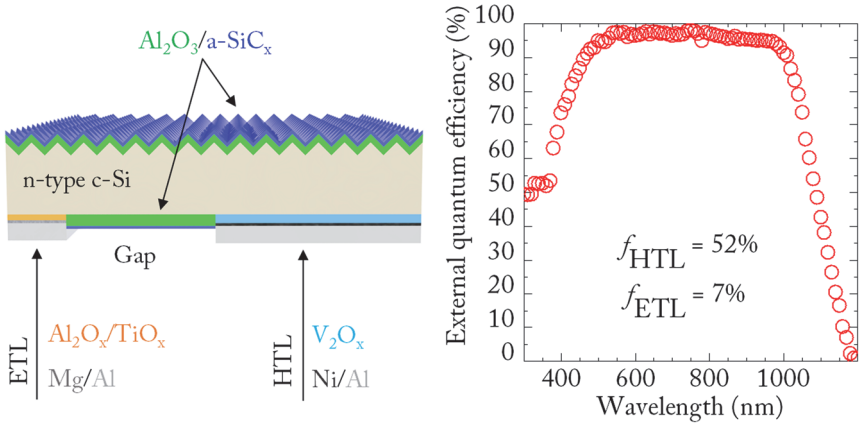

Figure 5.11 A sketch of the fully-TMO based solar cell, showing the main region schemes: the front and gap passivated regions, and the ETL and HTL regions (left). The EQE curve of the best IBC solar cell (f_{HTL}/f_{ETL} = 52%/7% coverage values) (right).

The measurements of external quantum efficiency (*EQE*) for the best device are shown in Figure 5.11. The *EQE* values close to 97% in the visible wavelength range confirm excellent passivation of the front and rear surfaces, which indicates that the electron-selectivity in our ETL regions is good enough to obtain high photovoltaic efficiencies.

In addition, short-circuit current densities (J_{sc}) of approximately 40 mA/cm^2 and power conversion efficiencies (η) in the range of 18 to 19% have been measured independently of the ETL coverage (f_{ETL}), suggesting that the surface passivation in the ETL regions is good enough to avoid excessive electrical shadowing [25]. A similar high-efficiency IBC solar cell has been reported, which combines a LiF_x-based ETL and a V_2O_x-metal-V_2O_x as the HTL [26]. However, in that device a phosphorous diffusion stage at high temperature is needed to form a front surface field (FSF). The details related to the photovoltaic parameters of the fabricated solar cells are listed in Table 5.2. In our devices, open-circuit voltages (V_{oc}) of up to 633 mV and fill factors (*FF*) of around 75% are achieved routinely.

Table 5.2 Summary of the IBC solar cell parameters measured under standard test conditions (AM1.5G 1 kW/m² solar spectrum, 25 °C) for the four device topologies with 9 cm² active area.

f_{HTL}/f_{ETL} (%)	V_{oc} (mV)	J_{sc} (mA/cm²)	*FF* (%)	p*FF* (%)	r_s (Ωcm²)	η (%)
40 / 8	631	39.4	76.4	77.1	0.144	18.9
52 / 7	633	40.0	75.4	76.3	0.183	19.1
64 / 5	633	39.2	76.0	77.9	0.398	18.8
76 / 3	625	39.4	74.1	76.9	0.391	18.2

In Figure 5.12 we compare the illuminated current density-voltage (*J-V*) curve for the best IBC solar cell with the corresponding pseudo-light *J-V* curve obtained from Suns-V_{oc} measurements [27].

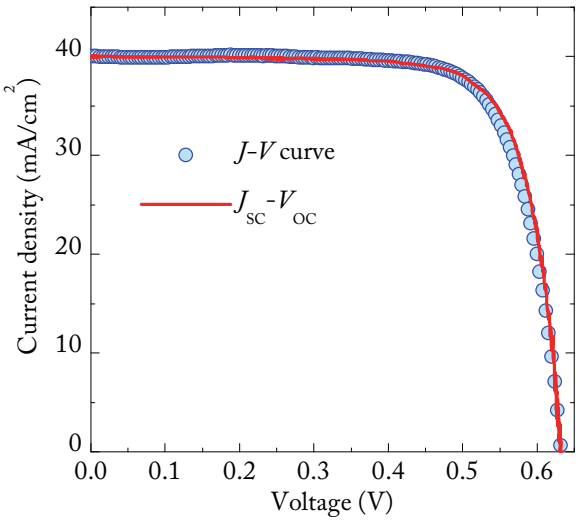

Figure 5.12 Light J-V and pseudo light J-V curves for the best IBC solar cell (f_{HTL}/f_{ETL} = 52%/7% coverage values). The pseudo J-V characteristic, free of series resistance effects, is determined from Suns-V_{oc} Measurements.

The Suns-V_{oc} measurements allow the determination of a pseudo *J-V* curve that excludes the contribution of the series resistance. The coincidence between these two curves suggests that series resistance is not the limiting factor in our solar cell efficiency, as corroborated by similar values of the fill factor and the pseudo-*FF* (p*FF*) parameters.

The specific series resistance calculated using the relationship Eq. (5.2) yields values below 0.4 Ωcm^2 in all cases, confirming the high contact quality of our ETL stack.

$$r_s \cong \left(1 - \frac{FF}{pFF}\right)\frac{V_{oc}}{J_{sc}} \tag{5.2}$$

Therefore, the relatively low *FF* is attributed to a diode ideality factor (*n*) close to two as can be seen in the dark *J-V* curve shown in Figure 5.13. In which, the dark *J-V* curve of the IBC cell fabricated with the laser-doped ETL approach is also shown (see Chapter 4). Both curves exhibit a similar exponential *J-V* trend with an *n* close to 2 at intermediate and high voltage levels. Then, we suggest that the origin of such a relatively high *n* value must be related to the HTL regions.

To optimise the V_2O_x properties, diode test samples were made. In these test samples the c-Si surface were fully covered with the HTL layer, resulting in *n* values of approximately 1.2. This much lower value suggests that the patterning of the V_2O_x needed to create the IBC structure introduces the distortion in the dark *J-V* curve, which negatively effects the values of p*FF* and *FF*. The interdigitated structure of HTL is defined by thermal evaporation of the corresponding V_2O_x/Ni layer on windows previously patterned by standard photolithography process. This technique could lead to poor material coverage at the edge of the HTL interdigitated regions. As a result, there could be an increase of surface recombination at the edges, which explains the exponential trend previously

showed in the *J-V* curve [28] and the difference between the V_{oc} and iV_{oc} values achieved in our completed IBC solar cells and test samples.

It is important to point out that for an interdigitated back-contacted approach, the perimeter *vs.* area related to HTL regions is typically much higher than for the both sides-contacted solar cells. This geometrical factor intensify any effect related to the edge. This drawback could be overcome in the future by using the ALD technique to deposit the ETL and HTL contacts to ensure a conformal layer coverage.

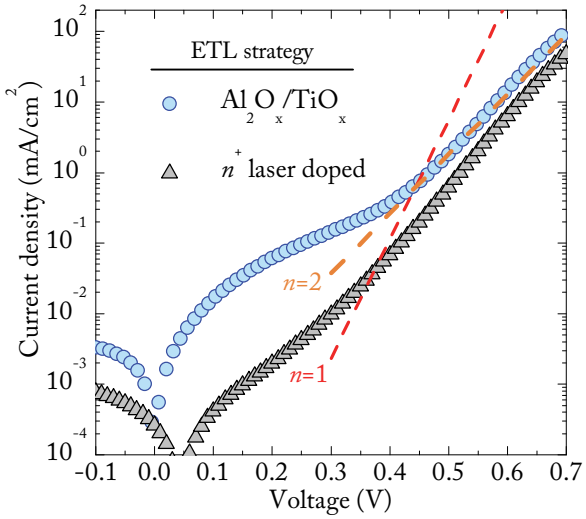

Figure 5.13 Dark J-V characteristic for the best IBC solar cell (f_{HTL}/f_{ETL} = 52%/7% coverage values) and its counterpart (same HTL coverage) using laser-doped contacts to form n^+ ETL regions, showing ideal exponential trends (lines) with ideality factors (n) of 1 and 2.

5.4 References

[1] Y. Wan *et al.*, "Conductive and Stable Magnesium Oxide Electron-Selective Contacts for Efficient Silicon Solar Cells," *Adv. Energy Mater.*, vol. 7, no. 5, p. 1601863, Mar. 2017.

[2] S. Avasthi, W. E. McClain, G. Man, A. Kahn, J. Schwartz, and J. C. Sturm, "Hole-blocking titanium-oxide/silicon heterojunction and its application to photovoltaics," *Appl. Phys. Lett.*, vol. 102, no. 20, p. 203901, May 2013.

[3] R. T. Tung, "The physics and chemistry of the Schottky barrier height," *Appl. Phys. Rev.*, vol. 1, no. 1, p. 011304, Mar. 2014.

[4] J. Bullock *et al.*, "Efficient silicon solar cells with dopant-free asymmetric heterocontacts," *Nat. Energy*, vol. 1, no. 3, p. 15031, Jan. 2016.

[5] X. Yang, Q. Bi, H. Ali, K. Davis, W. V. Schoenfeld, and K. Weber, "High-Performance TiO2-Based Electron-Selective Contacts for Crystalline Silicon Solar Cells," *Adv. Mater.*, vol. 28, no. 28, pp. 5891–5897, Jul. 2016.

[6] L. G. Gerling, C. Voz, R. Alcubilla, and J. Puigdollers, "Origin of passivation in hole-selective transition metal oxides for crystalline silicon heterojunction solar cells," *J. Mater. Res.*, vol. 32, no. 2, pp. 260–268, 2017.

[7] B. Liao, B. Hoex, A. G. Aberle, D. Chi, and C. S. Bhatia, "Excellent c-Si surface passivation by low-temperature atomic layer deposited titanium oxide," *Appl. Phys. Lett.*, vol. 104, no. 25, p. 253903, Jun. 2014.

[8] K. A. Nagamatsu *et al.*, "Titanium dioxide/silicon hole-blocking selective contact to enable double-heterojunction crystalline silicon-based solar cell," *Appl. Phys. Lett.*, vol. 106, no. 12, p. 123906, Mar. 2015.

[9] B. G. Lee, J. Skarp, V. Malinen, S. Li, S. Choi, and H. M. Branz, "Excellent passivation and low reflectivity Al2O3 /TiO2 bilayer coatings for n-wafer silicon solar cells," in *2012 38th IEEE Photovoltaic Specialists Conference*, 2012, pp. 001066–001068.

[10] N. Y. Garces, D. J. Meyer, V. D. Wheeler, Z. Liliental-Weber, D. K. Gaskill, and C. R. Eddy, "Plasma-assisted atomic layer deposition of nanolaminates for gate dielectric applications," *J. Vac. Sci. Technol. B*, vol. 32, no. 3, p. 03D101, May 2013.

[11] D. Suh, D.-Y. Choi, and K. J. Weber, "Al $_2$ O $_3$ /TiO $_2$ stack layers for effective surface passivation of crystalline silicon," *J. Appl. Phys.*, vol. 114, no. 15, p. 154107, Oct. 2013.

[12] R. A. Sinton, A. Cuevas, and M. Stuckings, "Quasi-steady-state photoconductance, a new method for solar cell material and device characterization," in *Conference Record of the Twenty Fifth IEEE Photovoltaic Specialists Conference - 1996*, 1996, pp. 457–460.

[13] B. Hoex, J. Schmidt, P. Pohl, M. C. M. van de Sanden, and W. M. M. Kessels, "Silicon surface passivation by atomic layer deposited Al2O3," *J. Appl. Phys.*, vol. 104, no. 4, p. 044903, Aug. 2008.

[14] X. Yang, P. Zheng, Q. Bi, and K. Weber, "Silicon heterojunction solar cells with electron selective TiOx contact," *Sol. Energy Mater. Sol. Cells*, vol. 150, pp. 32–38, Jun. 2016.

[15] A. Richter, S. W. Glunz, F. Werner, J. Schmidt, and A. Cuevas, "Improved quantitative description of Auger recombination in crystalline silicon," *Phys. Rev. B*, vol. 86, no. 16, p. 165202, Oct. 2012.

[16] A. G. Aberle, "Surface passivation of crystalline silicon solar cells: a review," *Prog. Photovoltaics Res. Appl.*, vol. 8, no. 5, pp. 473–487, Sep. 2000.

[17] B. Hoex, J. J. H. Gielis, M. C. M. van de Sanden, and W. M. M. Kessels, "On the c-Si surface passivation mechanism by the negative-charge-dielectric Al2O3," *J. Appl. Phys.*, vol. 104, no. 11, p. 113703, Dec. 2008.

[18] W.-C. Wang, M.-C. Tsai, J. Yang, C. Hsu, and M.-J. Chen, "Efficiency Enhancement of Nanotextured Black Silicon Solar Cells Using Al $_2$ O $_3$ /TiO $_2$ Dual-Layer Passivation Stack Prepared by Atomic Layer Deposition," *ACS Appl. Mater. Interfaces*, vol. 7, no. 19, pp. 10228–10237, May 2015.

[19] Y. Wan *et al.*, "A magnesium/amorphous silicon passivating contact for n -type crystalline silicon solar cells," *Appl. Phys. Lett.*, vol. 109, no. 11, p. 113901, Sep. 2016.

[20] R. Brendel and R. Peibst, "Contact Selectivity and Efficiency in Crystalline Silicon Photovoltaics," *IEEE J. Photovoltaics*, vol. 6, no. 6, pp. 1413–1420, Nov. 2016.

[21] Y. Wan *et al.*, "Magnesium Fluoride Electron-Selective Contacts for Crystalline

Silicon Solar Cells," *ACS Appl. Mater. Interfaces*, vol. 8, no. 23, pp. 14671–14677, Jun. 2016.

[22] M. T. Greiner and Z.-H. Lu, "Thin-film metal oxides in organic semiconductor devices: their electronic structures, work functions and interfaces," *NPG Asia Mater.*, vol. 5, no. 7, pp. e55–e55, Jul. 2013.

[23] B. V. Crist, *Handbook of monochromatic XPS spectra*. John Wiley, 2000.

[24] G. López *et al.*, "Surface passivation and optical characterization of Al 2 O 3 /a-SiC x stacks on c-Si substrates," *Beilstein J. Nanotechnol*, vol. 4, pp. 726–731, 2013.

[25] C. Reichel, F. Granek, M. Hermle, and S. W. Glunz, "Back-contacted back-junction *n* -type silicon solar cells featuring an insulating thin film for decoupling charge carrier collection and metallization geometry," *Prog. Photovoltaics Res. Appl.*, vol. 21, no. 5, p. n/a-n/a, Mar. 2012.

[26] W. Wu *et al.*, "Dopant-free multilayer back contact silicon solar cells employing V2Ox/metal/V2Ox as an emitter," *RSC Adv.*, vol. 7, no. 38, pp. 23851–23858, Apr. 2017.

[27] R. A. Sinton and A. Cuevas, "A quasi-stead-state open-circuit voltage method for solar cell characterization," in *16th European Photovoltaic Solar Energy Conference*, 2000, no. May, pp. 1–5.

[28] C. H. Henry, R. A. Logan, and F. R. Merritt, "The effect of surface recombination on current in Al $_x$ Ga $_{1-x}$ As heterojunctions," *J. Appl. Phys.*, vol. 49, no. 6, pp. 3530–3542, Jun. 1978.

6 Conclusions and future work

This Chapter summarises the main results and conclusions of this Thesis, as a result of the design, fabrication and characterisation of interdigitated back-contacted c-Si solar cells based on transition metal oxides as selective contacts.

6.1 Conclusions

The interdigitated back-contacted (IBC) structure applied to c-Si solar cells have increased their attention last years, since power conversion efficiencies beyond 26% have been achieved.

In addition, *novel* materials like transition metal oxides (TMOs) are being highly investigated as electron- and hole-selective contacts, using the so-called DASH approach (Dopand Free Asymmetric Heterocontacts), as substitutes to *classical* approximations such as boron or phosphorous diffusions or the use of doped hydrogenated amorphous silicon (a-Si:H) films.

This Thesis deals with the use of TMOs as selective contacts in IBC structures obtaining high efficiency c-Si solar cells. Firstly, exploring the use of vanadium oxide (V_2O_x) as hole transport layer (HTL) and then the titanium oxide (TiO_x) as electron transport layer (ETL), obtaining a final DASH-IBC solar cell with an efficiency of up to 19.1%.

The firs part of the Thesis has demonstrated a *novel* dopant-free V_2O_x/Ni hole-selective contact and its application to an IBC c-Si solar cell architecture. The compositional X-ray photoelectron spectroscopy (XPS) measurements of V_2O_x

layers confirm the oxygen deficiency of this material, which might be the origin of conduction states improving carrier transport through the layer.

The V_2O_x test structures show saturation current densities (J_0) of 175 fA/cm^2 and specific contact resistance (r_c) about 115 mΩcm^2 for 40 nm thick V_2O_x layers. The origin of the good passivation properties, indicated by the relatively low J_0 and high implied open circuit voltage values (iV_{oc} = 675 mV), is probably due to the presence of a very thin SiO_x interlayer confirmed by high resolution transmission electron microscopy (HR-TEM) measurements.

Moreover, the incorporation of a nickel capping layer over the V_2O_x film avoids surface passivation degradation and guarantees/boost the hole-selective contact behaviour.

Finally, cell efficiencies of 19.7% in a 9 cm^2 active area are reached with an open circuit voltage (V_{oc}) of 656 mV, which is a remarkable high value for a c-Si/V_2O_x/Ni heterojunction without additional passivation. Theses results confirm the interest of TMOs as potential HTL materials for crystalline silicon solar cells fabricated with lower thermal budgets and simplified processes.

The second part of the Thesis has demonstrated a *novel* dopant-free ETL based on atomic layer deposition (ALD) of aluminium and titanium oxide (Al_2O_x/TiO_x) bilayer and its application to an IBC c-Si solar cell architecture. The use of a very thin ALD Al_2O_x passivation interlayer (~0.5 nm) between silicon and the ALD TiO_x film (~1.5 nm) improves contact surface passivation, yielding surface recombination velocities below 33 cm/s and iV_{oc} of about 680 mV in test devices.

Additionally, the metal capping layer plays an important role in contact conductivity, being magnesium the best choice, with r_s values as low as 2.5 mΩcm^2. Chemical composition analysis, XPS and electron energy loss spectroscopy

(EELS), confirms spontaneous growth of a magnesium oxide layer, leaving an oxygen-deficient TiO_x layer in the Mg-coated samples, which might be the origin of the improvement in carrier transport through the contact.

Finally, the optimum electron-selective contact configuration consisting of an Al_2O_x (6 ALD cycles)/TiO_x (20 ALD cycles)/Mg stack was applied to an IBC solar cell structure using a V_2O_x/Ni stack as a hole transport layer. In this way, fully TMO-based (9 cm^2 active area) solar cells have been fabricated through a dopant-free and low temperature fabrication process, reaching efficiencies of up to 19.1%. These results outline the potential of TMOs to improve the trade-off between technological complexity and efficiency in c-Si solar cells.

6.2 Future work

It is worth to mention some additionally research aspects, which could help to improve our current devices in the future.

- The use of ALD system to deposit an TMO layer as HTL (e.g. V_2O_x) to overcome efficiency losses due to a non-conformal deposition, especially on the edges of the strip-like hole-transport layer regions, of the thermally evaporated V_2O_x films.

- Replace the a-SiC_x film in the front surface, which acts as protective layer against the subsequent chemical baths through the manufacturing solar cell process. In this way, the use of a TiO_2 thick layer deposited by ALD could be used to overcame the optical losses due to the light absorption of the a-SiC_x film, as well as be used as passivation/protective layer.

Moreover, to implement the TMOs as selective contacts on c-Si substrates for applications in high-volume and low-cost manufacturing solar cells, it is

mandatory to develop new deposition methods for them. In this way, spatial atmospheric ALD system could be good enough solution, which is scalable at large area devices.

Finally, a study in much more detail of the influence of the metal capping with the selective contact properties could help to optimise the final contact, improving the solar cell efficiency. In this way, there are some hypothesis to elucidate how metal interact with the TMOs, such as the difference between work-function energy and/or the formation of an extra-oxide because of the corrosion of the materials due to the difference between Gibbs energy.

Appendix. List of publications

This Chapter describes the most important research work accomplished during the Thesis. The abstracts of the publications, as a main author, are included for the readability of the Chapter.

A. Journal papers

Author

I. Interdigitated back-contacted crystalline silicon solar cells with low-temperature dopant-free selective contacts.

Abstract- *In the field of crystalline silicon solar cells, great efforts are being devoted to the development of selective contacts in search of a fully low-temperature and dopant-free fabrication process compatible with high photovoltaic conversion efficiencies. For high-efficiency devices, selective contacts have to simultaneously combine high conductivity with excellent passivating properties. With this objective, a thin passivating extra layer of a-Si:H or SiO_2 is usually introduced between the conducting layer and the silicon substrate. In this work, we present an interdigitated back-contacted (IBC) silicon based solar cell that avoids the use of either thermal SiO_2 or a-Si:H interlayers achieving a dopant-free, ITO-free and very low thermal budget fabrication process. In this work, we propose a new electron transport layer using ultrathin Al_2O_3/TiO_2 stacks deposited by atomic layer deposition at 100 ºC covered with a thermally evaporated Mg capping film. A specific contact resistance of 2.5 mΩcm^2 has been measured together with surface recombination velocities below 40 cms^{-1}. This electron-selective contact is combined with a thermally evaporated V_2O_x-based hole selective contact to form the rear scheme of an IBC structure with a 3x3 cm^2 active area as a proof-of-concept resulting in efficiencies beyond 19%. This approach sheds light on potential technological simplification and cost reduction in crystalline silicon solar cells.*

Authors- Masmitjà, G.; Ortega, P.; Puigdollers, J.; Gerling Sarabia, L.; Martin, I.; Voz, C.; Alcubilla, R.

Published in- Journal of Materials Chemistry A, vol. 6, pp. 3977-3985, January 2018. DOI: 10.1039/c7ta11308k

II. V_2O_x-based hole-selective contacts for c-Si interdigitated back-contacted solar cells.

Abstract- *Over the last few years, transition metal oxide layers have been proposed as selective contacts both for electrons and holes and successfully applied to silicon solar cells. However, better published results need the use of both a thin and high quality intrinsic amorphous Si layer and TCO (Transparent Conductive Oxide) films. In this work, we explore the use of vanadium suboxide (V_2O_x) capped with a thin Ni layer as a hole transport layer trying to avoid both the intrinsic amorphous silicon layer and the TCO contact layer. Obtained figures of merit for Ni/V_2O_x/c-Si(n) test samples are saturation current densities of 175 fAcm^{-2} and specific contact resistance below 115 mΩcm^2 on 40 nm thick V_2O_x layers. Finally, the Ni/V_2O_x stack is used with an interdigitated back-contacted c-Si(n) solar cell architecture fully fabricated at low temperatures. An open circuit voltage, a short circuit current and a fill factor of 656 mV, 40.7 mAcm^{-2} and 74.0% are achieved, respectively, leading to a power conversion efficiency of 19.7%. These results confirm the high potential of Ni/V_2O_x stacks as hole-selective contacts on crystalline silicon photovoltaics.*

Authors- **Masmitjà, G.**; Gerling Sarabia, L.; Ortega, P.; Puigdollers, J.; Martin, I.; Voz, C.; Alcubilla, R.

Published in- Journal of Materials Chemistry A, vol.5, pp.9182-9189, April 2017. DOI: 10.1039/c7ta01959a

Co-author

I. Transition metal oxides as hole-selective contacts in silicon heterojunctions solar cells.

Authors- Gerling Sarabia, L.; Mahato, S.; Morales-Vilches, A.; **Masmitjà, G.**; Ortega, P.; Voz, C.; Alcubilla, R.; Puigdollers, J.

Published in- Solar Energy Materials & Solar Cells, vol.145, pp.109-115, August 2015. DOI: 10.1016/j.solmat.2015.08.028

B. Conference papers

Author

I. Cost-effective cleaning solutions based on $H_2O/NH_3/H_2O_2$ mixtures for ALD Al_2O_3 passivated IBC c-Si solar cells.

Abstract- *In this work we study cost-effective cleaning solutions applied to interdigitated back-contacted solar cells (IBC), which are passivated by means of atomic layer deposited Al_2O_3 films. The cleaning baths must guarantee very clean surfaces as well as relatively low etching Al_2O_3 rates to avoid excessive undercutting at the edges of strip-like regions. We compare the standard high-cost cleaning procedure used in the microelectronic industry ($RCA_{1/2}$) with simpler cleaning baths based on $H_2O/NH_3/H_2O_2$ mixtures considering different temperatures. The best option is the $RCA_{1/2}$ sequence yielding surface recombination velocities below 4 cm/s but with a total Al_2O_3 etch around 500 nm after the cleaning stage. Nevertheless very simple and less aggressive cleaning baths performed at only 45 ºC obtain a relatively good surface passivation quality, achieving S_{eff} values of 20 ± 5 cm/s reducing the under etch to only 80 nm.*

Authors- **Masmitjà, G.**; Ortega, P.; Martin, I.; Lopez, G.; Calle, E.; Gerling Sarabia, L.; Voz, C.; Alcubilla, R.

Published in- IEEE 2017 Spanish Conference on Electron Devices (CDE), pp.1-3, Barcelona, Spain, February 2017. DOI: 10.1109/CDE.2017.7905228

II. IBC c-Si(n) Solar Cells Based on Laser Doping Processing for Selective Emitter and Base Contact Formation.

Abstract- *In the last years, there is a clear trend in c-Si solar cell fabrication to place both emitter and base contacts on the back side leading to the so-called Interdigitated Back Contacted (IBC) solar cell structure. This solar cell architecture requires excellent front and rear surface passivation as well as a very low recombination emitter. Moreover, laser doping may be an attractive technique to create both selective emitter and base contacts using appropriate dielectric layers as dopant sources, i.e. Al_2O_3 and a-SiC_x(n) stacks for the p^+ and n^+ regions, respectively. In this study, we report on a simplified fabrication process for IBC n-type c-Si solar cells combining laser doping and a conventional boron emitter passivated by Al_2O_3 films. Results show very low emitter recombination currents in the ~10-50 fA/cm^2 range before laser processing. In addition, selective emitter contacts can be created by laser doping with recombination current densities at each contact point around 4.4 pA/cm^2 in relatively low and shallow doped boron doped profiles (sheet resistance ~400 Ω/sq). Finally, IBC solar cells, 3x3 cm^2 device area, were fabricated combining selective laser-doped emitter and base contacts reaching efficiencies up to 20.8%.*

Authors- **Masmitjà, G.**; Ortega, P.; Martin, I.; Lopez, G.; Voz, C.; Alcubilla, R.

Published in- Energy Procedia, vol.92, pp.956-961, Chambery, France, March 2016. DOI: 10.1016/j.egypro.2016.07.107

Co-author

I. Passivating/hole-selective contacts based on V_2O_5/SiO_x stacks deposited at ambient temperature.

Authors- Gerling Sarabia, L.; **Masmitjà, G.**; Ortega, P.; Voz, C.; Alcubilla, R.; Puigdollers, J.

Published in- Energy procedia, vol.124, pp.584-592, Freiburg, Germany, April 2017. DOI: 10.1016/j.egypro.2017.09.294

II. Silicon solar cells with heterojunction emitters and laser processed base contacts.

Authors- Chen, J.; Martin, I.; Lopez, G.; Harrison, S.; **Masmitjà, G.**; Ortega, P.; Alcubilla, R.

Published in- Energy procedia, vol.124, pp.604-611, Freiburg, Germany, April 2017. DOI: 10.1016/j.egypro.2017.09.084

III. Interdigitated back contacted c-Si(p) solar cells with photovoltaic efficiencies beyond 22%.

Authors- Calle, E.; Ortega, P.; López, G.; Martín, I.; Carrió, D.; **Masmitjà, G.**; Voz, C.; Orpella, A.; Puigdollers, J.; Alcubilla, R.

Published in- IEEE 2017 Spanish Conference on Electron Devices (CDE), pp.1-4, Barcelona, Spain, February 2017. DOI: 10.1109/CDE.2017.7905230

IV. Back Junction n-type Silicon Heterojunction Solar Cells with V_2O_5 Hole-selective Contact.

Authors- Gerling Sarabia, L.; **Masmitjà, G.**; Voz, C.; Ortega, P.; Puigdollers, J.; Alcubilla, R.

Published in- Energy Procedia, vol.92, pp.633-637, Chambery, France, March 2016. DOI: 10.1016/j.egypro.2016.07.029

C. Other conference contributions

Author

I. TiO_2 Based Electron Selective Contacts for Interdigitated Back-Contacted c-Si(n) Solar Cells.

Abstract- *In this work we study the properties of atomic layer deposited (ALD) dielectric/TiO_2 stacks deposited at low temperatures as electron transport layers. The goal is to use optimized dielectric/TiO_2 layers as selective contacts in interdigitated back-contacted (IBC) c-Si(n) solar cells. Preliminary results confirm surface recombination velocities below 40 cm/s with implied open circuit voltage (iV_{oc}) values of 675 mV in symmetrical dielectric/TiO_2 test samples. Specific contact resistance values below 3 mΩcm^2 are also measured on stacks properly covered with the metal capping electrode. These excellent results pave the way to use these stacks as electron selective contacts on IBC solar cells, in combination with V_2O_x hole selective contacts. Experimental and technological details as well as first IBC solar cell results will be presented at the conference.*

Authors- **Masmitjà, G.**; Ortega, P.; Puigdollers, J.; Gerling, G.; Voz, C.; Martin, I.; Alcubilla, R.

Published in- MRS - Materials Research Society Fall Meeting & Exhibit, ES11.07.03: Doping-Free Approaches, Boston, USA, November 2017.

Co-author

I. Home-made and low-cost Suns-V_{oc} measurement system to characterize c-Si solar cells.

Authors- Piñol, J.; Ortega, P.; Martín, I.; Orpella, A.; **Masmitjà, G.**; Calle, E.; López, G.; García, M.; Ros, E.; Voz, C.; Puigdollers, J.; Alcubilla, R.

Published in- 12th Spanish Conference on Electron Devices (CDE), Salamanca, Spain, November 2018.

II. Electron selective contacts based on $Al_2O_3/TiO_2/ZnO$ stacks for crystalline silicon solar cells.

Authors- Zafoschnig, L.A.: Ortega, P.; Martín, I.; **Masmità, G.**; López, G.; Alcubilla, R.

Published in- 35th European PV Solar Energy Conference and Exhibition, 2AV.3.14 Heterojunction Solar Cells, Brussels, Belgium, October 2018.

III. Carrier selective contacts based on dielectric/metal/dielectric structures.

Authors- Puigdollers, J.; Gerling Sarabia, L.; **Masmitjà, G.**; Ros, E.; Perea, R.; Ortega, P.; Voz, C.; Alcubilla, R.

Published in- 9th International Conference on Materials for Advanced Technologies, F-05-ID:171168, Singapore, June 2017.

IV. Carrier selective contacts based on V_2O_5-Ag-V_2O_5 structures.

Authors- Puigdollers, J.; Gerling Sarabia, L.; **Masmitjà, G.**; Martin, I.; Ortega, P.; Voz, C.; Alcubilla, R.; Ros, E.; Perea, R.

Published in- EMRS - European Materials Research Society Spring Meeting & Exhibit., Strasbourg, France, May 2017.

V. Dopant-Free Carrier Selective Contacts: A Paradigm- Shift in Crystalline Silicon Photovoltaic Technology.

Authors- Gerling Sarabia, L.; **Masmitjà, G.**; Ortega, P.; Martin, I.; Voz, C.; Puigdollers, J.; Alcubilla, R.

Published in- 11th Spanish Conference on Electron Devices, Barcelona, Spain, February 2017.

VI. Passivating Electron- and Hole-Selective Materials for Crystalline Silicon: Interface Reactions and Passivation Alternatives.

Authors- Gerling Sarabia, L.; **Masmitjà, G.**; Ortega, P.; Voz, C.; Alcubilla, R.; Puigdollers, J.

Published in- MRS - Materials Research Society: Spring Meeting & Exhibit, Phoenix, USA, May 2016.

UNIVERSITAT POLITÈCNICA DE CATALUNYA
BARCELONATECH
Departament d'Enginyeria Electrònica